EBM Experimental Biology and Medicine

Volume 249 | Issue 1

Experimental Biology and Medicine

Chief Editor

Steven Richard Goodman
University of Tennessee Health Science Center, Memphis, USA

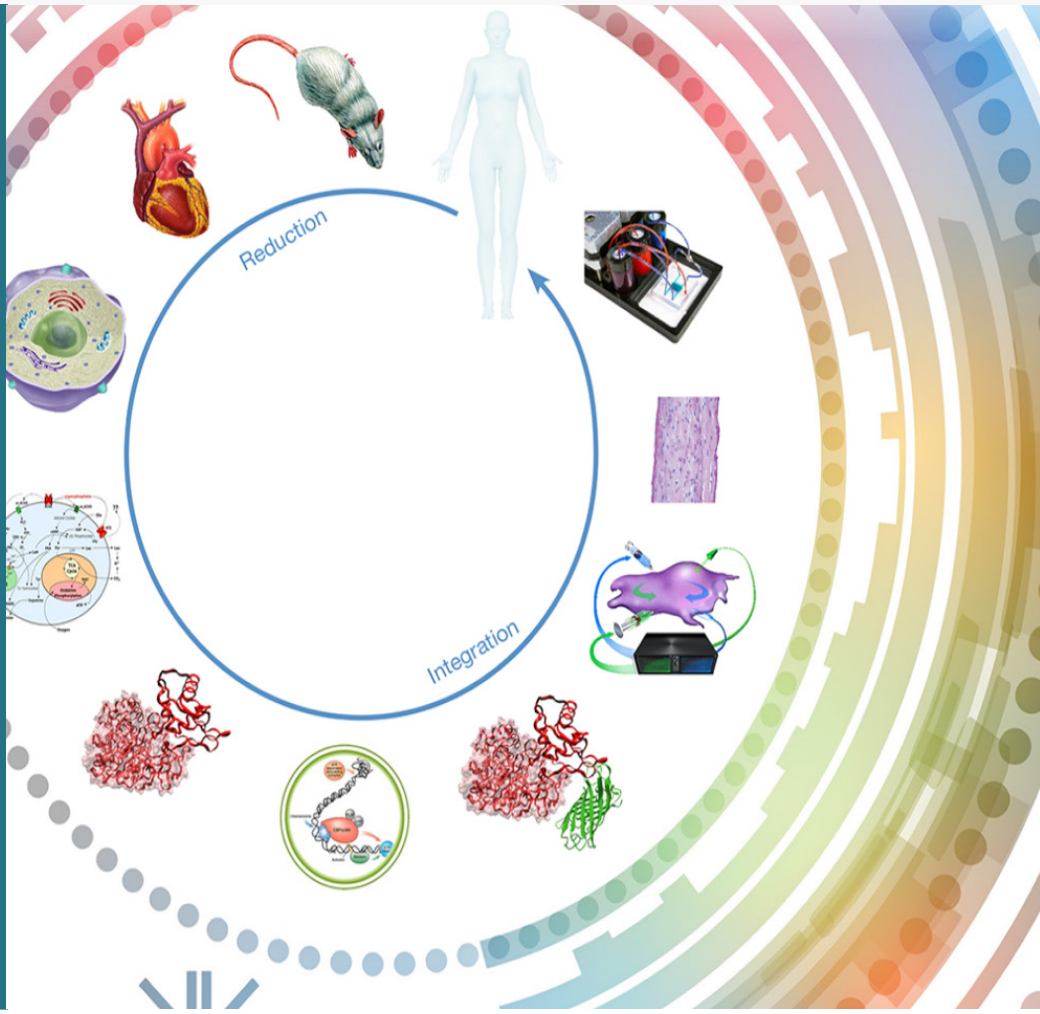

ISBN 978-2-8325-4673-4
DOI 10.3389/978-2-8325-4673-4

frontiers | Publishing Partnerships

SEBM Executive Council

Publication Committee

Society for Experimental Biology and Medicine
3220 N Street NW, #179
Washington DC 20007, USA
Executive Director – ed@sebm.org
Editor-in-Chief – ebm@sebm.org

www.sebm.org

Editorial Board

ISSN 1535-3699
ISBN 978-2-8325-4673-4
DOI 10.3389/978-2-8325-4673-4

EBM Experimental Biology and Medicine

2024 | Volume 249 | Issue 1 | ISSN 1535-3699

Table of contents

Clinical Trials

Immunology/ Microbiology/ Virology

Highlight article

EBM Experimental Biology and Medicine

TYPE Editorial
PUBLISHED 30 January 2024
DOI 10.3389/ebm.2024.10069

OPEN ACCESS

*CORRESPONDENCE
Steven R. Goodman,
sgoodma5@uthsc.edu

RECEIVED 19 December 2023
ACCEPTED 04 January 2024
PUBLISHED 30 January 2024

CITATION
Goodman SR (2024), Editorial: Experimental biology and medicine: new frontiers.
Exp. Biol. Med. 249:10069.
doi: 10.3389/ebm.2024.10069

Editorial: Experimental biology and medicine: new frontiers

Steven R. Goodman*

Department of Pediatrics, College of Medicine, University of Tennessee Health Science Center, Memphis, TN, United States

KEYWORDS

experimental biology, medicine, frontiers, editorial, publishing partnership

Experimental Biology and Medicine (EBM) has transferred to the Gold open access publisher Frontiers with this being the seminal issue of the partnership. Authors can submit manuscripts through the Frontiers portal (https://www.ebm-journal.org/submission/submit).

The Society of Experimental Biology and Medicine (SEBM) was created in 1903 in the Northeast of the United States and its journal, then called the *Proceedings of the Society of Experimental Biology and Medicine*, was first published in June 1904. The *Proceedings of the Society of Experimental Biology and Medicine* was renamed *Experimental Biology and Medicine (EBM)* in 2001. I was honored to be selected as the Editor-in-Chief of EBM in 2006, with my first issue published in July of that year. When being interviewed for the position of Editor-in-Chief, I stated two goals: 1) to expand the number of categories from the seven that existed in 2006 by adding cutting edge interdisciplinary and multidisciplinary new categories and 2) to globalize the journal and, in so doing, globalize the Society. We have accomplished both goals over the last 17 years.

EBM now has twenty-two categories to which authors can submit manuscripts that encompass the breadth of modern biomedical research. Our categories cover the entire translational spectrum including basic, preclinical, clinical, clinical trial and population research. EBM's focus is on biomedical research that is relevant to the practice of medicine. We publish original research articles, Brief Communications, Reviews, Mini Reviews, and at the Editor-in-Chief's discretion Commentaries and Editorials.

In terms of global expansion EBM/SEBM now has offices and Global Editors on the six habitable continents. In addition to its US offices in Memphis, Tennessee, College Station, Texas, and Washington DC; EBM/SEBM now has offices in Taiwan (Tainan), the United Kingdom (London), China (Chengdu), Brazil (Campinas), Ghana (Accra), and Australia (Perth). The current 180 members of the Editorial Board are outstanding scientists coming from the global research community. With the accomplishments of broadening the scope and coverage of our categories and expanding to all habitable continents, EBM submissions have grown by over 6-fold since my becoming Editor-in-Chief, with the correlated growth of the impact of our content.

EBM is unique in its broad range of topical areas and its coverage of the complete translational research spectrum. I believe that building upon its strong history and current direction, EBM will become the premier journal that publishes biomedical research that has a direct impact on the practice of modern medicine. The new EBM-Frontiers partnership is

committed to a fully open access model which makes our publications rapidly accessible to all researchers internationally. Advances in biomedical research require open, transparent, rapid communication between all researchers. It is this international collegial interaction which will have the greatest impact upon improving the health and wellbeing of all people around the globe.

I personally invite you to submit your work to *Experimental Biology and Medicine*. We will oversee your submission in the manner that we want our own work to be reviewed and judged. Together we will help transform global health through biomedical research.

Author contributions

The author confirms being the sole contributor of this work and has approved it for publication.

Conflict of interest

The author declares that the research was conducted in the absence of any commercial or financial relationships that could be construed as a potential conflict of interest.

EBM Experimental Biology and Medicine

TYPE Original Research
PUBLISHED 13 February 2024
DOI 10.3389/ebm.2024.10111

OPEN ACCESS

*CORRESPONDENCE
Yongmei Jiang,
jiangyongmei-1@163.com

†These authors have contributed equally to this work

RECEIVED 02 March 2023
ACCEPTED 02 October 2023
PUBLISHED 13 February 2024

CITATION
Dai Q, Shi R, Zhang G, Wang Y, Ye L, Peng L, Guo S, He J, Yang H and Jiang Y (2024), miR-539-5p targets BMP2 to regulate Treg activation in B-cell acute lymphoblastic leukemia through TGF-β/Smads/MAPK.
Exp. Biol. Med. 249:10111.
doi: 10.3389/ebm.2024.10111

miR-539-5p targets BMP2 to regulate Treg activation in B-cell acute lymphoblastic leukemia through TGF-β/Smads/MAPK

Qingkai Dai[1,2†], Rui Shi[1,2†], Ge Zhang[1,2], Yuefang Wang[1,2], Lei Ye[1,2], Luyun Peng[1,2], Siqi Guo[1,2], Jiajing He[1,2], Hao Yang[1,2] and Yongmei Jiang[1,2*]

[1]Department of Laboratory Medicine, West China Second University Hospital, Sichuan University, Chengdu, Sichuan, China, [2]Key Laboratory of Obstetric and Gynecological and Pediatric Diseases and Birth Defects of Ministry of Education, Chengdu, Sichuan, China

Abstract

MicroRNAs (mRNAs) were believed to play an important role in cancers, and this study aimed to explore the mechanism of miRNA regulating Treg in B-cell acute lymphoblastic leukemia (B-ALL). Firstly, the differentially expressed miRNAs and target genes significantly associated with Tregs were screened out by high-throughput sequencing, and their enrichment pathways were analyzed. The binding relationship between miRNA and target genes was further verified, and the effects of miRNA on the proliferation and apoptosis of B-ALL Nalm-6 cells and Treg activation were analyzed. Results showed that differentially expressed miR-539-5p was significantly under-expressed, and its target gene BMP2 was significantly over-expressed in B-ALL, and significantly enriched in the TGF-β1 pathway. In addition, both miR-539-5p and BMP2 were significantly correlated with Treg activity in B-ALL. *In vitro* experiments further confirmed that miR-539-5p could directly target BMP2. The low expression of miR-539-5p in B-ALL significantly promoted BMP2 expression to promote the proliferation and inhibit apoptosis of Nalm-6 cells. Furthermore, the high expression of BMP2 in B-ALL could cooperate with TGF-β1 to promote the activation of human $CD4^+CD25^-$T cells to Treg, and significantly activate the TGF-β/Smads/MAPK pathway. *In vivo* experiments also confirmed that overexpression of miR-539-5p significantly inhibited BMP2 to suppress Treg activation and Smad1 and Smad2 phosphorylation, and finally inhibit the B-ALL process. In conclusion, miR-539-5p was significantly under-expressed in B-ALL and could target BMP2 to promote its expression, and the overexpressed BMP2 further promoted Treg activation in B-ALL by regulating TGF-β/Smads/MAPK pathway.

KEYWORDS

miR-539-5p, BMP2, TGF-β, Treg, B-cell acute lymphoblastic leukemia

Impact statement

Acute lymphoblastic leukemia (ALL) is a hematological malignancy characterized by abnormal proliferation of primary and juvenile lymphocytes in the bone marrow and peripheral blood. Exploring the pathogenesis of ALL is of great clinical significance for further improving the long-term survival rate and reducing the recurrence of ALL. Studies have shown that miRNA can be used for early clinical diagnosis and prognosis of tumors, and play an important role in ALL. In this study, high-throughput sequencing technology was used to screen the differentially expressed miRNAs of ALL, and the mechanism was explored based on the regulatory Treg. It was found that miR-539-5p was significantly under-expressed in ALL, and could target BMP2 to promote its expression. Overexpression of BMP2 further promoted the activation of Treg in ALL by regulating the TGF-β/Smads/MAPK pathway. The study can provide new ideas and methods for understanding the occurrence and development of ALL.

Introduction

Acute lymphoblastic leukemia (ALL) is one of the most common hematological malignancies in children, accounting for about 20% of pediatric cancers [1]. It is mainly divided into B-cell ALL (B-ALL) and T-cell ALL (T-ALL), among which B-ALL accounts for 85% and T-ALL accounts for 15% [2]. In recent years, the 5-year survival rate of ALL is relatively high, which can reach 90% [3]. However, 20% of ALL are still at risk for relapse, and treatment outcomes after relapse are unsatisfactory and are the leading cause of death in ALL [4]. With the rise of immunotherapy, immunotherapies targeting ALL antigen-associated monoclonal antibodies and chimeric antigen receptor T cells have been shown to be effective against ALL and can significantly improve the prognosis of patients with relapsed/refractory ALL [5]. In addition, miRNAs have been described as modulators of a large number of different immune processes and have the potential to be key to the future development of immunotherapy [6]. Similarly, it is currently believed that the most important factors affecting the recurrence of ALL are the genetic and molecular biological abnormalities in the course of the disease [7]. Some studies have helped to demonstrate that specific miRNA gene expression signatures are associated with specific B- or T-ALL subpopulations. Further exploring the involvement of miRNA genes in the disease process of B-ALL alone or in the network, and clarifying the relationship between specific miRNA and the pathogenesis of B-ALL, will have important clinical significance for reducing the recurrence of B-ALL.

ALL, as cancer affecting lymphoid blood cells, originates primarily from B or T lymphoid progenitor cells [8]. T lymphocytes are an important member of cellular immunity in the body, which can be further divided into $CD4^+$ T and $CD8^+$ T cells [9]. Abnormal expression of $CD4^+$ and $CD8^+$ T cells has been confirmed in previous studies of patients with solid tumors [10, 11]. Regulatory T cells (Treg) are the immunosuppressive T cell subsets of $CD4^+$ T cells, which can inhibit the activation and proliferation of effector T cells and the functions of primary and memory T lymphocytes, and participate in the maintenance of autoimmune homeostasis [12, 13]. Studies have found that Treg can suppress the anti-cancer immune response through a variety of immune regulatory pathways, leading to cancer evasion from immune surveillance [14]. The abnormal number and function of Treg are involved in a variety of solid cancers and hematological malignancies, and are correlated with the prognosis of cancers, which has important clinical value for the evaluation and prognosis of patients [15]. Moreover, studies have shown that Treg cells in B-ALL patients have an important relationship with immune deficiency [16], and the differential expression levels and regulation of Treg may affect the diagnosis and treatment of B-ALL. However, the specific mechanism of regulating Treg in B-ALL remains unclear and needs further study.

Therefore, in this study, high-throughput sequencing was used to analyze the whole transcriptome in peripheral blood mononuclear cells (PBMCs) of B-ALL, and the differentially expressed miR-539-5p and its target gene bone morphogenetic protein 2 (BMP2) were screened to be involved in Treg regulation in B-ALL. *In vitro* and *in vivo* experiments further confirmed the regulatory effects and the possible mechanism of the miR-539-5p/BMP2 regulatory network on Treg in B-ALL.

Materials and methods

Clinical sample collection

The high-throughput sequencing samples were collected from five newly diagnosed B-ALL children at West China Second University Hospital of Sichuan University, and five healthy children who underwent physical examination in the outpatient department of our hospital were selected as the control. The blood routine and various indexes of children in control group showed normal, with no previous history of hematological malignancy or family history. And there was no statistical difference in age or gender between the two groups. In addition, 46 B-ALL children and 42 healthy children matched by age and sex were included for follow-up study. The diagnostic criteria for B-ALL refer to Chinese Children Cancer Group (CCCG) ALL 2015 protocol (CCCG-ALL-2015). This study was approved by the Ethics Committee of West China Second University Hospital of Sichuan University, and all patients and their families agreed and signed informed consent.

Isolation of PBMCs

Freshly 2 mL EDTA anticoagulated whole blood from B-ALL patients and healthy children were mixed with 2 mL PBS, and then slowly added to 3 mL of Ficoll-Paque density gradient media (cat. no. 17-5442-02; GE, United States). Centrifugation at room temperature at 400 g for 30 min, the top layer of plasma was removed, and the middle layer was washed with 3-fold volume of PBS. After centrifugation at 400 *g* for 10 min, the supernatant was discarded and the precipitation was PBMCs for subsequent study.

Transcriptome sequencing analysis

Total RNA was extracted from PBMCs [17–19] by Trizol (cat. no. 15596026; Invitrogen, United States), and the integrity and concentration of RNA were examined using Agilent 2100 Bioanalyzer (Agilent, United States). The TruSeg Small RNA Sample Prep kit (cat. no. RS-200-0012; Illumina, United States) was used to obtain cDNA. The cDNA library was further constructed and enriched, and sequencing was performed on the Illumina platform. The original sequencing data were de-spliced and the quality-filtered sequences were de-processed. According to the human genome annotation, the abundance of the de-duplicated sequences was annotated. The characteristics and expression levels of miRNAs in PBMCs of B-ALL and controls were statistically analyzed. And DESeq software of R language (version 4.3.0) was used to analyze the differentially expressed miRNA and mRNA, while $p < 0.05$ and $|\log2FoldChange| > 1.0$ were defined as significantly differentially expressed mRNA or miRNA. Further, R language was used to cluster the differentially expressed miRNAs, predict the target genes, and perform functional enrichment analysis of the predicted target genes, including gene ontology (GO) and Kyoto Encyclopedia of Genes and Genomes (KEGG) analysis.

Cell culture and transfection

Human B lymphoid leukemia cells Nalm-6 and human embryonic kidney cells H293-T were both purchased from Procell (Wuhan, China). H293-T cells were cultured in DMEM (Hyclone, United States) containing 10% FBS (CLARK BIOSCIENCE, United States) and 1% P/S (Hyclone, United States) and were used for double luciferase reporter assay. Nalm-6 cells were cultured in RPMI-1640 medium (Hyclone, United States) to analyze the role of miR-539-5p/BMP2 in the induction of Treg by Nalm-6 cells. Negative control-siRNA (NC-siRNA), siRNA targeting BMP2 (BMP2-siRNA), NC of pcDNA plasmid (pcDNA-NC), pc-DNA plasmid containing BMP2 sequence (pcDNA-BMP2), NC-mimic and miR-539-5p-mimic (all synthesized or purchased from Guangzhou Ribobio, China) were transfected into Nalm-6 cell by Lipofectamine 2000 (Beyotime, China).

Double luciferase reporter assay

The binding sites of miR-539-5p and BMP2 were predicted by online software Targetscan[1], and the BMP2 wild-type (BMP2-WT) and mutant sequence (BMP2-Mut) were constructed and cloned into the dual luciferase reporter pmirGLO-UTR vector. H293-T cells were co-transfected with the reporter plasmid and NC-mimic or miR-539-5p-mimic for 48 h by Lipofectamine 2000. Firefly luciferase and renilla luciferase values were determined and luciferase activity was calculated using the dual luciferase reporter kit (Promega Corporation, United States).

Cell activity analysis

The proliferation activity of Nalm-6 cells was analyzed by Cell Counting Kit-8 (CCK8). After different treatments, Nalm-6 cells were incubated with 10 μL CCK8 detection reagent (cat. no. C0037; Beyotime, China) for 1 h. The absorbance was measured at 450 nm and the cell viability was calculated.

Apoptosis detection

Apoptosis was detected by Annexin V-FITC/PI double staining. Nalm-6 cells with different transfection were collected, resuspended with 500 μL Binding Buffer, stained with 5 μL Annexin V-FITC, and 5 μL PI (cat. no. C1062S; Beyotime, China) for 15 min at room temperature under darkness, and then analyzed by flow cytometer (BD FACSCanto, United States).

Sorting of $CD4^+CD25^-$T cells in PBMCs

The human CD4 T lymphocyte enrichment kit (cat. no. 557939; BD, United States) was used to enrich $CD4^+$T cells in PBMCs of normal healthy subjects according to the manufacture instructions. Then, the number of enriched $CD4^+$T lymphocytes was counted and washed by 1×BD IMag buffer (cat. no. 552362; BD, United States), and the BD IMag anti-human CD25 magnetic particle-DM (cat. no. 558005; BD, United States) was added to incubate for 30 min at room temperature. After bringing the BD IMag-particle labeling

1 www.targetscan.org

volumes up to 1–8 × 10^7 cells/mL with 1 × BD IMag buffer, the tubes were immediately placed on a cell separation magnet (cat. no. 552311; BD, United States) to incubate at room temperature for 9 min. Finally, carefully aspirate the supernatant, which contains the negative fraction ($CD4^+CD25^-$T cells).

Treg induction *in vitro*

Primary peripheral blood $CD4^+CD25^-$T cells were cultured in the RPMI-1640 medium containing anti-CD3 (5 μg/mL), anti-CD28 (5 μg/mL), IL-2 (100 U/mL) and retinoic acid (10 nM) at 37°C and 5% CO_2 for 5 days for routine Treg induction. To analyze the role of miR-539-5p in Nalm-6 cell-induced Treg activation, subsequent experiments were divided into eight groups: control group, Nalm-6 cell supernatant group (NC), miR-539-5p-mimic transfected cell supernatant group (miR-539-5p-mimic), BMP2-siRNA transfected cell supernatant group (BMP2-siRNA), TGF-β1 positive control group (TGF-β1), TGF-β1+NC, TGF-β1+miR-539-5p-mimic, TGF-β1+BMP2-siRNA. The control group was treated by the routine induction method. Groups containing TGF-β1 were supplemented with 10 ng/mL TGF-β1. The NC, miR-539-5p-mimic and BMP2-siRNA groups were added with the culture supernatant of Nalm-6 cells transfected with NC, miR-539-5p-mimic and BMP2-siRNA at 1:1, respectively.

Treg cell ratio analysis

The proportion of Treg in peripheral blood of B-ALL patients was characterized by $CD3^+CD4^+CD25^+CD127^-$ in this study. Briefly, 5 μL fluorescein-labeled monoclonal antibodies FITC-CD3 (cat. no. 11-0037-42; Invitrogen, United States), PerCP-Cy5.5-CD4 (cat. no. 45-0049-42; Invitrogen), PE-CD25 (cat. no. 12-0259-80; Invitrogen) and APC-CD127 (cat. no. 17-1278-42; Invitrogen) were added to 100 μL anticoagulant blood samples, and incubated at room temperature for 30 min away from light. Then, 2,000 μL of FACS Lysing Solution (BD, United States) was added and incubated at room temperature and away from light for 10 min. After washing and suspension with PBS, flow cytometer was used for detection. In addition, the proportion of $Foxp3^+$ Treg in $CD4^+CD25^-$T cells after induction was also measured. The cells with different treatments were incubated with 5 μL FITC-labeled CD4 antibody (cat. no. 11-0041-82; Invitrogen) and APC-CD25 antibody (cat. no. MA5-16224; Invitrogen) at 4°C for 30 min. After washing with PBS, the membrane-breaking fixative was incubated at 4°C for 1 h. Then, 5 μL PE-Foxp3 antibody (cat. no. 12-4774-42; Invitrogen) was incubated at 4°C for 1 h. The proportion of $Foxp3^+$Treg cells was detected by flow cytometer.

Proliferation activity of $CD4^+CD25^-$T cells

The isolated $CD4^+CD25^-$T cells were induced at 37°C and 5% CO_2 for 5 days according to different groups. After centrifugation, the cells were incubated at 37°C for 20 min with 2 μM carboxyfluorescein succinimidyl ester (CFSE) staining solution (cat. no. C0051; Beyotime, China), neutralized and washed twice with RPMI-1640 containing FBS. CFSE was detected by flow cytometry, and the proliferation rate was calculated.

Animals experimental design

Eighteen NOD/SCID mice, weighing 18–20 g and aged 4–5 weeks, were purchased from Chengdu Dossy experimental animals Co., LTD. [animal license number: SYXK (chuan) 2019-189]. Animal experiments were approved by the Ethics Committee of West China Hospital of Sichuan University. The mice were randomly divided into three groups: control group, NC-mimic group and miR-539-5p-mimic group. Nalm-6 cells in the logarithmic growth phase were selected, and NOD/SCID mice were injected with 5 × 10^6 Nalm-6 cells, NC-mimic or miR-539-5p-mimic transfected Nalm-6 cells via tail vein, respectively.

Wright-Giemsa staining

After the bone marrow of mice was taken for smear, 2–3 drops of Wraith-Giemsa dye solution (cat. no. CR2012035; Servicebio, China) was added to dye for 2 min, then the same amount of 0.01 M phosphate buffer (pH6.4–6.8) was stained for 5 min. The morphological changes were observed by a digital slice scanner (Pannoramic 250, 3DHISTECH, Hungary).

ELISA detection

The expressions of BMP2, IL-10, IL-35, TGF-β1 and TGF-β2 in human/mouse serum and cells were detected by the corresponding ELISA kit (Beyotime, China), each sample was repeated at least three times.

Real-time quantitative polymerase chain reaction (RT-PCR)

Firstly, total RNA was extracted by Trizol reagent. For miRNA detection, the total RNA was reversed into cDNA by Bulge-LoopTM miRNA qRT-PCR Primer (cat. no. R10031.7; Ribobio, China), and Bulge-Loop miRNA qRT-PCR Starter Kit

TABLE 1 The primer sequences used in the study.

	Gene	Primer
miRNA	hsa-miR-548ba	Bulge-Loop hsa-miR-548ba Primer Set (cat. no. MQPS0001824-1-200; Ribobio, China)
	hsa-miR-1266-5p	Bulge-Loop hsa-miR-1266-5p Primer Set (cat. no. MQPS0000526-1-200; Ribobio, China)
	hsa-miR-466	Bulge-Loop hsa-miR-466 Primer Set (cat. no. MQPS0001494-1-200; Ribobio, China)
	hsa-miR-551a	Bulge-Loop hsa-miR-551a Primer Set (cat. no. MQPS0001855-1-200; Ribobio, China)
	hsa-miR-4484	Bulge-Loop hsa-miR-4484 Primer Set (cat. no. MQPS0001400-1-200; Ribobio, China)
	hsa-miR-1-3p	Bulge-Loop hsa-miR-1-3p Primer Set (cat. no. MQPS0000625-1-200; Ribobio, China)
	hsa-miR-133a-3p	Bulge-Loop hsa-miR-133a-3p Primer Set (cat. no. MQPS0000607-1-200; Ribobio, China)
	hsa-miR-1250-5p	Bulge-Loop hsa-miR-1250-5p Primer Set (cat. no. MQPS0000499-1-200; Ribobio, China)
	hsa-miR-539-5p	Bulge-Loop hsa-miR-539-5p Primer Set (cat. no. MQPS0001793-1-200; Ribobio, China)
	hsa-miR-11401	*Homo sapiens* miR-11401 stem-loop (cat. no. HmiRQP4695; FulenGen, China)
	hsa-miR-6718-5p	*Homo sapiens* miR-6718-5p stem-loop (cat. no. HmiRQP2994; FulenGen, China)
mRNA	TGF-β	F: 5′-GCCGACTACTACGCCAAGGAGGTCA-3′
		R: 5′-CGGTTGCTGAGGTATCGCCAGGAATT-3′
	BMP2	F: 5′-GACGTTGGTCAACTCTGTTAAC-3′
		R:5′-GTCAAGGTACAGCATCGAGATA-3′
	IL-10	F: 5′-GTTGTTAAAGGAGTCCTTGCTG-3′
		R: 5′-TTCACAGGGAAGAAATCGATGA-3′
	IL-35	F: 5′-CCTTGCACTTCTGAAGAGATTG-3′
		R: 5′-GGTCTCTCTGGAATTTAGGCAA-3′
	Foxp3	F: 5′- AGGCTCCAGAGAAGCAGCGGACACT-3′
		R: 5′-TCAGGTTGTGGCGGCTGGCGTTCTT-3′
	β-actin	F: 5′-GAAGATCAAGATCATTGCTCC-3′
		R: 5′-TACTCCTGCTTGCTGATCCA-3′

(cat. no. R11067.2; Ribobio) was used for PCR reaction with 20 μL reaction system. For mRNA detection, the cDNA was obtained by Prime Script RT reagent Kit (cat. no. RR047A; Takara, Japan). Then TB Green Premix Ex Taq II (cat. no. RR820A; Takara) was used for PCR reaction. The relative expression levels were calculated using $2^{-\triangle\triangle CT}$ methods. U6 was used as the internal reference for miRNA expression [20], and β-actin was used for mRNA. The primer sequences were shown in Table 1.

Western blot analysis

Total protein was extracted using protein lysate (cat. no. P0013; Beyotime, China), and quantified by BCA protein kit (cat. no. P0009; Beyotime). After denaturation, the total protein was separated by SDS-PAGE and transferred to the PVDF membrane (cat. no. ISEQ00010; Sigma-Aldrich, United States). The PVDF membranes were blocked with 5% skim milk for 2 h, then incubated with the corresponding primary antibody at 4°C overnight, and the secondary antibody at room temperature for 2 h for immune response. The protein was visualized by ECL luminescent solution (cat. no. KF001; Affinity, United States) through the chemiluminescence gel imager (Tanon, China). The primary antibodies BMP2 (cat. no. AF5163), PCAN (cat. no. DF10168), p38 (cat. no. AF6456) and p-p38 (cat. no. AF4001) were purchased from Affinity (United States); Bax (cat. no. ab32503), Bcl-2 (cat. no. ab182858), FOXP3 (cat. no. ab215206), Smad1 (cat. no. ab33902), p-Smad1 (cat. no. ab226821), Smad2 (cat. no.

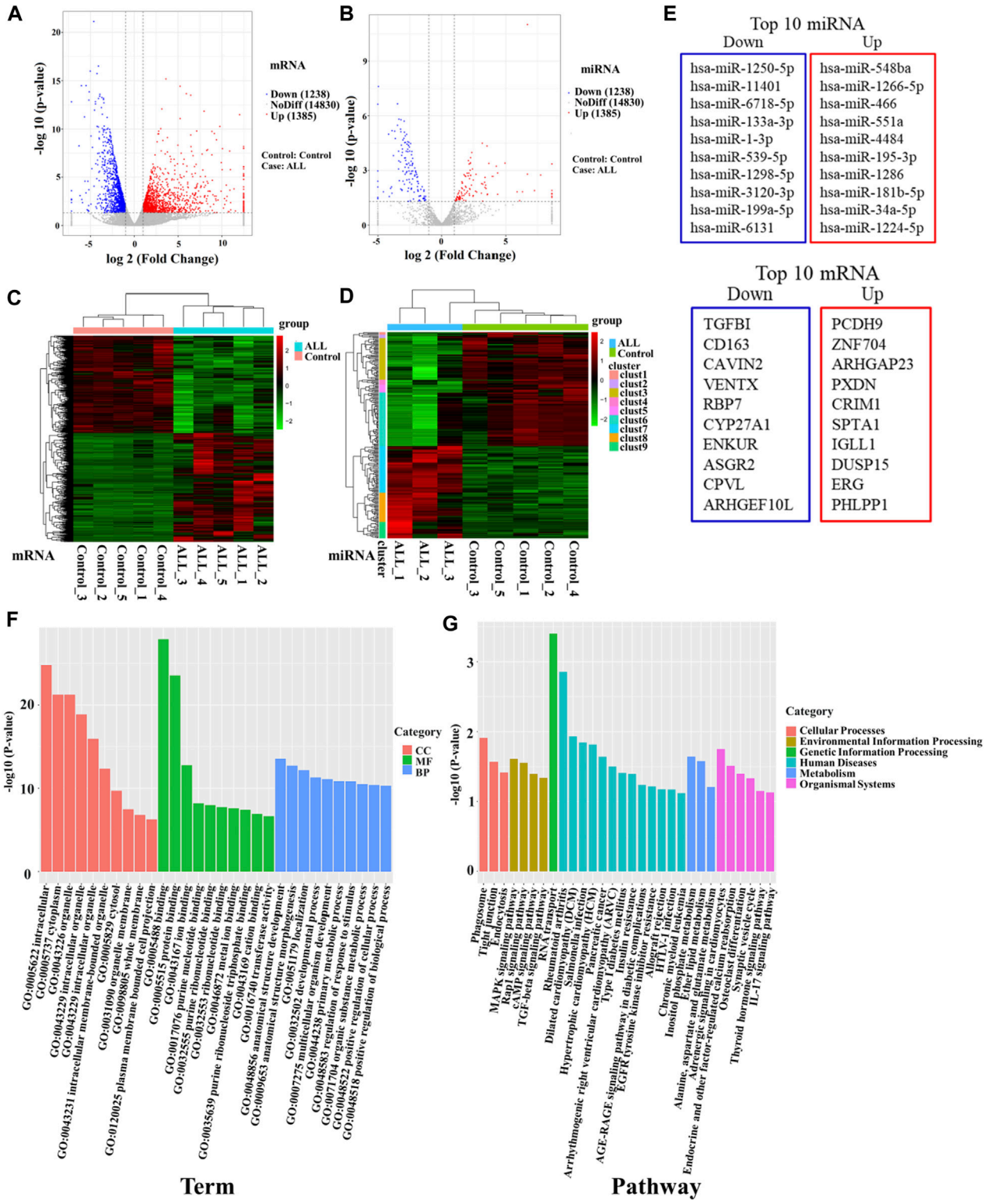

FIGURE 1
High-throughput sequencing was used to screen differentially expressed genes between B-ALL and controls. **(A)** Volcano map of differentially expressed mRNAs. **(B)** Volcano map of differentially expressed miRNAs. Red dots indicate upregulated genes, blue dots indicate downregulated genes. **(C)** Cluster analysis of differentially expressed mRNAs. **(D)** Cluster analysis of differentially expressed miRNAs. Horizontal represents genes, and each column is a sample. Red indicates high expression and green indicates low expression. **(E)** The top 10 differentially up-regulated and

(*Continued*)

FIGURE 1 (Continued)
down-regulated miRNAs and mRNAs. **(F)** Bar chart of GO enrichment analysis of differentially expressed miRNAs. **(G)** Bar graph of KEGG pathway enrichment analysis of differentially expressed miRNAs. GO: gene ontology; KEGG: Kyoto Encyclopedia of Genes and Genomes.

ab33875) and p-Smad2 (cat. no. ab188334) were purchased from Abcam (United Kingdom); ERK1/2 (cat. no. 11257-1-AP), JNK1/2 (cat. no. 66210-1-lg) and p-JNK1/2 (cat. no. 80024-1-RR) were purchased from Proteintech (United States); p-ERK1/2 (cat. no. AP0472) and β-actin (cat. no. AC026); were purchased from abclonal (China). Biotinylated goat anti-rabbit IgG (H+L) (cat. no. ab6721) and goat anti-mouse IgG (H+L) (cat. no. ab6789) were purchased from Abcam (United Kingdom).

Statistical analysis

All statistical results were analyzed using SPSS version 29.0 software package (IBM Corp., Armonk, NY United States). The Shapiro-Wilk test was used to check whether the data conform to the normal distribution. The data conforming to the normal distribution were expressed as mean ± standard deviation. And the difference between the two groups was analyzed by student's t-test, and the difference among multiple groups was analyzed by one-way analysis of variance. $p < 0.05$ was considered statistically significant.

Results

Transcriptome sequencing of PBMCs in B-ALL

The expression characteristics of mRNA and miRNA in PBMCs were analyzed by microarray sequencing. In this study, five samples from the B-ALL and control groups were used for transcriptome mRNA expression analysis. Since only three samples in the B-ALL group were eligible for miRNA analysis, there were three cases in the B-ALL group and five cases in the control group in miRNA analysis. A total of 1,666 miRNA and 17,453 mRNA were obtained in this study. The results of the differential statistics were represented by volcanic maps (Figures 1A, B). Compared with the control group, there were 2,623 differentially expressed mRNAs in the B-ALL group, 1,385 mRNAs were significantly up-regulated and 1,238 were significantly down-regulated (Figure 1A). There were 239 differentially expressed miRNAs, 107 were significantly up-regulated and 132 were significantly down-regulated (Figure 1B). A total of 239 differentially expressed miRNAs were predicted to have a total of 18,319 target genes corresponding to 38,188 target sites. Bidirectional cluster analysis of the differential genes and samples showed that the mRNA and miRNA expression clusters of B-ALL were significantly different from those of the control group (Figures 1C, D). The statistics of the top 10 differentially up-regulated and down-regulated miRNAs and mRNA were shown in Figure 1E.

To further clarify the functions of differentially expressed genes, we conducted an enrichment analysis. The GO enrichment analysis results of differentially expressed miRNA target genes showed that they were mainly enriched in intracellular, cytoplasm, organelle, binding, protein binding, and anatomical structure development, these differentially expressed target genes may play an important role in regulating cell development (Figure 1F). KEGG pathways enrichment were shown in Figure 1G. The results suggest that differentially expressed miRNA target genes had significant differences in regulating cell proliferation, survival and apoptosis, including the TGF-beta signaling pathway, Rap1 signaling pathway, cAMP signaling pathway and MAPK signaling pathway. MiRNAs regulating these pathways may be involved in the abnormal proliferation of B lymphocytes in ALL (Table 2). Among them, the TGF-β signaling pathway has the highest enrichment factor and also has significant differences ($p < 0.05$, Table 2). The involved differentially expressed miRNAs and differentially expressed target genes were analyzed, and miR-539-5p and BMP2 were preliminarily screened (Table 2).

miR-539-5p/BMP2 was associated with Treg activation in B-ALL

To verify the accuracy of the sequencing data, blood samples were collected from 20 B-ALL patients and 15 controls. The miRNAs with significant expression differences were selected from the sequencing data, among which miR-548ba, miR-1266-5p, miR-466, miR-551a and miR-4484 were the top five miRNAs with up-regulated multiples, miR-539-5p, miR-1-3p, miR-133a-3p, miR-6718-5p, miR-11401 and miR-1250-5p were the top 6 miRNAs that found to be down-regulated, and the results of sequencing data were verified by RT-PCR. As shown in Figure 2A, the RT-PCR results were consistent with the sequencing results ($p < 0.001$). In addition, in order to study the relationship between the differential expression of miRNA and the proportion of Treg in peripheral blood of children with B-ALL, we divided B-ALL children into low expression group and high expression group with the median expression of each differentially expressed miRNA as the critical value, and analyzed

TABLE 2 miRNAs and their target genes in KEGG enrichment pathways related to cell proliferation and activation.

KEGG pathway	ID	Rich factor	*p*-value	FDR	miRNA		Target EDGs	
TGF-beta signaling pathway	hsa04350	0.976	0.046	0.68	hsa-miR-3176	up	TGF-β1	down
					hsa-miR-3120-3p	down	TGF-β2	up
					hsa-miR-6852-3p	down	SMAD1	up
					hsa-miR-539-5p	**down**	**BMP2**	**up**
Rap1 signaling pathway	hsa04015	0.961	0.028	0.65	hsa-miR-548ba	up	RAP1A	down
					hsa-miR-654-5p	down	RAP1GAP	up
MAPK signaling pathway	hsa04010	0.956	0.025	0.65	hsa-miR-1286	up	RASGRP4	down
					hsa-miR-96-5p	up	RASGRP3	down
cAMP signaling pathway	hsa04024	0.959	0.040	0.65	hsa-miR-1-3p	down	RAPGEF3	up
					hsa-miR-6718-5p	down	ATP2B4	up

The bold values are the miRNA and its target genes screened in this study.

whether there was a difference in the proportion of Treg between the low expression group and the high expression group. The results showed that there was no statistical significance in the proportion of Treg between miR-548ba (median: 3.03), miR-1266-5p (median: 1.53), miR-466 (median: 1.81), miR-4484 (median: 2.10), miR-1-3p (median: 0.73), miR-133a-3p (median: 0.68), miR-6718-5p (median: 0.71), miR-11401 (median: 0.59), and miR-1250-5p (median: 0.46) low expression group and high expression group ($p > 0.05$, Figure 2B). Only miR-551a (median: 2.07) and miR-539-5p (median: 0.67) had significant differences in the proportion of Treg cells between the low and high expression groups ($p < 0.01$, Figure 2B). Therefore, we further identified miR-539-5p as the object of follow-up research. Then, the expressions of TGF-β1, TGF-β2, IL-35 and IL-10 in the serum of B-ALL were analyzed by ELISA, which showed that TGF-β1, IL-35 and IL-10 were significantly increased in the B-ALL group ($p < 0.01$, Figure 2C). The proportion of Treg was significantly higher in the B-ALL group than that in the control group ($p < 0.05$, Figures 2D, E). Correlation analysis showed that the proportion of Treg was significantly negatively correlated with the expression of miR-539-5p (Figure 2F). In addition, the expression of BMP2 in serum was analyzed by ELISA, which showed that the level of BMP2 in the B-ALL group was significantly higher than that in the control group ($p < 0.001$, Figure 2G), and the proportion of Treg was significantly positively correlated with the expression of BMP2 ($p < 0.05$, Figure 2H). RT-PCR results also showed that the gene expression of BMP2 in the B-ALL group was significantly higher than that in the control group ($p < 0.001$, Figure 2I), and it was significantly negatively correlated with the gene expression of miR-539-5p ($p < 0.05$, Figure 2J). These results indicated that miR-539-5p could significantly regulate the gene expression and secretion of BMP2 to participate in Treg activation in B-ALL.

miR-539-5p directly targets BMP2

To further clarify whether there is a clear targeting relationship between miR-539-5p and BMP2, TargetScan was used to analyze the possible binding sites between miR-539-5p and BMP2 3′UTR. The result was shown in Figure 3A. After transfecting H293T cells with a 5 pmol NC mimic or miR-539-5p mimic, the gene expression of miR-539-5p was detected by RT-PCR, and results showed that miR-539-5p expression in the miR-539-5p mimic group was significantly increased compared with that of the NC mimic group ($p < 0.01$, Figure 3B). Then, the relationship between miR-539-5p and BMP2 was verified by double luciferase reporter assay (Figure 3C). The results showed that there was no significant difference in luciferase activity between NC-mimic+BMP2-Mut and miR-539-5p-mimic+BMP2-Mut groups ($p > 0.05$), while the luciferase activity was significantly decreased in the miR-539-5p-mimic+BMP2-WT group compared with NC-mimic+BMP2-WT group ($p < 0.001$), indicating that miR-539-5p directly targeted the 3′UTR region of BMP2, thereby affecting BMP2 gene expression.

Effects of miR-539-5p/BMP2 on proliferation and apoptosis of Nalm-6 cells

To clarify the role of the downstream target gene BMP2 in B-ALL cells, BMP2-siRNA and pcDNA-BMP2 were constructed to transfect Nalm-6 cells. The transfection efficiency analysis by WB showed that the protein expression of BMP2 was significantly reduced in the BMP2-siRNA group compared with the NC-siRNA, and was significantly increased in the pcDNA-BMP2 group compared with the pcDNA-NC group ($p < 0.001$, Figure 4A). In addition, compared with NC-siRNA or pcDNA-NC group, the BMP2-siRNA group significantly inhibited cell proliferation activity ($p < 0.05$, Figure 4B), promoted cell apoptosis

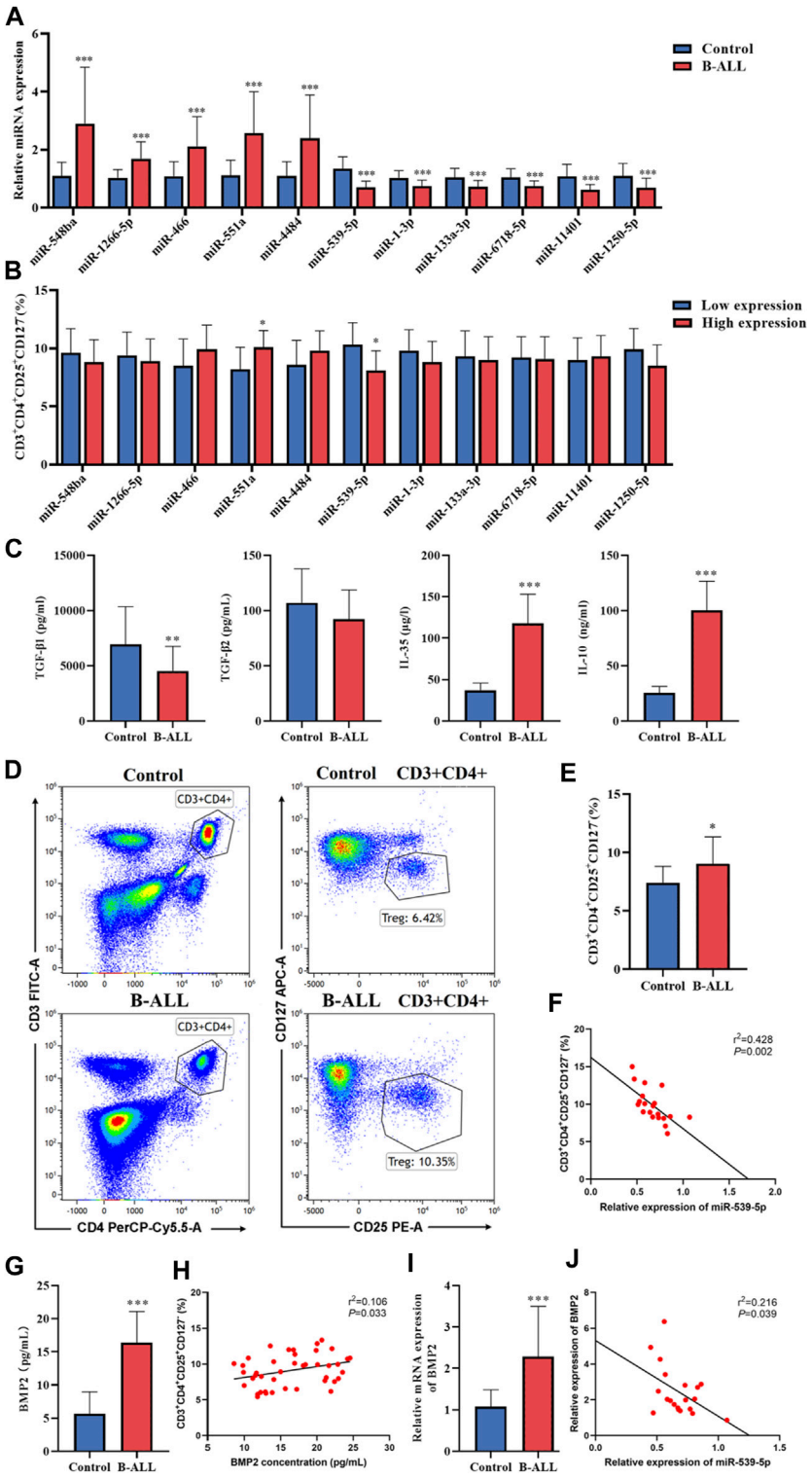

FIGURE 2
Expression of miR-539-5p/BMP2 in B-ALL and its relationship with Treg activation. **(A)** RT-PCR was used to verify the differential expressed miRNAs in more clinical samples. **(B)** With the median of differentially expressed miRNA expression as the critical value, B-ALL children were divided into low expression group and high expression group, and the proportion of Treg was analyzed. **(C)** The expressions of TGF-β1, TGF-β2, IL-35 and IL-10 in serum were detected by ELISA. **(D)** The proportion of Treg in peripheral blood was detected by flow cytometry. **(E)** Statistical bar graph of flow cytometry. **(F)** Correlation between miR-539-5p expression level and Treg ratio in B-ALL. **(G)** Serum BMP2 content was detected by ELISA. **(H)** (*Continued*)

FIGURE 2 (Continued)
Correlation between BMP2 concentration and Treg ratio in B-ALL. **(I)** The gene expression of BMP2 was detected by RT-PCR. **(J)** Correlation between expression levels of miR-539-5p and BMP2 in B-ALL. *$p < 0.05$, **$p < 0.01$, ***$p < 0.001$.

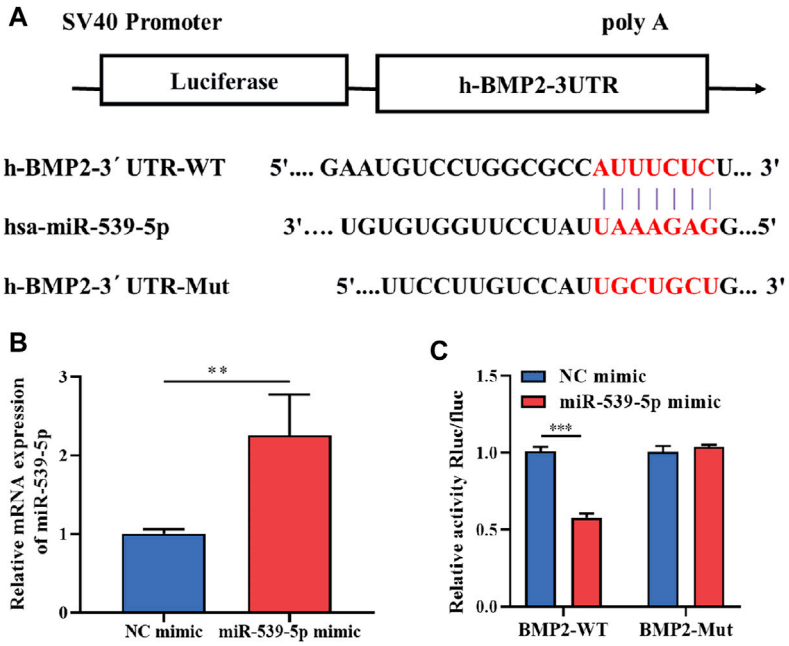

FIGURE 3
Binding relationship between miR-539-5p and BMP2. **(A)** The predicted binding site of miR-539-5p and BMP2 3′UTR. **(B)** RT-PCR was used to detect the gene expression of miR-539-5p after transfecting NC mimic or mir-539-5p mimic. **(C)** Double luciferase reporter assay to verify the binding relationship between miR-539-5p and BMP2. *$p < 0.05$, **$p < 0.01$, ***$p < 0.001$.

($p < 0.001$, Figures 4C, D), increased the protein expression of Bax, and decreased the protein expression of Bcl-2 and PCN2 ($p < 0.05$, Figures 4E, F), while pcDNA-BMP2 group showed the opposite effect (Figures 4B–F). These results suggested that BMP2, as the downstream target gene of miR-539-5p, could significantly promote cell viability and inhibit apoptosis in Nalm-6 cells.

On this basis, we further analyzed the effects of miR-539-5p regulation of BMP2 on the proliferation and apoptosis of Nalm-6 cells. MiR-539-5p mimic and/or pcDNA-BMP2 were used to co-transfect Nalm-6 cells, and RT-PCR analysis showed that compared with the NC-mimic group, miR-539-5p-mimic significantly increased the gene expression of miR-539-5p ($p < 0.05$, Figure 5A). In addition, the expression analysis of BMP2 by RT-PCR and WB showed that miR-539-5p-mimic significantly decreased the gene and protein expressions of BMP2 compared with the NC-mimic group ($p < 0.05$, Figures 5B, C). And compared with the miR-539-5p-mimic+pcDNA-NC group, miR-539-5p-mimic+pcDNA-BMP2 significantly decreased the gene expression of miR-539-5p ($p < 0.05$, Figure 5A), and promoted the gene and protein expression of BMP2 ($p < 0.05$, Figures 5B, C). Analysis of the proliferation and apoptosis activity of Nalm-6 cells showed that miR-539-5p-mimic significantly decreased the cell viability ($p < 0.05$, Figure 5D), promoted apoptosis ($p < 0.001$, Figures 5E, F), increased the protein expression of Bax, and decreased the protein expression of Bcl-2 and PCN2 compared with NC mimic group ($p < 0.05$, Figures 5G, H). Compared with the miR-539-5p-mimic+pcDNA-NC group, miR-539-5p-mimic+pcDNA-BMP2 significantly reversed the effects of miR-539-5p-mimic on Nalm-6 cells. These results suggested that miR-539-5p might inhibit Nalm-6 cell proliferation and promote apoptosis by targeting BMP2.

Nalm-6 cell synergies with TGF-β1 to promote Treg activation through TGF-β1/Smads/MAPK pathways

To explore the effects of Nalm-6 cells on Treg activation, the culture supernatant of Nalm-6 cells was collected and incubated with human peripheral blood $CD4^+CD25^-$T cell induction

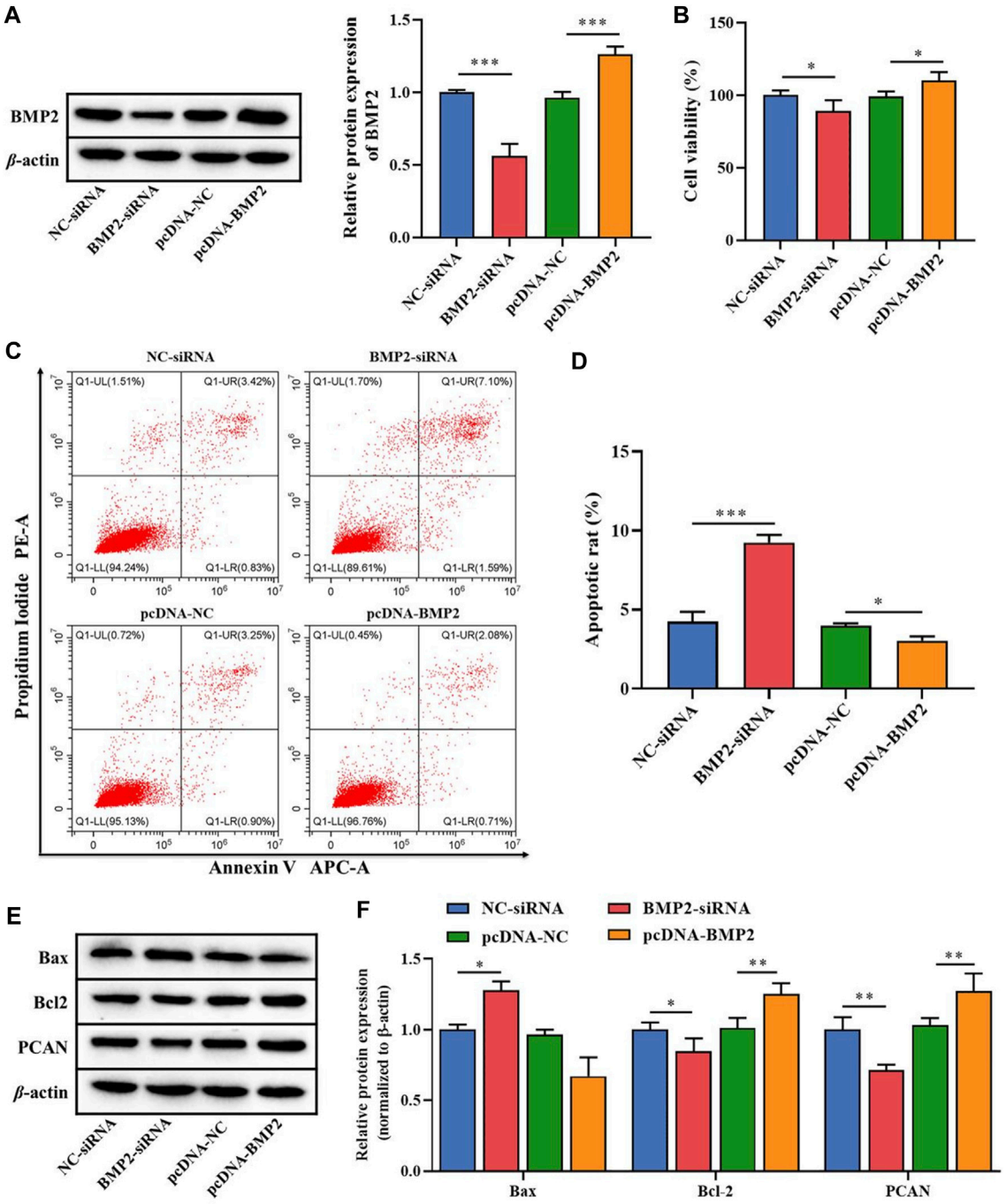

FIGURE 4
Effects of miR-539-5p downstream gene BMP2 on proliferation and apoptosis of Nalm-6 cells. **(A)** After transfection with BMP2-siRNA or pcDNA-BMP2, the protein expression of BMP2 was detected by WB to verify the transfection efficiency. **(B)** CCK8 was used to detect the viability of Nalm-6 cells after intervention or overexpression of BMP2. **(C)** The apoptosis of Nalm-6 cells was detected by flow cytometry. **(D)** Histogram of percentage of apoptotic cells. **(E)** The protein expressions of Bax, Bcl-2 and PCAN were detected by WB. **(F)** Histogram of gray level analysis of protein bands. $*p < 0.05$, $**p < 0.01$, $***p < 0.001$.

medium at a ratio of 1:1 to stimulate Treg differentiation. The results showed that in the absence of TGF-β1 stimulation, the culture supernatant of Nalm-6 cells treated with different treatments could not directly induce the expression of Foxp3 in $CD4^+CD25^-$T cells ($p > 0.05$, Figures 6A–D). Compared with the control group, TGF-β1 significantly

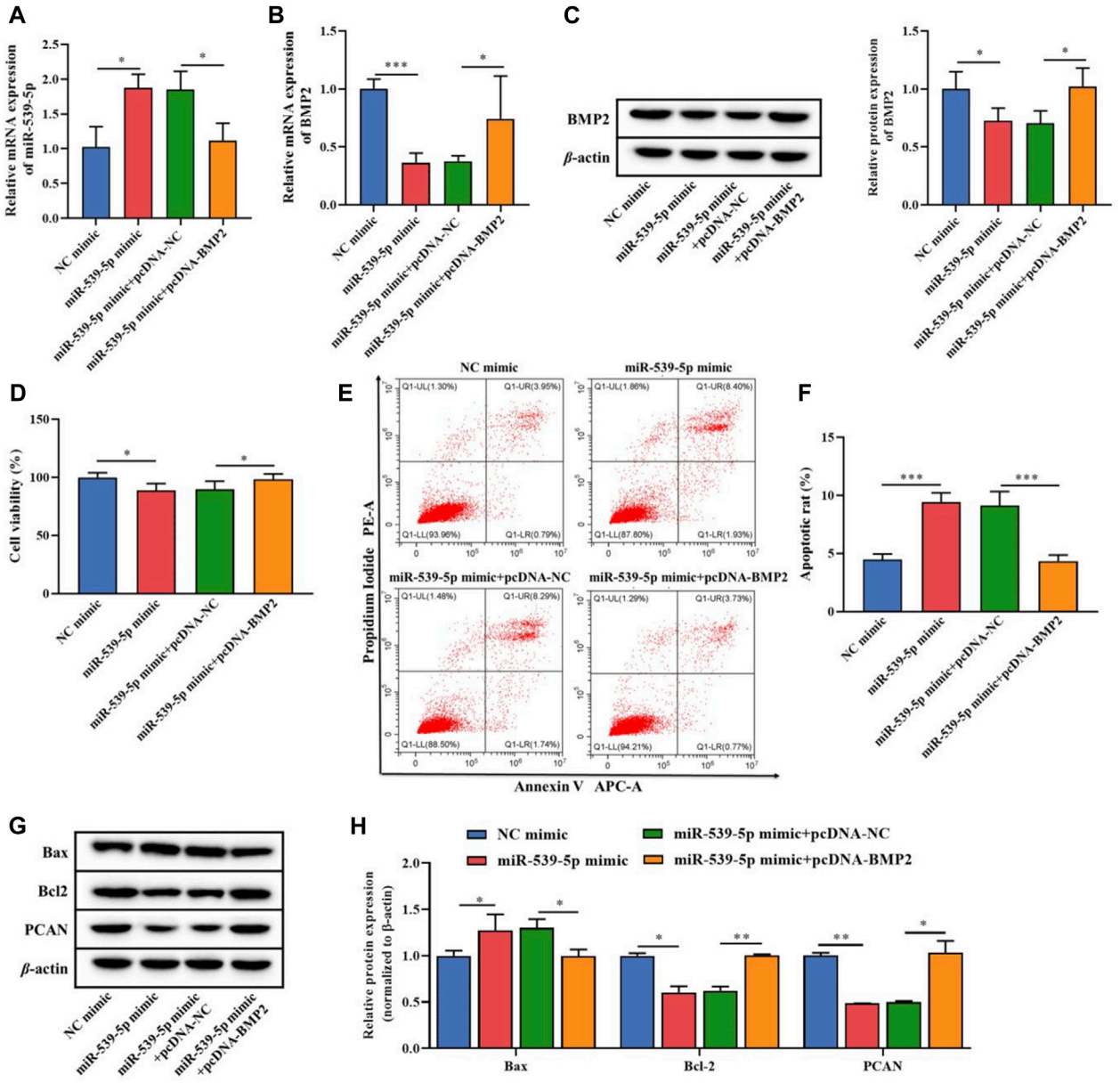

FIGURE 5
Effects of miR-539-5p/BMP2 regulatory axis on proliferation and apoptosis of Nalm-6 cells. After transfection of Nalm-6 cells with miR-539-5p-mimic and/or pcDNA-BMP2, the gene expression of miR-539-5p **(A)** and BMP2 **(B)** was detected by RT-PCR. **(C)** The protein expression of BMP2 was detected by WB. **(D)** CCK8 was used to detect the viability of Nalm-6 cells. **(E)** The apoptosis of Nalm-6 cells was detected by flow cytometry. **(F)** Histogram of percentage of apoptotic cells. **(G)** The protein expressions of Bax, Bcl-2 and PCAN were detected by WB. **(H)** Histogram of gray level analysis of protein bands. *$p < 0.05$, **$p < 0.01$, ***$p < 0.001$.

induced the Foxp3$^+$ proportion (Figures 6A, B) and Foxp3 expression (Figures 6C, D) in CD4$^+$CD25$^-$T cells ($p < 0.001$), and also increased the mRNA expression levels of cytokines TGF-β1, IL-10 and IL-35 ($p < 0.01$, Figure 6E). When simultaneously stimulated with TGF-β1, the culture supernatant of Nalm-6 cells could further enhance the promoting effects of TGF-β1, showing a synergistic effect with TGF-β1 ($p < 0.001$, Figures 6A–D). In addition, the supernatant of miR-539-5p-mimic and BMP2-siRNA transfected cells attenuated the synergistic effect between the Nalm-6 cell supernatant and TGF-β1 ($p < 0.001$, Figures 6A–D). Similarly, in cell proliferation experiments, we also found that the culture supernatant of Nalm-6 cells in each group could promote the proliferation of CD4$^+$CD25$^-$T cells induced by TGF-β1, showing

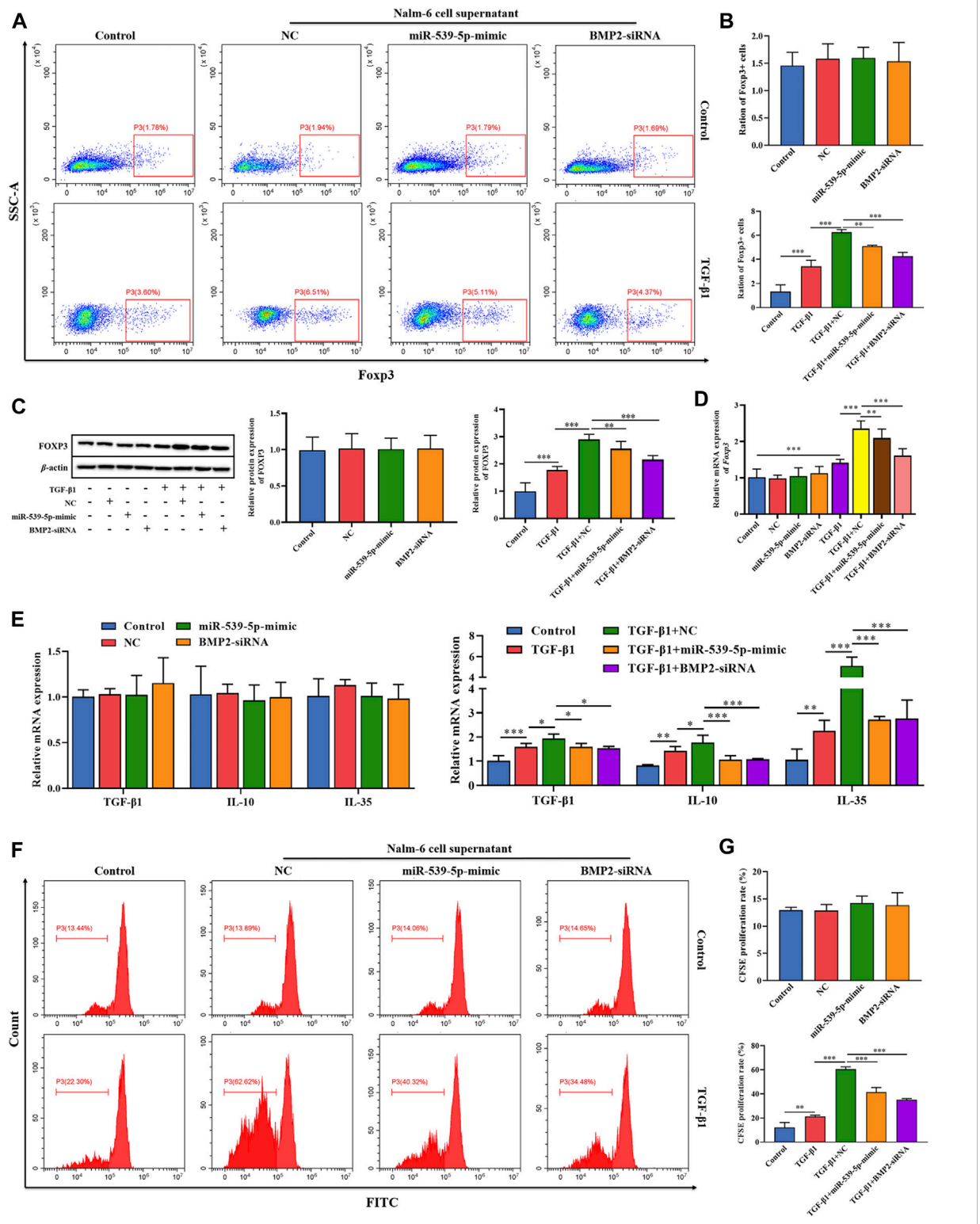

FIGURE 6
Effects of miR-539-5p/BMP2 in Treg activation induced by Nalm-6 cells. **(A)** The effect of different induction methods on the proportion of Foxp3⁺ was detected by flow cytometry. **(B)** Statistical results of Foxp3⁺ cell percentage. **(C)** The effect of different induction methods on Foxp3 protein expression was detected by WB. **(D)** Foxp3 gene expression was detected by RT-PCR. **(E)** The effects of different induction methods on

(*Continued*)

FIGURE 6 (Continued)
the gene expressions of TGF-β1, IL-10 and IL-35 were detected by RT-PCR. **(F)** The proliferation activity was analyzed by CFSE. **(G)** Statistical results of CFSE proliferation rate. *$p < 0.05$, **$p < 0.01$, ***$p < 0.001$.

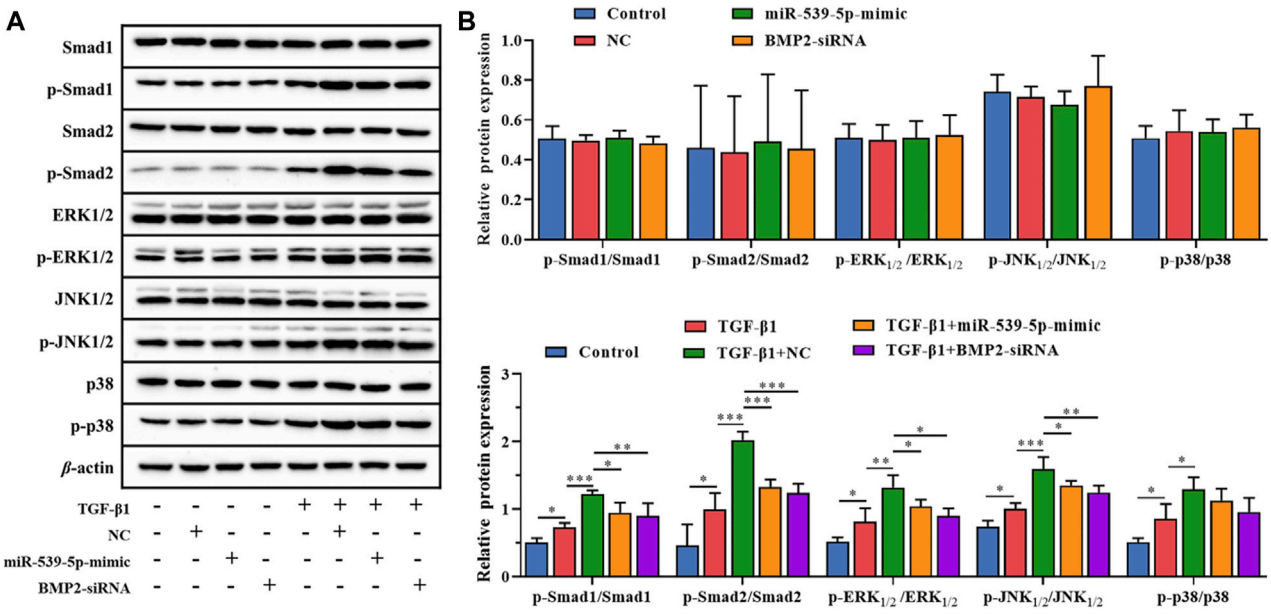

FIGURE 7
Effects of miR-539-5p/BMP2 on TGF-β/Smads/MAPK pathway in Treg induced by Nalm-6 cells. **(A)** The protein expressions of Smad1, p-Smad1, Smad2, p-Smad2, ERK1/2, p-ERK1/2, JNK1/2, p-JNK1/2, p38 and p-p38 were detected by WB. **(B)** Histogram of gray level analysis of protein bands. *$p < 0.05$, **$p < 0.01$, ***$p < 0.001$.

a synergistic effect with TGF-β1 ($p < 0.001$, Figures 6F, G). However, after transfected with miR-539-5p-mimic or BMP2-siRNA, the synergistic effect between the Nalm-6 cells and TGF-β1 decreased ($p < 0.001$, Figures 6F, G). These experiments indicated that Nalm-6 cells could cooperate with TGF-β1 to stimulate $CD4^+CD25^-$T cells to differentiate into $Foxp3^+$Treg cells, which might be achieved by inhibiting miR-539-5p to promote BMP2 secretion.

In order to further clarify the downstream signaling pathway involved in Nalm-6 cells synergism with TGF-β1, the protein expressions of TGF-β/Smads/MAPK pathway in different treatment groups were detected (Figure 7). The results showed that compared with the control group, the supernatant of Nalm-6 cells alone could not promote the phosphorylation of Smad1, Smad2, ERK1/2, JNK and p38 in $CD4^+CD25^-$T cells ($p > 0.05$). TGF-β1 could significantly promote the phosphorylation of Smad1, Smad2, ERK1/2, JNK and p38 ($p < 0.05$). The induction and pro-phosphorylation effects were strongest when the supernatant of Nalm-6 cells was co-treated with TGF-β1 ($p < 0.05$). However, when TGF-β1 was treated with miR-539-5p-mimic and BMP2-siRNA supernatant, the induction and pro-phosphorylation effects were decreased, but still higher than those of the control group ($p < 0.001$). In conclusion, Nalm-6 cells and TGF-β1 cooperatively regulate TGF-β/Smads/MAPK pathways to promote Treg activation.

Effects of miR-539-5p/BMP2 on Treg induction in B-ALL mice

We further used Nalm-6 cells to construct the B-ALL model in NOD/SCID mice, and explored the effect of miR-539-5p/BMP2 on Treg activation *in vivo*. Firstly, analysis of the expression levels of miR-539-5p and BMP2 in PBMCs showed that in the miR-539-5p-mimic group, the mRNA expression level of miR-539-5p was significantly increased ($p < 0.001$, Figure 8A), and the level of BMP2 was significantly decreased ($p < 0.001$, Figure 8B). Overexpression of miR-539-5p also inhibited BMP2 levels in mice. Then, the Wraith-Giemsa staining results of mouse bone marrow tissues were shown in Figures 8A, C large number of abnormal lymphocytes were observed in the control and NC-mimic groups, with large volume, dysregulated nucleo-plasmic ratio, basophilic cytoplasm, and

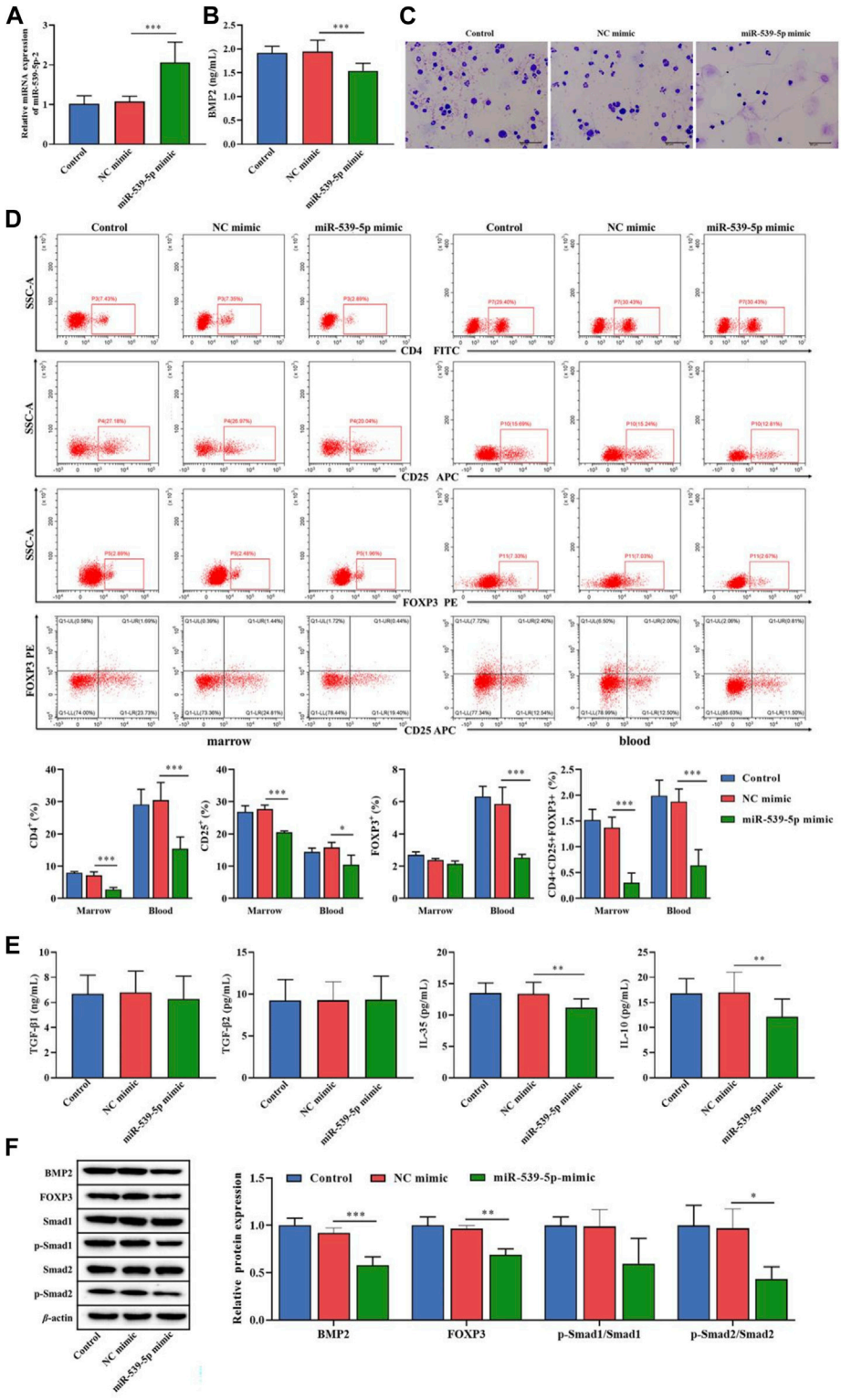

FIGURE 8
Effects of miR-539-5p/BMP2 on B-ALL mice *in vivo*. **(A)** RT-PCR was used to detect the expression of miR-539-5p in mouse PBMCs. **(B)** The content of BMP2 in plasma was detected by ELISA. **(C)** The cytopathic changes in bone marrow smears were observed by Wright-Giemsa staining. **(D)** The proportion of $CD4^+CD25^+Foxp3^+$Treg cells in the bone marrow and peripheral blood was detected by flow cytometry. **(E)** The expression of

(*Continued*)

FIGURE 8 (Continued)
TGF-β1, TGF-β2, IL-35 and IL-10 in plasma was detected by ELISA. **(F)** The protein expressions of BMP2, FOXP3, Smad1, p-Smad1, Smad2 and p-Smad2 in bone marrow were detected by WB. *$p < 0.05$, **$p < 0.01$, ***$p < 0.001$.

large and hyperchromatic nuclei. In the miR-539-5p-mimic group, no obvious abnormalities were observed in all types of cells under the microscope. Furthermore, analysis of the proportions of $CD4^+CD25^+Foxp3^+$Treg showed that the proportions of $CD4^+$, $CD25^+$ and $CD4^+CD25^+Foxp3^+$ in the bone marrow and peripheral blood of the miR-539-5p-mimic group were significantly lower than those of the NC-mimic group ($p < 0.001$, Figure 8D). ELISA assay of serum cytokine levels showed that the levels of IL-35 and IL-10 in miR-539-5p-mimic were significantly lower than those in the NC-mimic group ($p < 0.001$), but there was no significant difference in TGF-β1 and TGF-β2 among all groups ($p > 0.05$, Figure 8E). WB assay showed that miR-539-5p-mimic reduced the levels of BMP2, Foxp3 and p-Smad2/Smad2 ($p < 0.05$, Figure 8F). *In vivo* experiments confirmed that miR-539-5p-mimic could inhibit BMP2 secretion and Treg differentiation in B-ALL model mice.

Discussion

As an important regulatory factor of genes, miRNAs participate in physiological and pathological processes *in vivo*, and their abnormal expression is closely related to cancers [21]. In recent years, a large number of studies have confirmed that miRNA can directly participate in the cancer process [22], and can be used for the early clinical diagnosis, prognosis evaluation, chemotherapy drug resistance evaluation and toxicity prediction of cancers [23, 24]. Similarly, miRNAs can directly participate in ALL as proto-oncogenes or tumor suppressor genes [25], and may become an effective indicator related to B-ALL. In this study, the significantly low expression of miR-539-5p and its target gene BMP2 in B-ALL were screened out by high-throughput sequencing. Functional enrichment analysis showed that the main enrichment pathway involved the TGF-β pathway. Further analysis showed that miR-539-5p and BMP2 were significantly correlated with the proportion of Treg in B-ALL. *In vitro* and *in vivo* experiments confirmed that the low expression of miR-539-5p in B-ALL could directly target and promote BMP2 expression, and the increased BMP2 could further promote the proliferation and inhibit apoptosis of Nalm-6 cells, and cooperate with TGF-β1 to stimulate the differentiation of human $CD4^+CD25^-$T cells into Treg. TGF-β1/Smads/MAPK pathway played an important role in the regulation of Treg activation by miR-539-5p/BMP2.

MiRNA is a class of endogenous non-coding single-stranded small RNA, which is involved in the regulation of post-transcriptional gene expression by specifically binding to the target genes [26, 27]. MiR-539 has been confirmed as a suppressor factor in cancers, and plays an inhibitory role in a variety of cancers, including breast cancer [28], osteosarcoma [29], and pancreatic cancer [30]. However, there are no relevant research reports on miRNA-539-5p in B-ALL at present. Our study confirmed that the expression of miR-539-5p was significantly decreased in B-ALL, which may play a role in cancer suppression. There was a targeting site between miR-539-5p and BMP2, and miR-539-5p could negatively target the expression of BMP2 in B-ALL. BMP is a key regulator of various developmental stages and plays an important role in biological processes [31]. Studies have shown that BMP2 has a dual effect on tumorigenesis, which may promote [32–34] or inhibit [35] cancer progression. This study confirmed that BMP2 was significantly increased in B-ALL, and the high expression of BMP2 promoted the proliferation and inhibited the apoptosis of Nalm-6 cells, significantly decreased the expression of Bax, and increased the expression of Bcl-2 and PCNA. Bax is a regulator of Bcl-2 activity, both Bcl-2 and Bax play an important role in cell apoptosis [36, 37], and Bcl-2 is increased in most cancers, while Bax is decreased [38]. PCNA is a protein expressed in a specific phase of the cell cycle and is generally considered to be positively correlated with cancer cell proliferation [39]. In this study, further experiments suggested that miR-539-5p could regulate the proliferation and apoptosis of B-ALL cells by targeting BMP2.

BMP has been shown to promote T cell activation, and regulate the proliferative response of naive CD4+T cells [40]. When BMP signaling is inhibited, it leads to impaired maturation, differentiation and function of $Foxp3^+$ Treg [41]. Similarly, miRNA has also been shown to inhibit the function of immune cells and promote immune escape by regulating the proliferation and differentiation of immune cells, and the secretion of effectors in the tumor microenvironment [42]. The analysis of this study showed that the significantly low expression of miR-539-5p and its target gene BMP2 in B-ALL were both significantly correlated with the percentage of Treg in B-ALL. Treg cells, a subset of T cells, play a critical role in maintaining the homeostasis of the immune system [43]. In the tumor microenvironment, Treg can inhibit anti-tumor immune response and promote tumor immune escape, thus affecting the development of tumors [44]. The inhibitory adaptive immune response induced by Treg is mediated through the expression of TGF-β1 [45]. The inhibition ability of Treg induced by BMP2 and TGF-β1 is stronger than that induced by TGF-β1 alone [46]. In this study, we found that the culture supernatant of Nalm-6 cells could cooperate with TGF-β1 to promote the proportion of Foxp3+Treg and increase the expression of Foxp3 in $CD4^+CD25^-$T cells. Transfection with miR-539-5p-mimic and BMP2-siRNA attenuated the synergistic effect of Nalm-6 cells and TGF-β1 on Foxp3 promotion. Studies

have confirmed that Foxp3+Treg could be used as a therapeutic target to promote anti-tumor immunity [47]. Once Foxp3+Treg loses its transcription factor Foxp3, it will lose immunomodulatory function [48]. A recent relevant study recorded a slight insignificant increase in Treg cells in children with ALL compared to controls, and the increase in Treg appeared to occur due to a decrease in miR-155 [49]. A large number of studies have confirmed that miRNAs play an important role in the alteration of Treg in B-ALL [50]. Our study confirmed that miR-539-5p can regulate BMP2 to participate in Treg activation in B-ALL.

BMP belongs to the TGF-β superfamily, and a large number of studies have confirmed that TGF-β plays an important role in the inhibitory activity of $CD4^+CD25^+$T cells [51]. This study showed that the target genes of differentially expressed miR-539-5p in B-ALL were mainly enriched in the TGF-β pathway. TGF-β pathway is involved in cancer cell proliferation, differentiation, apoptosis and other functions [52]. When TGF-β binds specifically to the receptor, it initiates both classical Smad and non-Smad pathways [53]. MAPK pathway includes ERK, JNK and p38, which are the main signaling pathway for TGF-β to initiate non-Smad in cells [54]. Both Smad and non-Smad pathways are involved in the evolution of Treg differentiation induced by TGF-β [55]. This study found that the culture supernatant of Nalm-6 cells in collaboration with TGF-β1 could activate the phosphorylation of Smad1, Smad2, ERK, JNK and p38. In addition, the transfection of miR-539-5p-mimic and BMP2-siRNA inhibited the activation of the TGF-β1/Smads/MAPK pathway induced by Nalm-6 cells. These results suggested that the regulatory effect of Nalm-6 cells on Treg is achieved through the negative regulation of BMP2 by miR-539-5p to regulate the TGF-β1/Smads/MAPK pathway.

Conclusion

In conclusion, this study showed that miR-539-5p was one of the significantly down-regulated miRNAs in B-ALL and was significantly correlated with Treg expression, and BMP2 was the most differential expressed gene among miR-539-5p target genes, which was mainly enriched in the TGF-β pathway. The expression levels of miR-539-5p and BMP2 were both significantly correlated with the proportion of Tregs. *In vitro* and *in vivo* experiments confirmed that miR-539-5p could directly target BMP2, and the low expression of miR-539-5p in B-ALL resulted in significantly increased levels of BMP2. High BMP2 not only promoted Nalm-6 cell proliferation and inhibited apoptosis, but also cooperated with TGF-β1 to promote the expression of transcription factor Foxp3 to promote the differentiation of $CD4^+CD25^-$T cells into $Foxp3^+$Treg through the TGF-β1/Smads/MAPK pathways. This study demonstrated that miR-539-5p targeting BMP2 was involved in the Treg activation through the TGF-β1/Smads/MAPK pathway and played an important role in B-ALL.

Author contributions

GZ, YW, LY, LP, and HY conducted the experiments, SG and JH contributed to the data acquisition, QD and RS wrote the manuscript, and YJ contributed supervision. All authors contributed to the article and approved the submitted version.

Data availability statement

The original contributions presented in the study are included in the article/Supplementary Material, further inquiries can be directed to the corresponding author.

Ethics statement

The studies involving humans were approved by the Ethics Committee of West China Second University Hospital of Sichuan University. The studies were conducted in accordance with the local legislation and institutional requirements. Written informed consent for participation in this study was provided by the participants' legal guardians/next of kin. The animal study was approved by the Ethics Committee of West China Hospital of Sichuan University. The study was conducted in accordance with the local legislation and institutional requirements.

Funding

This work was supported by the Medical Science and Technology Project of Health Commission of Sichuan Province (No. 21PJ054).

Conflict of interest

The authors declare that the research was conducted in the absence of any commercial or financial relationships that could be construed as a potential conflict of interest.

Publisher's note

Please note that the review of this paper was conducted at the previous publisher, SAGE.

Supplementary material

The Supplementary Material for this article can be found online at: https://www.ebm-journal.org/articles/10.3389/ebm.2024.10111/full#supplementary-material

References

1. Siegel RL, Miller KD, Fuchs HE, Jemal A. Cancer statistics, 2022. *CA: A Cancer J Clinicians* (2022) **72**:7–33. doi:10.3322/caac.21708

2. Hunger SP, Mullighan CG. Acute lymphoblastic leukemia in children. *New Engl J Med* (2015) **373**:1541–52. doi:10.1056/nejmra1400972

3. Pui CH, Yang JJ, Bhakta N, Rodriguez-Galindo C. Global efforts toward the cure of childhood acute lymphoblastic leukaemia. *Lancet Child Adolescent Health* (2018) **2**:440–54. doi:10.1016/s2352-4642(18)30066-x

4. Vrooman LM, Silverman LB. Treatment of childhood acute lymphoblastic leukemia: prognostic factors and clinical advances. *Curr hematologic malignancy Rep* (2016) **11**:385–94. doi:10.1007/s11899-016-0337-y

5. Lv M, Liu Y, Liu W, Xing Y, Zhang S. Immunotherapy for pediatric acute lymphoblastic leukemia: recent advances and future perspectives. *Front Immunol* (2022) **13**:921894. doi:10.3389/fimmu.2022.921894

6. Romano G, Kwong LN. Diagnostic and therapeutic applications of miRNA-based strategies to cancer immunotherapy. *Cancer Metastasis Rev* (2018) **37**:45–53. doi:10.1007/s10555-017-9716-7

7. Bloom M, Maciaszek JL, Clark ME, Pui CH, Nichols KE. Recent advances in genetic predisposition to pediatric acute lymphoblastic leukemia. *Expert Rev Hematol* (2020) **13**:55–70. doi:10.1080/17474086.2020.1685866

8. Bhojwani D, Yang JJ, Pui CH. Biology of childhood acute lymphoblastic leukemia. *Pediatr Clin North America* (2015) **62**:47–60. doi:10.1016/j.pcl.2014.09.004

9. Buck MD, O'Sullivan D, Pearce EL. T cell metabolism drives immunity. *J Exp Med* (2015) **212**:1345–60. doi:10.1084/jem.20151159

10. Ostroumov D, Fekete-Drimusz N, Saborowski M, Kühnel F, Woller N. CD4 and CD8 T lymphocyte interplay in controlling tumor growth. *Cell Mol Life Sci* (2018) **75**:689–713. doi:10.1007/s00018-017-2686-7

11. Huang Y, Ma C, Zhang Q, Ye J, Wang F, Zhang Y, et al. CD4+ and CD8+ T cells have opposing roles in breast cancer progression and outcome. *Oncotarget* (2015) **6**:17462–78. doi:10.18632/oncotarget.3958

12. Akkaya B, Shevach EM. Regulatory T cells: master thieves of the immune system. *Cell Immunol* (2020) **355**:104160. doi:10.1016/j.cellimm.2020.104160

13. Minton K. Regulatory T cells: subset-specific suppression. *Nat Rev Immunol* (2017) **17**:401. doi:10.1038/nri.2017.68

14. Li C, Jiang P, Wei S, Xu X, Wang J. Regulatory T cells in tumor microenvironment: new mechanisms, potential therapeutic strategies and future prospects. *Mol Cancer* (2020) **19**:116. doi:10.1186/s12943-020-01234-1

15. Ohue Y, Nishikawa H. Regulatory T (Treg) cells in cancer: can Treg cells be a new therapeutic target? *Cancer Sci* (2019) **110**:2080–9. doi:10.1111/cas.14069

16. Bhattacharya K, Chandra S, Mandal C. Critical stoichiometric ratio of CD4(+) CD25(+) FoxP3(+) regulatory T cells and CD4(+) CD25(-) responder T cells influence immunosuppression in patients with B-cell acute lymphoblastic leukaemia. *Immunology* (2014) **142**:124–39. doi:10.1111/imm.12237

17. Bam M, Yang X, Sen S, Zumbrun EE, Dennis L, Zhang J, et al. Characterization of dysregulated miRNA in peripheral blood mononuclear cells from ischemic stroke patients. *Mol Neurobiol* (2018) **55**:1419–29. doi:10.1007/s12035-016-0347-8

18. Gardiner E, Beveridge NJ, Wu JQ, Carr V, Scott RJ, Tooney PA, et al. Imprinted DLK1-DIO3 region of 14q32 defines a schizophrenia-associated miRNA signature in peripheral blood mononuclear cells. *Mol Psychiatry* (2012) **17**:827–40. doi:10.1038/mp.2011.78

19. Ding W, Xin J, Jiang L, Zhou Q, Wu T, Shi D, et al. Characterisation of peripheral blood mononuclear cell microRNA in hepatitis B-related acute-on-chronic liver failure. *Scientific Rep* (2015) **5**:13098. doi:10.1038/srep13098

20. Yan W, Song L, Wang H, Yang W, Hu L, Yang Y. Extracellular vesicles carrying miRNA-181b-5p affects the malignant progression of acute lymphoblastic leukemia. *J translational Med* (2021) **19**:511. doi:10.1186/s12967-021-03174-w

21. Rupaimoole R, Slack FJ. MicroRNA therapeutics: towards a new era for the management of cancer and other diseases. *Nat Rev Drug Discov* (2017) **16**:203–22. doi:10.1038/nrd.2016.246

22. Hill M, Tran N. miRNA interplay: mechanisms and consequences in cancer. *Dis models Mech* (2021) **14**:dmm047662. doi:10.1242/dmm.047662

23. Sempere LF, Azmi AS, Moore A. microRNA-based diagnostic and therapeutic applications in cancer medicine. *Wiley Interdisciplinary Reviews RNA* (2021) **12**:e1662. doi:10.1002/wrna.1662

24. Svoronos AA, Engelman DM, Slack FJ. OncomiR or tumor suppressor? The duplicity of MicroRNAs in cancer. *Cancer Res* (2016) **76**:3666–70. doi:10.1158/0008-5472.can-16-0359

25. Tapeh BEG, Alivand MR, Solali S. The role of microRNAs in acute lymphoblastic leukaemia: from biology to applications. *Cel Biochem Funct* (2020) **38**:334–46. doi:10.1002/cbf.3466

26. Lu TX, Rothenberg ME. MicroRNA. *J Allergy Clin Immunol* (2018) **141**:1202–7. doi:10.1016/j.jaci.2017.08.034

27. Lee I, Ajay SS, Yook JI, Kim HS, Hong SH, Kim NH, et al. New class of microRNA targets containing simultaneous 5'-UTR and 3'-UTR interaction sites. *Genome Res* (2009) **19**:1175–83. doi:10.1101/gr.089367.108

28. Cai F, Chen L, Sun Y, He C, Fu D, Tang J. MiR-539 inhibits the malignant behavior of breast cancer cells by targeting SP1. *Biochem Cel Biol* (2020) **98**:426–33. doi:10.1139/bcb-2019-0111

29. Liu H, Yang M, Zhang Y, Yang Z, Chen Z, Xie Y, et al. The effect of miR-539 regulating TRIAP1 on the apoptosis, proliferation, migration and invasion of osteosarcoma cells. *Cancer Cel Int* (2021) **21**:227. doi:10.1186/s12935-021-01909-9

30. Xue L, Shen Y, Zhai Z, Zheng S. miR-539 suppresses the proliferation, migration, invasion and epithelial mesenchymal transition of pancreatic cancer cells through targeting SP1. *Int J Mol Med* (2020) **45**:1771–82. doi:10.3892/ijmm.2020.4561

31. Brazil DP, Church RH, Surae S, Godson C, Martin F. BMP signalling: agony and antagony in the family. *Trends Cell Biology* (2015) **25**:249–64. doi:10.1016/j.tcb.2014.12.004

32. Fukuda T, Fukuda R, Koinuma D, Moustakas A, Miyazono K, Heldin CH. BMP2-induction of FN14 promotes protumorigenic signaling in gynecologic cancer cells. *Cell Signal* (2021) **87**:110146. doi:10.1016/j.cellsig.2021.110146

33. Fukuda T, Fukuda R, Miyazono K, Heldin CH. Tumor promoting effect of BMP signaling in endometrial cancer. *Int J Mol Sci* (2021) **22**:7882. doi:10.3390/ijms22157882

34. Wu CK, Wei MT, Wu HC, Wu CL, Wu CJ, Liaw H, et al. BMP2 promotes lung adenocarcinoma metastasis through BMP receptor 2-mediated SMAD1/5 activation. *Scientific Rep* (2022) **12**:16310. doi:10.1038/s41598-022-20788-2

35. Chen Z, Yuan L, Li X, Yu J, Xu Z. BMP2 inhibits cell proliferation by downregulating EZH2 in gastric cancer. *Cell Cycle (Georgetown, Tex)* (2022) **21**:2298–308. doi:10.1080/15384101.2022.2092819

36. Jensen K, WuWong DJ, Wong S, Matsuyama M, Matsuyama S. Pharmacological inhibition of Bax-induced cell death: bax-inhibiting peptides and small compounds inhibiting Bax. *Exp Biol Med (Maywood, NJ)* (2019) **244**:621–9. doi:10.1177/1535370219833624

37. Spitz AZ, Gavathiotis E. Physiological and pharmacological modulation of BAX. *Trends Pharmacological Sciences* (2022) **43**:206–20. doi:10.1016/j.tips.2021.11.001

38. Goldar S, Khaniani MS, Derakhshan SM, Baradaran B. Molecular mechanisms of apoptosis and roles in cancer development and treatment. *Asian Pac J Cancer Prev* (2015) **16**:2129–44. doi:10.7314/apjcp.2015.16.6.2129

39. González-Magaña A, Blanco FJ. Human PCNA structure, function and interactions. *Biomolecules* (2020) **10**:570. doi:10.3390/biom10040570

40. Martínez VG, Sacedón R, Hidalgo L, Valencia J, Fernández-Sevilla LM, Hernández-López C, et al. The BMP pathway participates in human naive CD4+ T cell activation and homeostasis. *PloS one* (2015) **10**:e0131453. doi:10.1371/journal.pone.0131453

41. Yoshioka Y, Ono M, Osaki M, Konishi I, Sakaguchi S. Differential effects of inhibition of bone morphogenic protein (BMP) signalling on T-cell activation and differentiation. *Eur J Immunol* (2012) **42**:749–59. doi:10.1002/eji.201141702

42. Deng W, Pan M, Zhu S, Chao R, Wang L. Emerging roles of microRNAs in acute lymphoblastic leukemia and their clinical prospects. *Expert Rev Hematol* (2021) **14**:987–92. doi:10.1080/17474086.2021.2007763

43. Scheinecker C, Göschl L, Bonelli M. Treg cells in health and autoimmune diseases: new insights from single cell analysis. *J Autoimmun* (2020) **110**:102376. doi:10.1016/j.jaut.2019.102376

44. Tanaka A, Sakaguchi S. Targeting Treg cells in cancer immunotherapy. *Eur J Immunol* (2019) **49**:1140–6. doi:10.1002/eji.201847659

45. Moreau JM, Velegraki M, Bolyard C, Rosenblum MD, Li Z. Transforming growth factor-β1 in regulatory T cell biology. *Sci Immunol* (2022) **7**:eabi4613. doi:10.1126/sciimmunol.abi4613

46. Lu L, Ma J, Wang X, Wang J, Zhang F, Yu J, et al. Synergistic effect of TGF-β superfamily members on the induction of Foxp3$^+$ Treg. *Eur J Immunol* (2010) **40**:142–52. doi:10.1002/eji.200939618

47. Whiteside TL. FOXP3+ Treg as a therapeutic target for promoting anti-tumor immunity. *Expert Opin Ther Targets* (2018) **22**:353–63. doi:10.1080/14728222.2018.1451514

48. Dong Y, Yang C, Pan F. Post-translational regulations of Foxp3 in Treg cells and their therapeutic applications. *Front Immunol* (2021) **12**:626172. doi:10.3389/fimmu.2021.626172

49. El-Maadawy EA, Elshal MF, Bakry RM, Moussa MM, El-Naby S, Talaat RM. Regulation of CD4(+)CD25(+)FOXP3(+) cells in pediatric acute lymphoblastic leukemia (ALL): implication of cytokines and miRNAs. *Mol Immunol* (2020) **124**:1–8. doi:10.1016/j.molimm.2020.05.002

50. Zidan M, Zidan AA, Attia Saad M, El-Shanshory M, Bakry U, Sobh A, et al. Altered microRNA expression profile is linked to T-cell exhaustion-related pathways in pediatric patients with acute lymphoblastic leukemia. *Hum Immunol* (2023) **84**:113–22. doi:10.1016/j.humimm.2022.10.005

51. Chen W, Jin W, Hardegen N, Lei KJ, Li L, Marinos N, et al. Conversion of peripheral CD4+CD25− naive T cells to CD4+CD25+ regulatory T cells by TGF-β induction of transcription factor *Foxp3*. *J Exp Med* (2003) **198**:1875–86. doi:10.1084/jem.20030152

52. Syed V. TGF-B signaling in cancer. *J Cell Biochem* (2016) **117**:1279–87. doi:10.1002/jcb.25496

53. Derynck R, Zhang YE. Smad-dependent and Smad-independent pathways in TGF-β family signalling. *Nature* (2003) **425**:577–84. doi:10.1038/nature02006

54. Mu Y, Gudey SK, Landström M. Non-Smad signaling pathways. *Cel Tissue Res* (2012) **347**:11–20. doi:10.1007/s00441-011-1201-y

55. Kanamori M, Nakatsukasa H, Okada M, Lu Q, Yoshimura A. Induced regulatory T cells: their development, stability, and applications. *Trends Immunology* (2016) **37**:803–11. doi:10.1016/j.it.2016.08.012

EBM Experimental Biology and Medicine

TYPE Brief Communication
PUBLISHED 08 February 2024
DOI 10.3389/ebm.2024.10030

OPEN ACCESS

*CORRESPONDENCE
Stacey L. Gorniak,
sgorniak@uh.edu

RECEIVED 09 October 2023
ACCEPTED 16 January 2024
PUBLISHED 08 February 2024

CITATION
Gorniak SL, Meng H, Yazdekhasti S and Pollonini L (2024), Correlation between subcutaneous adipose tissue of the head and body mass index in children and young adults aged 8–19 years: implications for functional neuroimaging.
Exp. Biol. Med. 249:10030.
doi: 10.3389/ebm.2024.10030

Correlation between subcutaneous adipose tissue of the head and body mass index in children and young adults aged 8–19 years: implications for functional neuroimaging

Stacey L. Gorniak [1]*, Hao Meng [1], Saba Yazdekhasti [1] and Luca Pollonini [2,3,4]

[1]Department of Health and Human Performance, University of Houston, Houston, TX, United States, [2]Department of Engineering Technology, University of Houston, Houston, TX, United States, [3]Department of Electrical and Computer Engineering, University of Houston, Houston, TX, United States, [4]Department of Biomedical Engineering, University of Houston, Houston, TX, United States

Abstract

High body mass index (BMI) is presumed to signify high amounts of fat (subcutaneous adipose tissue) distributed across the body. High amounts of fat co-occurring with increased BMI has been cited as a potential neuroimaging barrier. Presence of increased fat may result in high electrical impedance and increased light diffusion—resulting in low signal to noise ratios during electroencephalography (EEG), functional near-infrared spectroscopy (fNIRS), and transcranial direct current stimulation (tDCS) measurements. Examining if subcutaneous fat in the head increases with respect to total body fat percentage and BMI in school-aged children and adolescents is an essential next step in developing possible mathematical corrections for neuroimaging modalities. We hypothesized that percentage of subcutaneous adipose tissue in the head region would increase with respect to both total body fat percentage and BMI. Increased subcutaneous head fat percentage was associated with a positive linear relationship with BMI and a quadratic relationship with total body fat. The data indicate that participant age, sex, and adiposity should be considered in the development of model corrections for neuroimaging signal processing in school-aged children and adolescents. Strength of regression coefficients in our models differed from those in adults, indicating that age-specific models should be utilized.

KEYWORDS

body fat, sex differences, EEG, fNIRS, obesity, tDCS, adolescents

Impact statement

This project serves to provide justification for the development of signal to noise correction algorithms for neuroimaging modalities such as electroencephalography (EEG), functional near infrared spectroscopy (fNIRS), and transcranial direct current stimulation (tDCS). Noise in each of these neuroimaging modalities exists due to differences in subcutaneous adiposity, sex, and age across participants. Consideration and correction of these sources of noise will have a significant clinical impact on reported outcomes and life-long treatments plans for pediatric patients.

Introduction

Increased body mass leading to overweight status or obesity is one of the most common health problems globally [1]. The World Health Organization (WHO) has recently estimated that more than 39 million school-aged children (aged 6–11 years) and 340 million adolescents (aged 12–19 years) are overweight or obese worldwide [2]. In the United States alone, over 20% of school-aged children and adolescents meet the criteria for obesity [3]. The definition of overweight is a Body Mass Index (BMI) ≥ 25 kg/m^2 and the definition of obesity is BMI ≥ and 30 kg/m^2, as per WHO guidelines [4]. High BMI is presumed to signify a large amount fat distributed across the body, whereas amount of body fat is measured via gold-standard techniques such as Dual-energy X-ray absorptiometry (DXA). Studies have shown that BMI differs from total body fat percentage across the lifespan [5, 6]. Specifically, it has been shown that BMI exhibits a non-linear relationship with body fat percentage that is impacted by both age and sex [5–7].

Despite the differences in adiposity measures, both high BMI and increased body fat are associated with the development of increased risk for cardiovascular diseases, metabolic disease (e.g., Type 2 Diabetes), musculoskeletal disease, cancer, and negative impacts to mental health across the lifespan [4, 8]. In recent years, increased subcutaneous adipose tissue has been cited as a barrier for non-invasive neuroimaging technologies, including electroencephalography (EEG), functional near infrared spectroscopy (fNIRS), and transcranial direct current stimulation (tDCS) [9, 10]. Recent interest in the impact of obesity on these neuroimaging technologies has manifested within the evidence base. In EEG [11–13] and tDCS [14, 15]-based research, the concern is that increased subcutaneous adipose tissue within the head may cause high electrical impedance and reduce the amplitude of signals detected through the derma during measurement. In fNIRS [16]-based research, the concern is that the increased subcutaneous adipose tissue will cause increased light diffusion from emitter optodes which will reduce the signal detected by the detector optodes during testing.

In each of these cases, the reduced signal strength to be detected during these evaluations is a major concern, leading to exclusion of participant or patient data due to low signal to noise ratios in individuals with increased amounts of adiposity. This exclusion is a form of phenotypic bias that disproportionally impacts underrepresented minorities, given the higher incidence of overweight and obesity in these populations [3, 17]. The presence of such phenotypic biases due to an inattention of adipose impacts on EEG, fNIRS, and tDCS signal to noise characteristics may reinforce and amplify gaps in assessment and treatment of significant life-long health conditions impacting neurological function and mental health in school-aged children and adolescents with increased adipose tissue, particularly in those individuals that belong to underrepresented minority groups [18].

As a countermeasure to these potential biases that can affect long-term health outcomes across the lifespan and disproportionally impacting underrepresented minority groups, adiposity should be considered as a potential confounder of cortical activity measurement occurring through the derma. Examining how subcutaneous adipose tissue in the head region increases with respect to percentage of total body fat and BMI in school-aged children and adolescents is an essential step in developing mathematical corrections to be implemented in these neuroimaging modalities, consisted with our prior findings in adults aged 20–89 years old [9].

Accordingly, the purpose of this project was to investigate how the percentage of subcutaneous adipose tissue in the head region in children and young adults aged 8–19 years is influenced by common adiposity metrics such as BMI and total body fat percentage. We hypothesized that percentage of subcutaneous adipose tissue in the head region would increase with respect to both percentage of total body fat percentage and BMI yet still carry influences of both age and sex, consistent with the adult models in our earlier work (Hypothesis 1). Consistent with our prior findings [9], we also expected total body fat to increase proportionally with BMI but that head fat percentage would increase modestly with BMI across the sample (Hypothesis 2). This information may be used by researchers and clinicians in improving neuroimaging signal to noise ratios for EEG, fNIRS, and tDCS data collected in pediatric populations as well as to avoid persistent exclusion biases due to physiologic characteristics (e.g., adiposity).

Materials and methods

Study participants

To evaluate the measures of interest for this study on a large scale, data from the National Health and Nutrition Examination Survey (NHANES) 2005–2006 were analyzed

TABLE 1 Age, anthropometry, BMI, total body fat %, and subcutaneous head fat % for each commonly referenced BMI range within the assessed data set.

	Normal weight (NW)		Overweight (OW)		Obese (OB)		Entire sample	
# Subjects	2,050		474		397		2,947	
Males:Females	1,052:998		214:260		176:221		1,455:1,492	
	Mean ± SD	[min–max]	Mean ± SD	[min–max]	Mean ± SD	[min–max]	Mean ± SD	[min–max]
Age (years)	13 ± 3	[8–19]	15 ± 3	[8–19]	16 ± 3	[8–19]	14 ± 3	[8–19]
Height (m)	1.57 ± 0.15	[1.12–2.00]	1.62 ± 0.12	[1.23–1.93]	1.65 ± 0.10	[1.38–1.97]	1.59 ± 0.15	[1.12–2.00]
Mass (kg)	49.85 ± 13.72	[20.00–88.20]	72.24 ± 11.31	[42.50–106.10]	97.21 ± 20.28	[61.20–215.3]	59.92 ± 22.19	[20.00–215.30]
BMI (kg/m^2)	19.82 ± 2.77	[12.41–24.99]	27.27 ± 1.40	[25.02–29.99]	35.17 ± 5.37	[30.04–62.08]	23.12 ± 6.30	[12.41–62.08]
Body fat (%)	26.29 ± 7.23	[10.10–46.80]	35.25 ± 7.46	[16.2–50.00]	40.33 ± 6.19	[25.20–58.00]	29.60 ± 8.90	[10.10–58.00]
Head fat (%)	23.78 ± 0.42	[21.90–25.70]	24.13 ± 0.68	[22.60–26.60]	24.53 ± 0.76	[22.90–27.40]	23.94 ± 0.59	[21.90–27.40]

Range of data [minimum–maximum] are included for reference.

[19]. This particular data set included a body composition scanning protocol via DXA for a sample of individuals aged 8–69 living in the United States in addition to typical NHANES anthropomorphic data. Data from individuals in the 8–19 years old age groups were included in this project. Data from individuals aged 20–69 were assessed in a different project [9], as the sampling rates for individuals aged 20+ years were different from the 8–19 year-old age group (NHANES purposefully oversampled individuals aged ≤19 years). The data set in this study included a wide variety of BMI values. Specifically, BMI values within the data set ranged from 12.41 kg/m^2 to 62.08 kg/m^2. Data from 2,947 participants were included in this analysis (1,455 males and 1,492 females). Of the 2,947 participants within the NHANES 2005–2006 data set, 26 had data reported on only age and sex. A total of 2,921 participants with anthropometric data were assessed in the presented models. Demographics for the initial sample (n = 2,947) are located in Table 1. Characteristics of individuals in commonly considered BMI groups as per WHO anthropometry-based criteria [normal weight (NW), BMI ≤ 24.9 kg/m^2; overweight (OW), BMI: 25.0–29.9 kg/m^2; and the obese groups (OB), BMI ≥ 30.0 kg/m^2] [4] are in Table 1. As this is a secondary analysis of the NHANES 2005–2006 data set (a de-identified data set), this project was considered exempt from review by the Institutional Review Board (IRB) at the University of Houston [20]. All NHANES participants provided written informed consent and/or assent in the original study.

Procedure

In the NHANES study, body mass (kg) and height (m) were measured for each participant. BMI was calculated as kg/m^2 as per WHO guidelines [4]. Total and region-specific body composition of each participant was measured via Hologic DXA (Hologic QDR-4500A, Hologic, Inc., Bedford, MA, United States). DXA measures of interest for this study included % of total body fat and head region composition (including head fat %).

Statistical analyses

Multiple regression analyses were performed via SPSS 25 (IBM Corporation, Armonk, NY, United States). All follow-up correlation analyses were performed via Minitab 17 (Minitab LLC, State College, PA, United States) to assess the strength of relationships among individual variables of interest. Consistent with our prior work, linear, quadratic, and logarithmic best fit regression models were assessed for measures of interest. In all models, age, BMI, total body fat %, and head fat % were considered continuous variables. *Sex* (two levels: coded as male = 0 and female = 1) was considered as a categorical variable. Anthropomorphic and DXA data were considered in imputation batches as recommended by the US Centers for Disease Prevention and Control (CDC) [21]. The data from the five NHANES imputation batches converged to the models presented in the results section. The model produced by imputation #1 is presented in this manuscript. After diagnosis using Cook's D, no outliers were removed from the imputation #1 data set.

Results

Means, standard deviations, and range values of age, body mass, height, BMI, total body fat %, and head fat % for all NHANES 2005–2006 study participants aged 8–19 years old

TABLE 2 Regression analyses output.

Factor	Coefficient	t-value	*p*-value
Log(BMI) and total body fat regression model (r = 0.8476, adjusted r^2 = 71.84%)			
Age (years)	−1.0262	−35.01	<0.001
$\log_{10}$(BMI) [$\log_{10}(kg/m^2)$]	62.8960	70.07	<0.001
Sex	7.7910	44.13	<0.001
Regression constant	−44.7900	−40.56	<0.001
Total body fat and head fat linear regression model (r = 0.6939, adjusted r^2 = 48.16%)			
Age (years)	−0.0544	−22.73	<0.001
Total body fat (%)	0.0456	44.79	<0.001
Sex	−0.4571	−25.27	<0.001
Regression constant	23.5743	522.98	<0.001
Total body fat and head fat quadratic regression model (r = 0.7269, adjusted r^2 = 52.84%)			
Age (years)	−0.0609	−26.34	<0.001
Total body fat (%)	−0.0492	−8.66	<0.001
[Total body fat (%)]^2	0.0015	16.94	<0.001
Sex	−0.4026	−22.93	<0.001
Regression constant	24.9762	267.81	<0.001
BMI and head fat regression model (r = 0.7056, adjusted r^2 = 49.78%)			
Age (years)	−0.1069	−41.99	<0.001
BMI (kg/m^2)	0.0624	46.46	<0.001
Sex	−0.1125	−7.22	<0.001
Regression constant	24.0467	622.37	<0.001

are located in Table 1. Significant relationships among adiposity measures of interest (total body fat %, head fat %, and BMI) were found via regression (see Table 2). Age and sex significantly impacted all adiposity relationships. A logarithmic relationship between BMI and total body fat % was found. Linear relationships between head fat % and measures of full body adiposity (BMI and total body fat %) were noted. A quadratic model between head fat % and total body fat is also reported here; the quadratic model provided a modest improvement in R^2 value as compared to the linear model.

The correlation between $\log_{10}$(BMI) and total body fat % was found to be strong (r = 0.626), concurrent with moderate linear positive correlations between head fat % and general adiposity (r = 0.432 for head fat % vs. BMI; and r = 0.522 for head fat % vs. total body fat %). Figures 1A–E illustrates scatterplots of relationships among total body fat %, heat fat %, and BMI. Total body fat % strongly increased with BMI (an increase of 53.43% of total body fat was found across the sample groups); however, the increase in head fat % with BMI was much smaller, at only 3.16% across the sample groups. Differences in adiposity measures across WHO BMI categories are found in Figure 2. The Eqs. 1–4 describing the significant relationships among adiposity measures of interest found in Table 2 are below:

With respect to the relationship between BMI and total body fat, the logarithmic equation describing their relationship is:

$$Total\ Fat\ (\%) = -44.79 - 1.0262^{*}Age\,(years) + 62.896^{*}\log_{10}\left(BMI\,(kg/m^2)\right) + 7.791^{*}Sex \quad (1)$$

where age is in years, BMI is in kg/m^2, total body fat is in %, and sex is coded as male = 0 and female = 1.

With respect to the relationship between total body fat % and subcutaneous head fat %, the equation describing their linear relationship is:

$$Head\ Fat\ (\%) = 23.5743 - 0.0544^{*}Age\,(years) + 0.0456^{*}Total\ Fat\ (\%) - 0.4571^{*}Sex \quad (2)$$

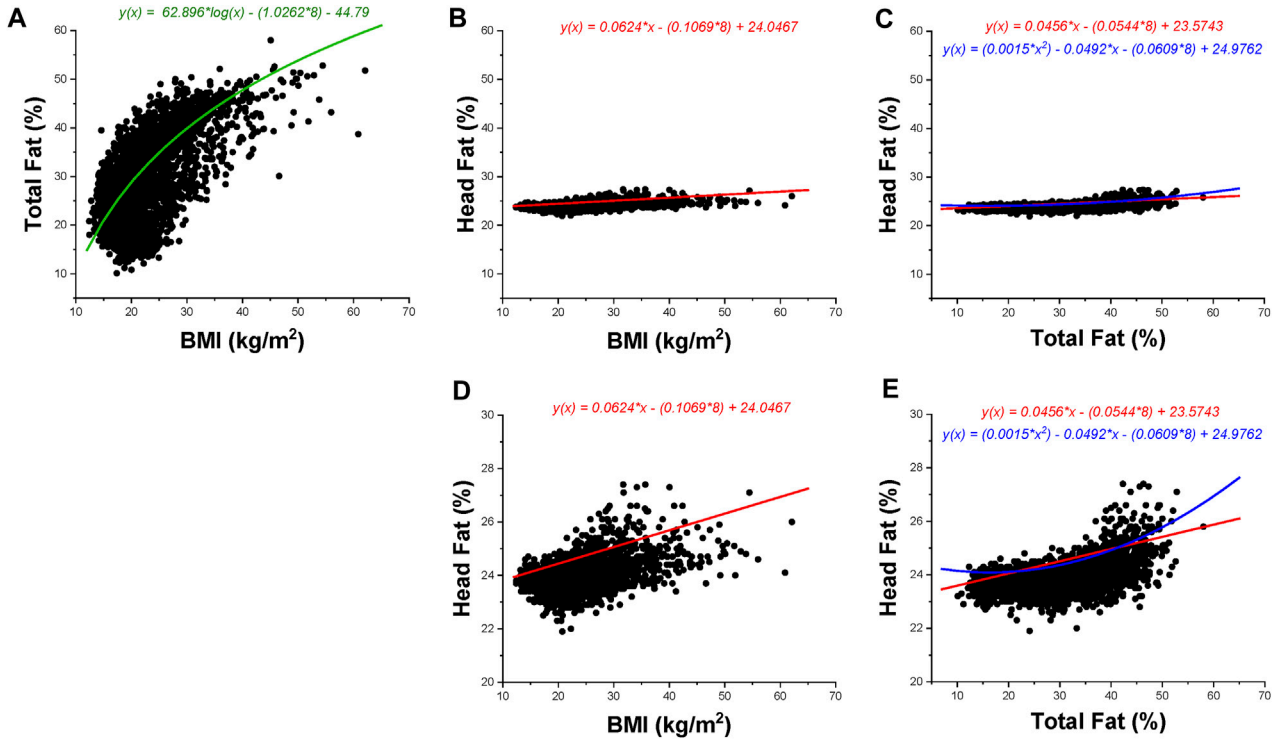

FIGURE 1
BMI, total body fat percentage, and head fat percentage data are presented for children aged 8–19 years. Black dots represent data points; the color-coded lines and corresponding color-coded equations are regression fits as per Table 2. Green indicates a logarithmic regression fit, red indicates a linear regression fit, and blue indicates a quadratic regression fit. All presented regression fits include age = 8 years (minimum age included in the data set) in the equation. The regression fit in **(A)** includes the sex indicator variable (1 = female). **(A–C)** Utilize the same axes values to show magnitude changes across the same scale; **(D–E)** illustrate data at a magnified scale. **(A)**: Total body fat percentage vs. BMI. **(B)**: Head fat percentage versus BMI (full scale). **(C)**: Head fat percentage versus total body fat percentage (full scale). **(D)**: Head fat percentage versus BMI (magnified scale). **(E)**: Head fat percentage versus total body fat percentage (magnified scale).

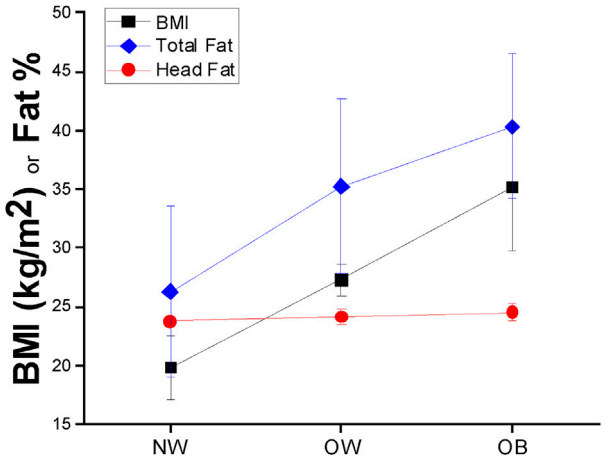

FIGURE 2
BMI (black squares), total body fat percentage (blue diamonds), and head fat percentage (red circles) mean ± SD values across BMI groups in children aged 8–19 years.

where age is in years, total body fat is in %, subcutaneous head fat is in %, and sex is coded as male = 0 and female = 1.

With respect to the relationship between total body fat % and subcutaneous head fat %, the equation describing their quadratic relationship is:

$$\begin{aligned} Head\ Fat\ (\%) = & 24.9762 - 0.0609^{*} Age\,(years) \\ & - 0.0492^{*}\ Total\ Fat\ (\%) \\ & + 0.0015^{*}\,(Total\ Fat\ (\%)^{2}) - 0.4026^{*}\ Sex \end{aligned} \quad (3)$$

where age is in years, total body fat is in %, subcutaneous head fat is in %, and sex is coded as male = 0 and female = 1.

With respect to the relationship between BMI and subcutaneous head fat %, the linear equation describing their relationship is:

$$\begin{aligned} Head\ Fat\ (\%) = & 24.0467 - 0.1069^{*} Age\,(years) \\ & + 0.0624^{*} BMI\ (kg/m^{2}) - 0.1125^{*}\ Sex \end{aligned} \quad (4)$$

where age is in years, BMI is in kg/m^2, subcutaneous head fat is in %, and sex is coded as male = 0 and female = 1.

Discussion

The purpose of this manuscript was to investigate how the percentage of subcutaneous adipose tissue in the head region in children and young adults aged 8–19 years is influenced by commonly used adiposity metrics (e.g., BMI). Consistent with our prior work in adults and older adults, we hypothesized that percentage of subcutaneous adipose tissue in the head region would increase with respect to both total body fat percentage and BMI yet still carry influences of both age and sex (Hypothesis 1). Also in line with our prior findings [9], we expected total body fat to increase proportionally with BMI but that head fat percentage would increase modestly with BMI across the sample (Hypothesis 2).

With respect to Hypothesis 1, a significant increase in subcutaneous head fat percentage was found concurrent with increased BMI ($r = 0.432$) and total body fat percentage ($r = 0.522$). These correlation values were lower than similar comparisons in adults and older adults ($r = 0.668$ and $r = 0.62$, respectively) [9]. Relationships among measures of interest were also influenced by age and sex. In particular, age was found to have a stronger influence on the current data set (children and young adults aged 8–19 years, $|t\text{-values}| \geq 22.73$) as compared to adults ($|t\text{-values}| \geq 4.50$) [9]. In contrast, the magnitude of the influence of sex differences appears lower in children and young adults aged 8–19 years (|t-value| range = 7.22–44.13) as compared to adults (|t-value| range = 14.55–92.84) [9]. The relationship between total body fat percentage and head fat percentage was found to be strongest using a quadratic model, which offered a modest improvement in accounting for model variability (+4.68% as compared to the linear model), whereas adult and older adult data exhibited linear trends [9]. This indicates that head fat percentage appears to become linearly related to total body fat percentage as individuals move into adulthood.

In consideration of Hypothesis 2, head fat percentage exhibited a small increase with BMI as compared to total body fat percentage (3.16% versus 53.43%, respectively). This small increase is similar to our findings in adult models (7.8% and 56.5%, respectively) [9] and findings reported from MRI work [22]. Based on these findings, it is probable that an increased amount of subcutaneous adipose tissue within the head region interferes with neuroimaging tools that measure physiological signals through the derma—confirming concerns that have emerged in the evidence base [9–16]. These tools are particularly susceptible to subcutaneous adipose tissue given the increased electrical resistance of adipose tissue [23] as well as inconsistencies in light propagation across adipose tissue [24]. Consideration of subcutaneous fat as a confounder is important given emerging evidence altered cortical function in persons with obesity (e.g., impaired motor cortex plasticity), which may have life-long impacts [25]. The data in this manuscript indicate that age, sex, and adiposity measures should be considered in the development of model corrections for neuroimaging across the lifespan. Despite similarities in the regression factors in the models generated for children and adults, there are differences in the strengths of relationships within the developed models (e.g., magnitude of regression coefficients, t-values, etc.). Use of age-range specific models is highly encouraged (models developed for ages 8–19 years for children and young adults versus models developed for ages 20–89 years for adults and older adults). We acknowledge at this time that models are not yet developed for children aged 7 years and younger—this is a future direction of our work.

Given the similarity of r^2 values across the models developed from this data set, use of either BMI or total body fat percentage in model corrections with respect to head fat percentage as a source of noise in neuroimaging is recommended for children aged 8–19 years. As BMI only requires basic anthropometric data such as height and mass, it is likely that BMI will be easier for the vast majority of investigators to use for model corrections. Use of total body fat in model corrections is encouraged for investigators who have access to DXA technology for more comprehensive physiological characterization in their model corrections. By accounting for the influence of subcutaneous adipose tissue of the head in neuroimaging studies, a more inclusive approach to neuroscience is permitted at the participant level. Current practices include discarding data with poor signal to noise ratios—an issue that may be caused by increased subcutaneous adipose tissue under the derma of the head. The equations developed in this manuscript may be used to counter this phenotypic bias across the lifespan, which may have a significant impact on reported outcomes in pediatric populations and life-long treatments plans for pediatric patients [17].

We acknowledge that signal to noise corrections with respect to subcutaneous head fat should be explored for individual measurement types (e.g., EEG, fNIRS, and tDCS) and manufacturers for the 8–19 years age range. The development of equations for specific equipment and manufacturers are outside of the scope of this project. The data in this project serve to provide justification in support of recent reports in the evidence base [11–16] for the practice of developing signal to noise correction algorithms due to adiposity measures, sex, and age.

Author contributions

SG and LP participated in the study conceptualization and design; SG drafted the initial version of the manuscript; and HM, SY, and LP contributed to revision of the drafted manuscript. All

authors contributed to the article and approved the submitted version.

Data availability statement

Publicly available datasets were analyzed in this study. This data can be found here: https://www.cdc.gov/nchs/nhanes/index.htm.

Ethics statement

Ethical approval was not required for the study involving humans in accordance with the local legislation and institutional requirements. Written informed consent to participate in this study was not required from the participants or the participants' legal guardians/next of kin in accordance with the national legislation and the institutional requirements.

Funding

Funding support for this project was received from the American Heart Association via #16BGIA27250047 to SG and 1R56AG080816-01 to SG.

Conflict of interest

The authors declare that the research was conducted in the absence of any commercial or financial relationships that could be construed as a potential conflict of interest.

References

1. WHO. *Controlling the global obesity epidemic* (2024). Available from: https://www.who.int/activities/controlling-the-global-obesity-epidemic (Accessed December 6, 2023).

2. WHO. *World obesity day 2022 – accelerating action to stop obesity* (2022). Available from: https://www.who.int/news/item/04-03-2022-world-obesity-day-2022-accelerating-action-to-stop-obesity (Accessed June 13, 2023).

3. CDC. *Childhood obesity facts | overweight and obesity* (2022). Available from: https://www.cdc.gov/obesity/data/childhood.html (Accessed June 13, 2023).

4. WHO. *Obesity and overweight* (2021). Available from: https://www.who.int/news-room/fact-sheets/detail/obesity-and-overweight (Accessed January 14, 2022).

5. Meeuwsen S, Horgan GW, Elia M. The relationship between BMI and percent body fat, measured by bioelectrical impedance, in a large adult sample is curvilinear and influenced by age and sex. *Clin Nutr* (2010) **29**:560–6. doi:10.1016/j.clnu.2009.12.011

6. Rusek W, Baran J, Leszczak J, Adamczyk M, Baran R, Weres A, et al. Changes in children's body composition and posture during puberty growth. *Children (Basel)* (2021) **8**:288. doi:10.3390/children8040288

7. CDC. *All about adult BMI*. Atlanta, GA, United States: Centers for Disease Control and Prevention (2021). Available from: https://www.cdc.gov/healthyweight/assessing/bmi/adult_bmi/index.html (Accessed January 14, 2022).

8. Kanellopoulou A, Antonogeorgos G, Douros K, Panagiotakos DB. The association between obesity and depression among children and the role of family: a systematic review. *Children (Basel)* (2022) **9**:1244. doi:10.3390/children9081244

9. Gorniak SL, Meng H, Pollonini L. Correlation between subcutaneous adipose tissue of the head and body mass index: implications for functional neuroimaging. *Hum Move Sci* (2022) **85**:102997. doi:10.1016/j.humov.2022.102997

10. Mustafa FH, Jones PW, McEwan AL. Near infrared spectroscopy for body fat sensing in neonates: quantitative analysis by GAMOS simulations. *Biomed Eng Online* (2017) **16**:14. doi:10.1186/s12938-016-0310-y

11. Biasiucci A, Franceschiello B, Murray MM. Electroencephalography. *Curr Biol* (2019) **29**:R80–R85. doi:10.1016/j.cub.2018.11.052

12. Usakli AB. Improvement of EEG signal acquisition: an electrical aspect for state of the art of front end. *Comput Intelligence Neurosci* (2010) **2010**:1–7. doi:10.1155/2010/630649

13. Sun H, Li C, Zhang H. Design of virtual BCI channels based on informer. *Front Hum Neurosci* (2023) **17**:1150316. doi:10.3389/fnhum.2023.1150316

14. Horvath J, Carter O, Forte J. Transcranial direct current stimulation: five important issues we aren't discussing (but probably should be). *Front Syst Neurosci* (2014) **8**:2. doi:10.3389/fnsys.2014.00002

15. Reinhart RMG, Cosman JD, Fukuda K, Woodman GF. Using transcranial direct-current stimulation (tDCS) to understand cognitive processing. *Atten Percept Psychophys* (2017) **79**:3–23. doi:10.3758/s13414-016-1224-2

16. Nguyen H-D, Yoo S-H, Bhutta MR, Hong K-S. Adaptive filtering of physiological noises in fNIRS data. *BioMedical Eng Online* (2018) **17**:180. doi:10.1186/s12938-018-0613-2

17. Webb EK, Etter JA, Kwasa JA. Addressing racial and phenotypic bias in human neuroscience methods. *Nat Neurosci* (2022) **25**:410–4. doi:10.1038/s41593-022-01046-0

18. Boutajangout A, Li YS, Quartermain D, Sigurdsson EM. Cognitive and sensorimotor tasks for assessing functional impairments in mouse models of alzheimer's disease and related disorders. *Methods Mol Biol* (2012) **849**:529–40. doi:10.1007/978-1-61779-551-0_35

19. CDC. *NHANES 2005-2006 overview* (2023). Available from: https://wwwn.cdc.gov/nchs/nhanes/continuousnhanes/overview.aspx?BeginYear=2005 (Accessed December 6, 2023).

20. University of Houston. *Exempt review categories* (2024). Available from: https://www.uh.edu/research/compliance/irb/exempt-categories/index (Accessed April 6, 2023).

21. CDC. *NHANES 1999-2006 DXA multiple imputation data files* (2016). Available from: https://wwwn.cdc.gov/nchs/nhanes/dxa/dxa.aspx (Accessed August 17, 2022).

22. Truong DQ, Magerowski G, Blackburn GL, Bikson M, Alonso-Alonso M. Computational modeling of transcranial direct current stimulation (tDCS) in obesity: impact of head fat and dose guidelines. *NeuroImage: Clin* (2013) **2**:759–66. doi:10.1016/j.nicl.2013.05.011

23. Baumgartner RN, Ross R, Heymsfield SB. Does adipose tissue influence bioelectric impedance in obese men and women? *J Appl Physiol* (1998) **84**:257–62. doi:10.1152/jappl.1998.84.1.257

24. Yanina IY, Dyachenko PA, Abdurashitov AS, Shalin AS, Minin IV, Minin OV, et al. Light distribution in fat cell layers at physiological temperatures. *Sci Rep* (2023) **13**:1073. doi:10.1038/s41598-022-25012-9

25. Sui SX, Ridding MC, Hordacre B. Obesity is associated with reduced plasticity of the human motor cortex. *Brain Sci* (2020) **10**:579. doi:10.3390/brainsci10090579

EBM Experimental Biology and Medicine

TYPE Original Research
PUBLISHED 31 January 2024
DOI 10.3389/ebm.2024.10024

OPEN ACCESS

*CORRESPONDENCE
Xincheng Yao,
xcy@uic.edu

RECEIVED 05 October 2023
ACCEPTED 04 January 2024
PUBLISHED 31 January 2024

CITATION
Ding J, Kim T-H, Ma G and Yao X (2024), Intrinsic signal optoretinography of dark adaptation abnormality due to rod photoreceptor degeneration. *Exp. Biol. Med.* 249:10024. doi: 10.3389/ebm.2024.10024

Intrinsic signal optoretinography of dark adaptation abnormality due to rod photoreceptor degeneration

Jie Ding[1], Tae-Hoon Kim[1], Guangying Ma[1] and Xincheng Yao[1,2]*

[1]Department of Biomedical Engineering, University of Illinois Chicago, Chicago, IL, United States, [2]Department of Ophthalmology and Visual Sciences, University of Illinois Chicago, Chicago, IL, United States

Abstract

This research aims to investigate the potential of using intrinsic optical signal (IOS) optoretinography (ORG) to objectively detect dark adaptation (DA) abnormalities related to rod photoreceptor degeneration. Functional optical coherence tomography (OCT) was employed in both wild-type (WT) and retinal degeneration 10 (rd10) mice to conduct this assessment. Dynamic OCT measurements captured the changes in retinal thickness and reflectance from light-to-dark transition. Comparative analysis revealed significant IOS alterations within the outer retina. Specifically, a reduction in thickness from external limiting membrane (ELM) peak to retinal pigment epithelium (RPE) peak was observed (WT: 1.13 $\pm$ 0.69 μm, 30 min DA; rd10: 2.64 $\pm$ 0.86 μm, 30 min DA), as well as a decrease in the intensity of the inner segment ellipsoid zone (EZ) in 30 min DA compared to light adaptation (LA). The reduction of relative EZ intensity was notable in rd10 after 5 min DA and in WT after 15 min DA, with a distinguishable difference between rd10 and WT after 10 min DA. Furthermore, our findings indicated a significant decrease in the relative intensity of the hyporeflective band between EZ and RPE in rd10 retinas during DA, which primarily corresponds to the outer segment (OS) region. In conclusion, the observed DA-IOS abnormalities, including changes in ELM-RPE thickness, EZ, and OS intensity, hold promise as differentiators between WT and rd10 mice before noticeable morphological abnormalities occur. These findings suggest the potential of this non-invasive imaging technique for the early detection of dysfunction in retinal photoreceptors.

KEYWORDS

rd10, rod degeneration, OCT, dark adaptation, IOS

Impact statement

Various eye diseases can lead to photoreceptor dysfunction, with rod photoreceptors being particularly susceptible. Therefore, it is crucial to assess rod photoreceptor function early for detecting eye diseases. This study showcases the potential of using intrinsic signal optoretinography to objectively detect dark adaptation abnormalities associated with rod photoreceptor degeneration.

Introduction

Ocular conditions like age-related macular degeneration (AMD) [1–3], retinitis pigmentosa (RP) [4, 5], and diabetic retinopathy (DR) [6, 7], can result in photoreceptor dysfunctions and eventually vision loss. Numerous eye diseases primarily affect retinal photoreceptors. Presently, there is no definitive cure for these degenerative retinal diseases, which cause permanent damage to photoreceptors and the retinal pigment epithelium (RPE). To prevent vision loss from retinal degeneration, preserving function and identifying progression early are crucial. Therefore, detecting potential biomarkers promptly is essential in prevention of these retinal diseases [8, 9].

Although structural changes like drusen and macular pigmentary abnormalities are valuable for evaluating eye conditions in AMD patients, they do not offer a comprehensive assessment of retinal function [10]. Physiological abnormalities in retinal cells can manifest before any noticeable morphological changes, such as cell loss or thickness alterations. Hence, it is crucial to evaluate the physiological conditions of the retina for the early detection of eye diseases.

Electrophysiological methods like electroretinography (ERG) objectively assess retinal physiology [11, 12]. It is known that ERG a-wave reflects stimulus-evoked physiological activation of photoreceptors, and b-wave reflects the physiological dynamics of neurons. ERG abnormalities were reported in eye diseases [13] and neurodegenerative conditions [14, 15] at an early stage. However, it can be complicated to accurately interpret ERG alterations in diseased conditions since its signal represents combined activities of retinal photoreceptors and inner neurons. It's reported that a-wave abnormality may be attributable to a contamination of post-photoreceptor abnormality in retinal dysfunction [16]. Moreover, the spatial resolution of ERG is relatively low, and thus it is difficult to correlate physiological changes to morphological abnormalities revealed in high resolution imaging.

Intrinsic optical signal (IOS) imaging [17–22], also known as optophysiology [23], optoretinogram [24–28] or optoretinography (ORG) [29–33] allows for simultaneous assessment of retinal morphology and physiology. Optical coherence tomography (OCT) provides non-invasive depth-resolved imaging of retinal layers, making OCT-based intrinsic signal ORG a promising approach for studying human and animal retinas [27–31].

Functional OCT has been utilized to monitor photoreceptor-IOS changes in retinal degeneration 10 (rd10) mice over time [32]. Rd10 mice are a recognized model of rod photoreceptor degeneration [34–38] due to a spontaneous mutation in the genes encoding β-subunit of rod-phosphodiesterase (PDE), resulting in cGMP accumulation and subsequent rod degeneration [37–42]. Since the rods can express approximately 40% of endogenous PDE [41, 43], this degeneration in rd10 mice occurs relatively slowly, starting around postnatal day 16 (P16) to P17. After P21, the outer retina is massively reduced and unable to distinguish. Photoreceptor-IOS abnormalities were previously detected in rd10 mice at P17 by using functional OCT [32]. With a rapid time course to follow visible light stimulus, fast photoreceptor-IOS invoked by the light stimulation can reflect the early phase of phototransduction reaction chains [44]. Photoreceptor-IOS abnormalities were previously detected in rd10 mice at P17 using functional OCT. Fast photoreceptor-IOS responses were found to be similar in both wild-type (WT) and rd10 mice at P14, suggesting that this response occurs before PDE activation in phototransduction reaction chains [41]. The relative expression levels of rhodopsin and transducin in rd10 mice are comparable to those in WT mice [41, 43, 45], indicating that fast photoreceptor-IOS alone is not enough to evaluate PDE deficiency in rd10 before P15.

Dark adaptation (DA) is a method used to assess functional changes in retinal photoreceptors. During DA, eyes are exposed to dark environment and the retina shifts from cone to rod activities in the absence of light. PDE activation can impact the metabolic function of retinal photoreceptors, and thus may cause DA abnormalities. ERG studies have suggested that DA abnormalities may reflect retinal metabolic issues [40], as an early indicators of rod photoreceptor degeneration [46, 47]. The photoreceptor inner segment ellipsoid zone (EZ) is known to be the metabolic center with abundant mitochondria, and it has been demonstrated as a non-invasive OCT marker that reflects optical index changes of cell substances due to photoreceptor activity [48–50]. Recent research demonstrated the monitoring of DA-IOS kinetics within the outer retina, with a focus on the dynamics of the ellipsoid zone (EZ), in healthy adult mice [51]. This study aims to determine if DA-IOS kinetics in the outer retina, which involves downstream transducin activation and photoreceptor metabolism, can detect PDE deficiency-induced photoreceptor abnormalities at P14.

Materials and methods

Animal preparation

OCT images were collected from retinas of Six C57BL/6J mice and nine B6.CXB1-Pde6brd10/J mice (Jackson Laboratory, Bar Harbor, Maine, United States). Pre-experiment, the mouse eyes underwent light adaptation in a well-lit room for more than 5 h [52]. A mixed solution of 100 mg/kg ketamine and 5 mg/kg xylazine was used for anesthesia by intraperitoneal injection. Following

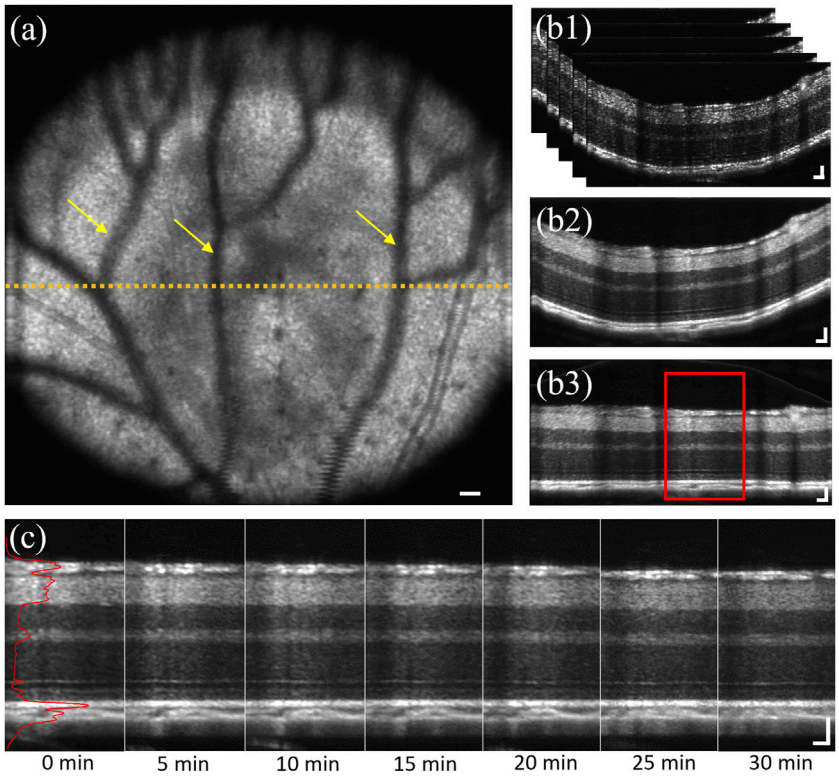

FIGURE 1
(A) Representative en face image of the dorsal quadrant of a mouse retina. Yellow arrows indicate projection shadows of hyaloid vessels. Yellow dashed line represented the selected area, approximately 0.7 mm from optical nerve head. **(B1)** Representative image stack of selected 50 B-scans with 4 repetitions, corresponding to the retinal region marked by yellow dashed line in a. **(B2)** Representative averaged OCT B-scan of b1. **(B3)** Flattened illustration of **(B2)**. **(C)** Representative sequential recording, corresponding to the red window in **(B3)**. Solid red line represents the averaged A-line reflectance profile of the B-scan at 0 min DA. Scale bar: 50 μm.

anesthesia, 0.5% tropicamide was used for eye dilation. GenTeal gel (Alcon Laboratories, Fort Worth, Texas, United States) was applied to mice eyes during the OCT imaging to prevent dryness of the cornea. Post-experiment, mice were kept on a heating pad before recovering from anesthesia and then caged in the animal facility in the Biological Resources Laboratory at the University of Illinois Chicago.

OCT system

A custom-designed OCT system described in a previous paper [51] was used for imaging. Light source was a superluminescent diode (SLD) with a wavelength of 810 nm and a bandwidth of 100 nm (D-810-HP, Superlum, Carrigtwohill, County Cork, Ireland). Light from the SLD was split into the subject and reference arms using a fiber coupler (75:25, TW850R5A2, Thorlabs, Newton, New Jersey, United States). For the spectrometer, a custom-designed setup was assembled, featuring a line CCD camera with 2048 pixels (OCTOPLUS, e2v, Chelmsford, United Kingdom) and a transmission grating with 1200 lines per millimeter (Wasatch Photonics, West Logan, Utah, United States). The sensitivity of the OCT system was assessed using a mirror as the imaging subject, yielding a signal-to-noise ratio of 40 dB. The axial resolution was approximately 2.1 μm and lateral resolution was approximately 11 μm in mouse eye.

Data acquisition

OCT volumes were acquired in a well-lit laboratory room at noon to reduce the impact of circadian rhythm-related disk shedding [52, 53]. The mouse was fully anesthetized and transferred to an adjustable mount. The mouse head was securely fixed by a bite bar and two ear bars to prevent physical movement which may cause the imaging location or focus point change. During OCT imaging, a rodent surgical heating pad was used to keep the body warm.

Mouse retinas were measured at the dorsal quadrant over a 1.4 mm*1.4 mm area (Figure 1A). Each mouse retina was imaged for one experiment that contained 7 sequential OCT volumes for a total

of 30 min recording, with a 5 min interval. The first OCT volume was imaged and adjusted under normal lighting conditions, while the subsequent six OCT volumes were sequentially recorded under dark conditions using identical settings. The focus point and location of the imaging area were optimized before turning off lights. Every OCT volume comprised 500 B-scans with 4 repeated scannings, covering a 1.4 mm × 1.4 mm area. Each B-scan contained 500 A-lines. The fps was 80 B-scans per second. All OCT operations were completed by the same person to reduce errors.

Image processing

Reconstruction of OCT volumes was processed through MATLAB using a custom-designed algorithm including k-sampling, interferogram extraction, apodization, fast Fourier transform (FFT). After OCT reconstruction, 50 consecutive B-scans with 4 repetitions at the retinal cross-section approximately 0.7 mm away from the optical nerve head (ONH) were selected for stack registration (yellow dash line in Figure 1A). The image stack contained 200 B-scans in total (Figure 1B1). Then the stack was registered using the first B-scan as a reference and subsequently aligned the following 199 B-scans to remove stack movement caused by mouse breathing. After that, the image stack was averaged into one B-scan (Figure 1B2) to increase image fidelity and reduce sparkle difference. Then, the A-lines of the B-scan were realigned for image flattening (Figure 1B3), which used the middle one A-line as a reference and all adjacent A-lines were aligned with a subpixel registration algorithm. Next, a central portion of the flattened B-scan, covering 100 to 150 A-lines, was extracted to generate an averaged A-line reflectance profile (Figure 1C). The reason to choose center A-lines instead of the whole B-scan was to avoid the shadow area caused by hyaloid vessels [54] (yellow arrows, Figure 1A) and distortion caused by the retina angle at both edges. Also, large blood vessels were avoided when choosing center A-lines, because the retina was thickened where the large blood vessel walls embedded. Retinal thickness and layer intensity were measured based on the A-line profile normalized using the outer nuclear layer (ONL) intensity as a reference [55–57].

Statistical analysis was performed using Origin's one-way repeated-measures analysis of variance (ANOVA) with Bonferroni correction. A significance level of p-values < 0.05 was used, and standard deviation was represented as the error bar for each data point.

Results

Morphological changes caused by photoreceptor degeneration

Morphological comparison was conducted to investigate the structural changes caused by photoreceptor degeneration.

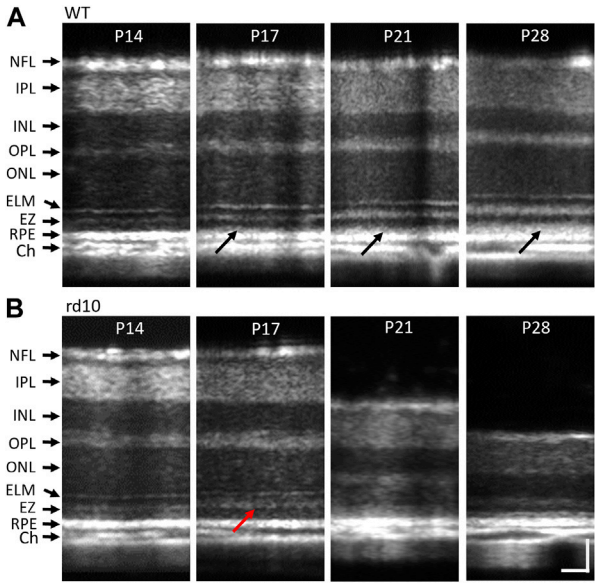

FIGURE 2
Representative morphological OCT images of WT **(A)** and rd10 **(B)** retinas at P14 to P28. The red arrow in figure 2b2 marks the OS region of rd10 started dissembling at P17. NFL, nerve fiber layer; IPL, inner plexiform layer; INL, inner nuclear layer; OPL, outer plexiform layer; ONL, outer nuclear layer; ELM, external limiting membrane; EZ, inner segment ellipsoid; RPE, retinal pigment epithelium; Ch, choroid. Scale bar: 50 μm.

Representative OCT images from WT and rd10 mice at P14, P17, P21, and P28 under light-adapted (LA) conditions were presented in Figure 2. Retinal OCT morphological changes were observed in rd10, compared to WT mice from P17. Specifically, rd10 retinas exhibited unclear external limiting membrane (ELM) and "swollen" EZ structures (red arrow, Figure 2B), with significant reduction in outer retinal thickness at P21 and P28. Also, the interdigitation zone (IZ) could be observed in WT retinas from P17 to P28 (dark arrows, Figure 2A), whilst it's not shown in rd10 retinas. As degeneration signs began around P17, morphologically intact retinas at P14 were chosen for comparative OCT measurements and analysis in the following sections. This stage represents an early phase before significant abnormality appeared.

Functional changes of retinas during light to dark transition

OCT analysis of P14 WT and rd10 retinas under LA and DA conditions were compared in Figure 3. Inner retinal morphology showed no obvious differences in WT (Figure 3A1) and rd10 (Figure 3A2) mice between LA and DA. In both groups, the thickness from ELM peak to RPE peak (highlighted with red arrows, Figure 3A) was reduced during DA compared to LA. Figure 3B showed averaged A-line profiles of retinas form six

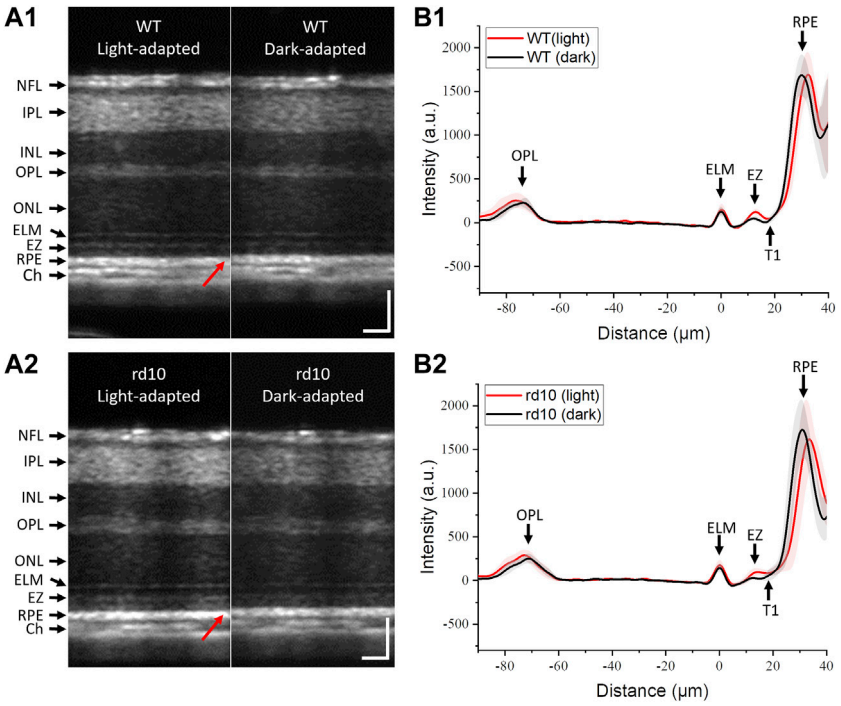

FIGURE 3
Representative OCT images of mouse retinas from WT **(A1)** and rd10 **(A2)** in LA and after 30 min DA; Averaged A-line profiles of OCT images from six WT **(B1)** and nine rd10 mice **(B2)** in LA and after 30 min DA. Standard deviations were represented as shadows adjacent to the lines. NFL: nerve fiber layer; IPL: inner plexiform layer; INL: inner nuclear layer; OPL: outer plexiform layer; ONL: outer nuclear layer; ELM: external limiting membrane; EZ: inner segment ellipsoid; RPE: retinal pigment epithelium; Ch: choroid; T1: trough 1. Scale bar: 50 μm.

WT mice and nine rd10 mice at LA condition and after 30 min of DA to further characterize the observed retinal shrinkage in WT (Figure 3B1) and rd10 (Figure 3B2) retinas. All mouse retinas were measured at P14. Standard deviations were represented as shadows accompanying the lines. For easy comparison, the location of ELM peak was normalized to 0 on the X-axis. In both groups, the RPE peak shifted toward the ELM in DA compared to LA. Additionally, OCT band intensities were altered, with a notable decrease in EZ peak intensity in both WT and rd10 during DA compared to LA. The OPL and ELM peak values also slightly decreased in DA.

A clear hyporeflective band, T1, situated between EZ and RPE, was visible in WT retinas (Figure 3B1). However, T1 was elusive in rd10 retinas after 30 min DA (Figure 3B2). As the T1 primarily corresponds to the photoreceptor outer segment (OS) region due to its location between EZ and RPE, this observation might indicate potential photoreceptor OS abnormalities, suggesting a physiological defect in rd10 photoreceptors.

Comparative analysis of retinal changes during light to dark transition

We proceeded to compare DA-IOS kinetics in WT and rd10 retinas during a 30 min transition from light to dark. Time-lapse OCT images were recorded, including seven sequential OCT volumes from 0 (LA) to 30 min of DA at a 5-min interval.

The thickness changes in inner and outer retina during DA were quantitatively assessed. Figure 4A illustrated inner retina thickness changes in both groups, with no significant alterations observed in the inner retina (NFL-OPL). Conversely, outer retina thickness (OPL-RPE) gradually decreased during DA, aligning with the shrinkage of outer retina observed in DA conditions in Figure 3. Figures 4C, D separately illustrated the ONL (OPL-ELM) and ELM-RPE thickness reduction. The thickness at LA condition (0 min) was set as standard and subtracted by the thicknesses at following time points. Both ONL and ELM-RPE thicknesses consistently decreased during DA. Results were shown in Figures 4C, D, that the ONL thickness change of WT (1.57 ± 0.73 μm, 30 min DA) was similar with rd10 (1.72 ± 0.78 μm, 30 min DA), however the ELM-RPE thickness change of WT (1.13 ± 0.69 μm, 30 min DA) was smaller than the rd10 (2.64 ± 0.86 μm, 30 min DA). Statistical significance was shown in rd10 after 5 min DA but not in WT ($p < 0.001$). Additionally, at time point 15 and 25, the difference was significant between the two groups ($p < 0.01$).

Figure 3B demonstrated a decrease in OCT intensity in the outer retina, particularly the EZ band in both retinas. Figure 5

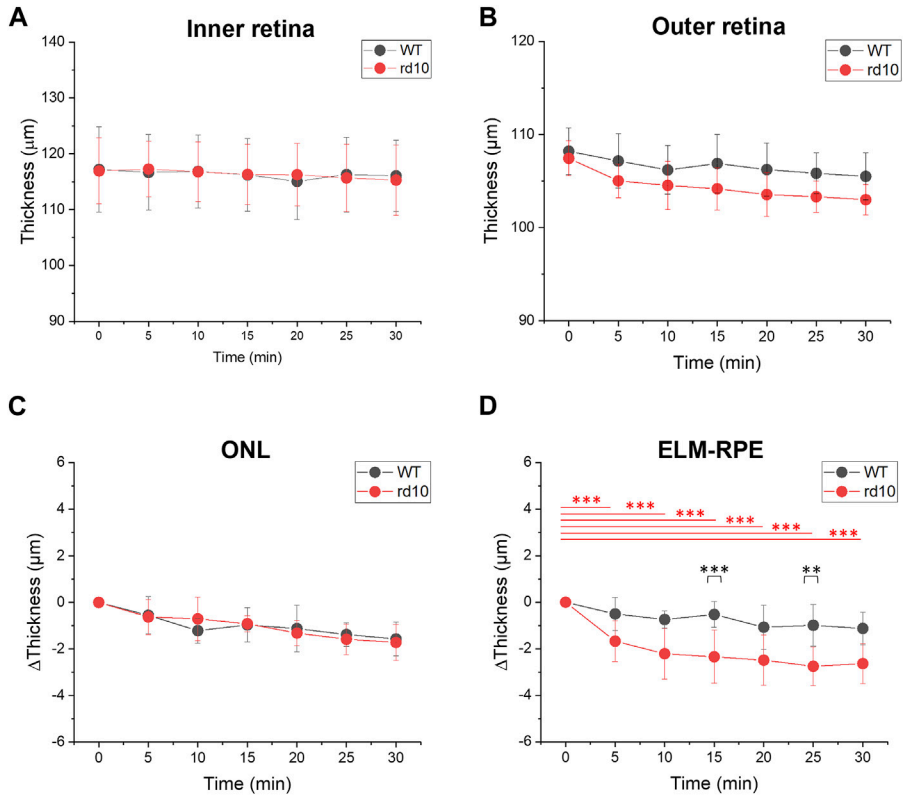

FIGURE 4
Comparative analysis of outer retina thickness changes during light to dark transition. **(A)** Inner retina (NFL-OPL) thickness; **(B)** Outer retina (OPL to RPE) thickness; **(C)** ONL (OPL to ELM) thickness change; **(D)** ELM to RPE thickness change. Standard deviation was represented as the error bar for each data point. $^{**}p < 0.001$, $^{***}p < 0.001$, compared to 0 min within group and at same time point between groups, using one-way ANOVA with the Bonferroni correction. Data was averaged from six WT and nine rd10 retinas.

followed this finding to further compare the relative intensity changes from outer retinal layers. The results indicated similar relative intensity changes in OPL (Figure 5A) and RPE (Figure 5D) bands between WT and rd10. However, significant DA-IOS kinetic differences were observed in EZ and T1 (Figures 5B, C). A significant intensity reduction was observed in EZ after 5 min DA in rd10 retinas ($p < 0.001$), while it occurred after 15 min DA in WT retinas ($p < 0.001$). Also, statistical difference was shown between WT and rd10 after 10 min DA ($p < 0.001$). Regarding the relative intensity reduction of T1, Figure 5C demonstrated the notable decrease in rd10 after 10 min of DA ($p < 0.01$), while in WT, this decrease was observed only after 30 min of DA ($p < 0.05$). Together, these results indicated that during DA the intensity of EZ peak and OS region decreased rapidly in rd10, compared to WT.

Discussion

Functional OCT was conducted to characterize morphological measurements and DA-IOS kinetics at the outer retina in WT and rd10 mice. First, we observed unclear ELM and "swollen" EZ at P17, as well as reduced outer retina at P21 in rd10 OCT images, and the IZ was observed only in WT OCT images after P17. According to these morphological changes, we then studied structural intact retinas at P14 using dark adaptation method, to observe functional morphological changes. Both WT and rd10 retinas displayed a decrease in ELM-RPE thickness and a reduction in EZ intensity during DA, as shown in Figures 4, 5. The observation aligns with prior reports of outer retina shrinkage in dark conditions [51, 52, 58]. However, it's worth noting that the transient thickness change of ELM-RPE in rd10 during DA was larger compared to WT, as indicated in Figure 4D. The EZ and T1 intensity changes were distinguishable quickly in rd10 after 5 min and 10 min DA (Figures 5B, D). These results suggested that DA-IOS kinetics, particularly the ELM-RPE thickness, EZ and OS body intensity, can provide sensitive biomarkers for functional assessment of photoreceptor physiology.

Compared to previous study [51], the DA changes in thickness and intensity were more significant and the OCT reflectance itself was brighter in mature WT retina. A

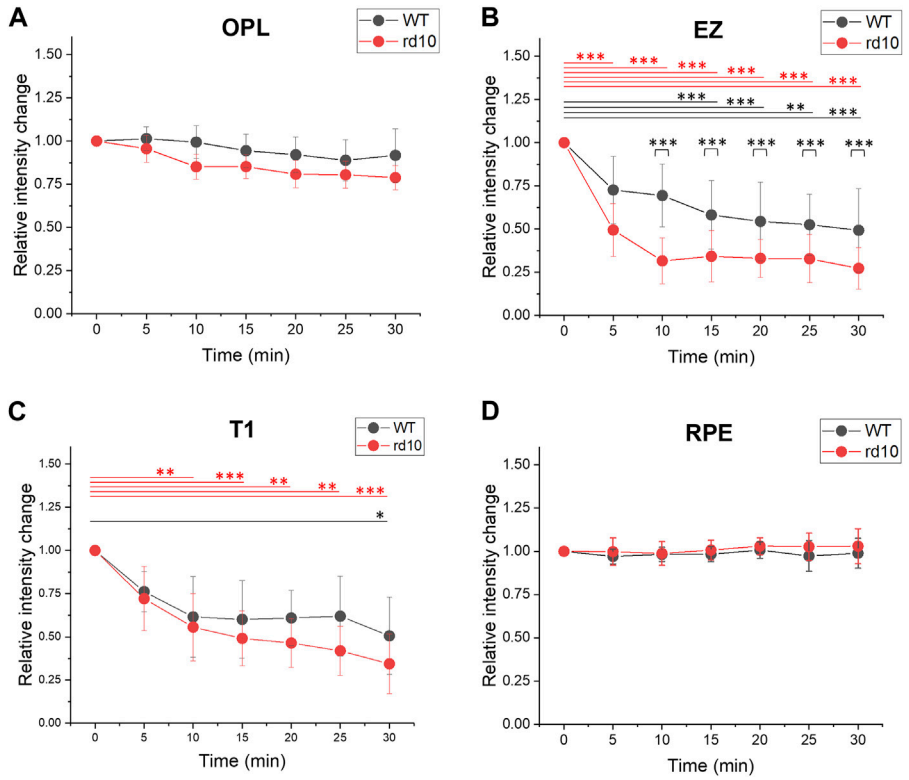

FIGURE 5
Comparative analysis of outer retina relative intensity changes during light to dark transition. **(A)** OPL relative intensity change; **(B)** EZ relative intensity change; **(C)** T1 relative intensity change. **(D)** RPE intensity change. Standard deviation was represented as the error bar for each data point. *$p < 0.05$, **$p < 0.01$, ***$p < 0.001$, compared to 0 min within one group and at same time point between two groups, using one-way ANOVA with the Bonferroni correction. Data was averaged from six WT and nine rd10 retinas.

potential explanation could be that the metabolic condition and response in adult mouse retina are known to become more robust with maturation which was reflected in ERG [59]. In addition, it has been reported that at the structural and molecular level, photoreceptors are fully functional by P30, and protein expressions as well as synapse activity become mature after P30 [60].

We speculated some potential mechanisms behind the DA-IOS changes, specifically the observed shrinkage of ELM-RPE thickness and reduction of EZ intensity from P14 retinas. Many studies reported that enhanced RPE pumping activity [40, 58, 61, 62] and mitochondrial morphological changes during DA [50, 61] may reduce the fluid content, which leads to shrinkage of ELM-RPE thickness and decrease of OCT reflectance. Higher oxidative stress in rod photoreceptors of rd10 [63] could cause oxidative damage to photoreceptors and affect their functions [64]. Increased oxygen supply to the photoreceptor increased the respiratory metabolites including water content produced by mitochondria [65, 66]. After DA, the accumulation of metabolic fluid between ELM-RPE is reduced and leads to thickness shrinkage in the rd10 retina [58]. Thus, we hypothesized that the enhanced water content removal together with mitochondrial activity contributes to accelerated shrinkage of ELM-RPE thickness and reduction of EZ intensity in rd10.

Decrease of internal osmotic pressure in DA resulting in reversed cytoplasmic swelling and less backscattering could be another potential mechanism behind these DA-IOS changes. In the presence of light, rhodopsin absorbs photons and becomes active, then activates transducin and subsequent PDE-mediated cGMP hydrolysis, which turns off ion channels. This process may increase osmotic pressure with extra osmolytes and result in cytoplasmic swelling, causing increased ELM-RPE thickness and EZ intensity [67, 68]. However, in DA without light, rhodopsin is inactivated, and the cascade gradually stops. Without transducin activating PDE, cGMP contributes to ion flux through open ion channels, reducing internal osmotic pressure and promoting cytoplasmic fluid removal, leading to shrinkage of ELM-RPE thickness and reduction of EZ intensity [67]. This process occurs after transducin activation, which was expressed comparably in WT and rd10 retinas at P14 [41]. Therefore, in both groups the thickness shrinkage and intensity reduction were observed. However, rd10 retinas at P14 exhibited accelerated reductions in ELM-RPE thickness and EZ intensity compared to WT,

possibly due to the pre-existing PDE deficiency in rd10 mice present from birth [38, 41, 43, 45], leading to less functional PDE proteins and higher cGMP accumulation in the OS [37]. The increased cGMP concentration may result in faster osmotic pressure reduction with restoration of cytoplasmic fluid removal in DA, contributing to accelerated thickness shrinkage and reduced backscattering in retinal photoreceptors of rd10 mice.

Based on the A-line reflectance profiles, we did not observe a hyperreflective peak (IZ) near RPE in P14 mouse like in adult WT mouse retina [51], but only the hyporeflective band T1 between EZ and RPE. Interestingly, the T1 intensity in rd10 was higher than that in WT in light condition, and it was almost same as the EZ intensity after dark adaptation (Figure 3B). It is known that hyporeflective band T1 between EZ and RPE was most correlated with OS body [32]. The intensity difference in OS may be result from the deficient PDE level in rd10 retina at P14 and need further investigation. Together, the observation of T1 intensity suggested that possible OS abnormality occurred during DA in rd10 retinas at P14.

Conclusion

Comparative OCT revealed DA-IOS markers, such as shrinkage of ELM-RPE thickness and reduction of EZ and T1 relative intensities, to differentiate WT and rd10 retinas at around P14 before notable morphological abnormality. Both WT and rd10 retinas consistently showed ELM-RPE thickness shrinkage together with EZ intensity reduction after DA. The DA caused thickness and intensity responses were observed to be significantly larger and quicker in rd10 compared to WT, providing non-invasive IOS markers for early detection of photoreceptors dysfunction due to degeneration. The hyporeflective band T1, corresponding to photoreceptor OS, also showed obvious intensity difference. The assessment of DA-IOS kinetics through intrinsic signal ORG presents a valuable non-invasive approach to detect early signs of rod photoreceptor degeneration.

Author contributions

JD conducted the experiments, data analysis and manuscript preparation. T-HK and GM contributed to data analysis and manuscript preparation. XY contributed to manuscript preparation and supervised the project. All authors contributed to the article and approved the submitted version.

Data availability statement

The raw data supporting the conclusion of this article will be made available by the authors, without undue reservation.

Ethics statement

The animal study was approved by Animal Care Committee at the University of Illinois Chicago. The study was conducted in accordance with the local legislation and institutional requirements.

Funding

This research received support from National Eye Institute (P30 EY001792, R01 EY023522, R01 EY030101, R01EY029673, R01EY030842); Research to Prevent Blindness; Richard and Loan Hill Endowment.

Conflict of interest

The authors declare that the research was conducted in the absence of any commercial or financial relationships that could be construed as a potential conflict of interest.

References

1. Curcio CA, Medeiros NE, Millican CL. Photoreceptor loss in age-related macular degeneration. *Invest Ophthalmol Vis Sci* (1996) **37**:1236–49.

2. Yang S, Zuo C, Xiao H, Mi L, Luo G, Xu X, et al. Photoreceptor dysfunction in early and intermediate age-related macular degeneration assessed with mfERG and spectral domain OCT. *Doc Ophthalmol* (2016) **132**:17–26. doi:10.1007/s10633-016-9523-4

3. Jackson GR, Owsley C, Curcio CA. Photoreceptor degeneration and dysfunction in aging and age-related maculopathy. *Ageing Res Rev* (2002) **1**: 381–96. doi:10.1016/s1568-1637(02)00007-7

4. Holopigian K, Seiple W, Greenstein VC, Hood DC, Carr RE. Local cone and rod system function in patients with retinitis pigmentosa. *Invest Ophthalmol Vis Sci* (2001) **42**:779–88.

5. Wen Y, Locke KG, Hood DC, Birch DG. Rod photoreceptor temporal properties in retinitis pigmentosa. *Exp Eye Res* (2011) **92**:202–8. doi:10.1016/j.exer.2010.12.014

6. Holopigian K, Greenstein VC, Seiple W, Hood DC, Carr RE. Evidence for photoreceptor changes in patients with diabetic retinopathy. *Invest Ophthalmol Vis Sci* (1997) **38**:2355–65.

7. McAnany JJ, Park JC. Cone photoreceptor dysfunction in early-stage diabetic retinopathy: association between the activation phase of cone phototransduction and the flicker electroretinogram. *Invest Ophthalmol Vis Sci* (2019) **60**:64–72. doi:10.1167/iovs.18-25946

8. Feigl B, Morris CP. The challenge of predicting macular degeneration. *Curr Med Res Opin* (2011) **27**:1745–8. doi:10.1185/03007995.2011.603301

9. Zhang Y, Wang Y, Shi C, Shen M, Lu F. Advances in retina imaging as potential biomarkers for early diagnosis of Alzheimer's disease. *Transl Neurodegener* (2021) **10**:6. doi:10.1186/s40035-021-00230-9

10. Sunness JS, Massof RW, Johnson MA, Bressler NM, Bressler SB, Fine SL. Diminished foveal sensitivity may predict the development of advanced age-related macular degeneration. *Ophthalmology* (1989) **96**:375–81. doi:10.1016/s0161-6420(89)32883-1

11. Porciatti V. Electrophysiological assessment of retinal ganglion cell function. *Exp Eye Res* (2015) **141**:164–70. doi:10.1016/j.exer.2015.05.008

12. Scholl HP, Zrenner E. Electrophysiology in the investigation of acquired retinal disorders. *Surv Ophthalmol* (2000) **45**:29–47. doi:10.1016/s0039-6257(00)00125-9

13. McAnany JJ, Park JC. Temporal frequency abnormalities in early-stage diabetic retinopathy assessed by electroretinography. *Invest Ophthalmol Vis Sci* (2018) **59**:4871–9. doi:10.1167/iovs.18-25199

14. Ragauskas S, Leinonen H, Puranen J, Ronkko S, Nymark S, Gurevicius K, et al. Early retinal function deficit without prominent morphological changes in the R6/2 mouse model of Huntington's disease. *PLoS One* (2014) **9**:e113317. doi:10.1371/journal.pone.0113317

15. Asanad S, Felix CM, Fantini M, Harrington MG, Sadun AA, Karanjia R. Retinal ganglion cell dysfunction in preclinical Alzheimer's disease: an electrophysiologic biomarker signature. *Sci Rep* (2021) **11**:6344. doi:10.1038/s41598-021-85010-1

16. McAnany JJ, Matei N, Chen YF, Liu K, Park JC, Shahidi M. Rod pathway and cone pathway retinal dysfunction in the 5xFAD mouse model of Alzheimer's disease. *Sci Rep* (2021) **11**:4824. doi:10.1038/s41598-021-84318-2

17. Ts'o D, Schallek J, Kwon Y, Kardon R, Abramoff M, Soliz P. Noninvasive functional imaging of the retina reveals outer retinal and hemodynamic intrinsic optical signal origins. *Jpn J Ophthalmol* (2009) **53**:334–44. doi:10.1007/s10384-009-0687-2

18. Yao X, Wang B. Intrinsic optical signal imaging of retinal physiology: a review. *J Biomed Opt* (2015) **20**:090901. doi:10.1117/1.jbo.20.9.090901

19. Hanazono G, Tsunoda K, Kazato Y, Tsubota K, Tanifuji M. Evaluating neural activity of retinal ganglion cells by flash-evoked intrinsic signal imaging in macaque retina. *Invest Ophthalmol Vis Sci* (2008) **49**:4655–63. doi:10.1167/iovs.08-1936

20. Begum M, Joiner DP, Ts'o DY. Stimulus-driven retinal intrinsic signal optical imaging in mouse demonstrates a dominant rod-driven component. *Invest Ophthalmol Vis Sci* (2020) **61**:37. doi:10.1167/iovs.61.8.37

21. Wang B, Yao X. *In vivo* intrinsic optical signal imaging of mouse retinas. *Proc SPIE Int Soc Opt Eng* (2016) **9693**:96930H. doi:10.1117/12.2212810

22. Zhang Q, Zhang Y, Lu R, Li Y, Pittler SJ, Kraft TW, et al. Comparative intrinsic optical signal imaging of wild-type and mutant mouse retinas. *Opt Express* (2012) **20**:7646–54. doi:10.1364/oe.20.007646

23. Bizheva K, Pflug R, Hermann B, Povazay B, Sattmann H, Qiu P, et al. Optophysiology: depth-resolved probing of retinal physiology with functional ultrahigh-resolution optical coherence tomography. *Proc Natl Acad Sci U S A* (2006) **103**:5066–71. doi:10.1073/pnas.0506997103

24. Azimipour M, Valente D, Vienola KV, Werner JS, Zawadzki RJ, Jonnal RS. Optoretinogram: optical measurement of human cone and rod photoreceptor responses to light. *Opt Lett* (2020) **45**:4658–61. doi:10.1364/ol.398868

25. Pandiyan VP, Maloney-Bertelli A, Kuchenbecker JA, Boyle KC, Ling T, Chen ZC, et al. The optoretinogram reveals the primary steps of phototransduction in the living human eye. *Sci Adv* (2020) **6**:eabc1124. doi:10.1126/sciadv.abc1124

26. Zhang L, Dong R, Zawadzki RJ, Zhang P. Volumetric data analysis enabled spatially resolved optoretinogram to measure the functional signals in the living retina. *J Biophotonics* (2022) **15**:e202100252. doi:10.1002/jbio.202100252

27. Jonnal RS. Toward a clinical optoretinogram: a review of noninvasive, optical tests of retinal neural function. *Ann Transl Med* (2021) **9**:1270. doi:10.21037/atm-20-6440

28. Zhang P, Shibata B, Peinado G, Zawadzki RJ, FitzGerald P, Pugh EN, Jr. Measurement of diurnal variation in rod outer segment length *in vivo* in mice with the OCT optoretinogram. *Invest Ophthalmol Vis Sci* (2020) **61**:9. doi:10.1167/iovs.61.3.9

29. Lassoued A, Zhang F, Kurokawa K, Liu Y, Bernucci MT, Crowell JA, et al. Cone photoreceptor dysfunction in retinitis pigmentosa revealed by optoretinography. *Proc Natl Acad Sci U S A* (2021) **118**:e2107444118. doi:10.1073/pnas.2107444118

30. Ma G, Son T, Kim TH, Yao X. Functional optoretinography: concurrent OCT monitoring of intrinsic signal amplitude and phase dynamics in human photoreceptors. *Biomed Opt Express* (2021) **12**:2661–9. doi:10.1364/boe.423733

31. Cooper RF, Brainard DH, Morgan JIW. Optoretinography of individual human cone photoreceptors. *Opt Express* (2020) **28**:39326–39. doi:10.1364/oe.409193

32. Kim TH, Wang B, Lu Y, Son T, Yao X. Functional optical coherence tomography enables *in vivo* optoretinography of photoreceptor dysfunction due to retinal degeneration. *Biomed Opt Express* (2020) **11**:5306–20. doi:10.1364/boe.399334

33. Pandiyan VP, Jiang X, Maloney-Bertelli A, Kuchenbecker JA, Sharma U, Sabesan R. High-speed adaptive optics line-scan OCT for cellular-resolution optoretinography. *Biomed Opt Express* (2020) **11**:5274–96. doi:10.1364/boe.399034

34. Berkowitz BA, Podolsky RH, Childers KL, Roche SL, Cotter TG, Graffice E, et al. Rod photoreceptor neuroprotection in dark-reared Pde6brd10 mice. *Invest Ophthalmol Vis Sci* (2020) **61**:14. doi:10.1167/iovs.61.13.14

35. Deng WT, Kolandaivelu S, Dinculescu A, Li J, Zhu P, Chiodo VA, et al. Cone phosphodiesterase-6γ' subunit augments cone PDE6 holoenzyme assembly and stability in a mouse model lacking both rod and cone PDE6 catalytic subunits. *Front Mol Neurosci* (2018) **11**:233. doi:10.3389/fnmol.2018.00233

36. Rosch S, Johnen S, Muller F, Pfarrer C, Walter P. Correlations between ERG, OCT, and anatomical findings in the rd10 mouse. *J Ophthalmol* (2014) **2014**:874751–10. doi:10.1155/2014/874751

37. Wang T, Reingruber J, Woodruff ML, Majumder A, Camarena A, Artemyev NO, et al. The PDE6 mutation in the rd10 retinal degeneration mouse model causes protein mislocalization and instability and promotes cell death through increased ion influx. *J Biol Chem* (2018) **293**:15332–46. doi:10.1074/jbc.ra118.004459

38. Pennesi ME, Michaels KV, Magee SS, Maricle A, Davin SP, Garg AK, et al. Long-term characterization of retinal degeneration in rd1 and rd10 mice using spectral domain optical coherence tomography. *Invest Ophthalmol Vis Sci* (2012) **53**:4644–56. doi:10.1167/iovs.12-9611

39. Chang B, Hawes N, Hurd R, Davisson M, Nusinowitz S, Heckenlively J. Retinal degeneration mutants in the mouse. *Vis Res* (2002) **42**:517–25. doi:10.1016/s0042-6989(01)00146-8

40. Gargini C, Terzibasi E, Mazzoni F, Strettoi E. Retinal organization in the retinal degeneration 10 (rd10) mutant mouse: a morphological and ERG study. *J Comp Neurol* (2007) **500**:222–38. doi:10.1002/cne.21144

41. Lu Y, Kim TH, Yao X. Comparative study of wild-type and rd10 mice reveals transient intrinsic optical signal response before phosphodiesterase activation in retinal photoreceptors. *Exp Biol Med (Maywood)* (2020) **245**:360–7. doi:10.1177/1535370219896284

42. Phillips MJ, Otteson DC, Sherry DM. Progression of neuronal and synaptic remodeling in the rd10 mouse model of retinitis pigmentosa. *J Comp Neurol* (2010) **518**:2071–89. doi:10.1002/cne.22322

43. Chang B, Hawes NL, Pardue MT, German AM, Hurd RE, Davisson MT, et al. Two mouse retinal degenerations caused by missense mutations in the β-subunit of rod cGMP phosphodiesterase gene. *Vis Res* (2007) **47**:624–33. doi:10.1016/j.visres.2006.11.020

44. Yao X, Kim TH. Fast intrinsic optical signal correlates with activation phase of phototransduction in retinal photoreceptors. *Exp Biol Med (Maywood)* (2020) **245**:1087–95. doi:10.1177/1535370220935406

45. Samardzija M, Wariwoda H, Imsand C, Huber P, Heynen SR, Gubler A, et al. Activation of survival pathways in the degenerating retina of rd10 mice. *Exp Eye Res* (2012) **99**:17–26. doi:10.1016/j.exer.2012.04.004

46. Owsley C, McGwin G, Jr, Clark ME, Jackson GR, Callahan MA, Kline LB, et al. Delayed rod-mediated dark adaptation is a functional biomarker for incident early age-related macular degeneration. *Ophthalmology* (2016) **123**:344–51. doi:10.1016/j.ophtha.2015.09.041

47. Hsiao CC, Hsu HM, Yang CM, Yang CH. Correlation of retinal vascular perfusion density with dark adaptation in diabetic retinopathy. *Graefes Arch Clin Exp Ophthalmol* (2019) **257**:1401–10. doi:10.1007/s00417-019-04321-2

48. Litts KM, Zhang Y, Freund KB, Curcio CA. Optical coherence tomography and histology of age-related macular degeneration support mitochondria as reflectivity sources. *Retina* (2018) **38**:445–61. doi:10.1097/iae.0000000000001946

49. Berkowitz BA, Podolsky RH, Childers KL, Burgoyne T, De Rossi G, Qian H, et al. Functional changes within the rod inner segment ellipsoid in wildtype mice: an optical coherence tomography and electron microscopy study. *Invest Ophthalmol Vis Sci* (2022) **63**:8. doi:10.1167/iovs.63.8.8

50. Ma G, Son T, Kim TH, Yao X. *In vivo* optoretinography of phototransduction activation and energy metabolism in retinal photoreceptors. *J Biophotonics* (2021) **14**:e202000462. doi:10.1002/jbio.202000462

51. Kim TH, Ding J, Yao X. Intrinsic signal optoretinography of dark adaptation kinetics. *Sci Rep* (2022) **12**:2475. doi:10.1038/s41598-022-06562-4

52. Li Y, Fariss RN, Qian JW, Cohen ED, Qian H. Light-induced thickening of photoreceptor outer segment layer detected by ultra-high resolution OCT imaging. *Invest Ophthalmol Vis Sci* (2016) **57**:OCT105–11. doi:10.1167/iovs.15-18539

53. Mazzoni F, Safa H, Finnemann SC. Understanding photoreceptor outer segment phagocytosis: use and utility of RPE cells in culture. *Exp Eye Res* (2014) **126**:51–60. doi:10.1016/j.exer.2014.01.010

54. Kim TH, Son T, Yao X. Functional OCT angiography reveals early physiological dysfunction of hyaloid vasculature in developing mouse eye. *Exp Biol Med (Maywood)* (2019) **244**:819–23. doi:10.1177/1535370219850787

55. Chen X, Hou P, Jin C, Zhu W, Luo X, Shi F, et al. Quantitative analysis of retinal layer optical intensities on three-dimensional optical coherence tomography. *Invest Opthalmology Vis Sci* (2013) **54**:6846–51. doi:10.1167/iovs.13-12062

56. Risseeuw S, Bennink E, Poirot MG, de Jong PA, Spiering W, Imhof SM, et al. A reflectivity measure to quantify Bruch's membrane calcification in patients with pseudoxanthoma elasticum using optical coherence tomography. *Translational Vis Sci Tech* (2020) **9**:34. doi:10.1167/tvst.9.8.34

57. Meleppat RK, Zhang P, Ju MJ, Manna SK, Jian Y, Pugh EN, et al. Directional optical coherence tomography reveals melanin concentration-dependent scattering properties of retinal pigment epithelium. *J Biomed Opt* (2019) **24**:1–10. doi:10.1117/1.jbo.24.6.066011

58. Li Y, Zhang Y, Chen S, Vernon G, Wong WT, Qian H. Light-Dependent OCT structure changes in photoreceptor degenerative rd 10 mouse retina. *Invest Ophthalmol Vis Sci* (2018) **59**:1084–94. doi:10.1167/iovs.17-23011

59. Bonezzi PJ, Stabio ME, Renna JM. The development of mid-wavelength photoresponsivity in the mouse retina. *Curr Eye Res* (2018) **43**:666–73. doi:10.1080/02713683.2018.1433859

60. Volkner M, Kurth T, Schor J, Ebner LJA, Bardtke L, Kavak C, et al. Mouse retinal organoid growth and maintenance in longer-term culture. *Front Cel Dev Biol* (2021) **9**:645704. doi:10.3389/fcell.2021.645704

61. Linton JD, Holzhausen LC, Babai N, Song H, Miyagishima KJ, Stearns GW, et al. Flow of energy in the outer retina in darkness and in light. *Proc Natl Acad Sci U S A* (2010) **107**:8599–604. doi:10.1073/pnas.1002471107

62. Bissig D, Berkowitz BA. Light-dependent changes in outer retinal water diffusion in rats *in vivo*. *Mol Vis* (2012) **18**:2561.

63. Berkowitz BA, Podolsky RH, Lins-Childers KM, Li Y, Qian H. Outer retinal oxidative stress measured *in vivo* using QUEnch-assiSTed (QUEST) OCT. *Invest Ophthalmol Vis Sci* (2019) **60**:1566–70. doi:10.1167/iovs.18-26164

64. Wang J, Saul A, Roon P, Smith SB. Activation of the molecular chaperone, sigma 1 receptor, preserves cone function in a murine model of inherited retinal degeneration. *Proc Natl Acad Sci U S A* (2016) **113**:E3764–72. doi:10.1073/pnas.1521749113

65. Trachsel-Moncho L, Benlloch-Navarro S, Fernandez-Carbonell A, Ramirez-Lamelas DT, Olivar T, Silvestre D, et al. Oxidative stress and autophagy-related changes during retinal degeneration and development. *Cell Death Dis* (2018) **9**:812. doi:10.1038/s41419-018-0855-8

66. Roehlecke C, Schumann U, Ader M, Brunssen C, Bramke S, Morawietz H, et al. Stress reaction in outer segments of photoreceptors after blue light irradiation. *PLoS One* (2013) **8**:e71570. doi:10.1371/journal.pone.0071570

67. Zhang P, Zawadzki RJ, Goswami M, Nguyen PT, Yarov-Yarovoy V, Burns ME, et al. *In vivo* optophysiology reveals that G-protein activation triggers osmotic swelling and increased light scattering of rod photoreceptors. *Proc Natl Acad Sci U S A* (2017) **114**:E2937–E46. doi:10.1073/pnas.1620572114

68. Lu CD, Lee B, Schottenhamml J, Maier A, Pugh EN, Jr, Fujimoto JG. Photoreceptor layer thickness changes during dark adaptation observed with ultrahigh-resolution optical coherence tomography. *Invest Ophthalmol Vis Sci* (2017) **58**:4632–43. doi:10.1167/iovs.17-22171

EBM Experimental Biology and Medicine

TYPE Original Research
PUBLISHED 29 February 2024
DOI 10.3389/ebm.2024.10064

OPEN ACCESS

*CORRESPONDENCE
Bahareh Ahmadi,
ahmadib@uoguelph.ca

RECEIVED 01 December 2023
ACCEPTED 30 January 2024
PUBLISHED 29 February 2024

CITATION
Ahmadi B, Duarte FCK, Srbely J and Bartlewski PM (2024), Ultrasound-based assessment of the expression of inflammatory markers in the rectus femoris muscle of rats.
Exp. Biol. Med. 249:10064.
doi: 10.3389/ebm.2024.10064

Ultrasound-based assessment of the expression of inflammatory markers in the rectus femoris muscle of rats

Bahareh Ahmadi[1]*, Felipe C. K. Duarte[2], John Srbely[3] and Pawel M. Bartlewski[1]

[1]Department of Biomedical Sciences, Ontario Veterinary College, University of Guelph, Guelph, ON, Canada, [2]School of Health, Medical and Applied Sciences, Central Queensland University, Brisbane, QLD, Australia, [3]Department of Human Health and Nutritional Sciences, College of Biological Sciences, University of Guelph, Guelph, ON, Canada

Abstract

Ultrasonographic characteristics of skeletal muscles are related to their health status and functional capacity, but they still provide limited information on muscle composition during the inflammatory process. It has been demonstrated that an alteration in muscle composition or structure can have disparate effects on different ranges of ultrasonogram pixel intensities. Therefore, monitoring specific clusters or bands of pixel intensity values could help detect echotextural changes in skeletal muscles associated with neurogenic inflammation. Here we compare two methods of ultrasonographic image analysis, namely, the echointensity (EI) segmentation approach (EI banding method) and detection of selective pixel intensity ranges correlated with the expression of inflammatory regulators using an in-house developed computer algorithm (r-Algo). This study utilized an experimental model of neurogenic inflammation in segmentally linked myotomes (i.e., rectus femoris (RF) muscle) of rats subjected to lumbar facet injury. Our results show that there were no significant differences in RF echotextural variables for different EI bands (with 50- or 25-pixel intervals) between surgery and sham-operated rats, and no significant correlations among individual EI band pixel characteristics and protein expression of inflammatory regulators studied. However, mean numerical pixel values for the pixel intensity ranges identified with the proprietary r-Algo computer program correlated with protein expression of ERK1/2 and substance P (both 86–101-pixel ranges) and CaMKII (86–103-pixel range) in RF, and were greater ($p < 0.05$) in surgery rats compared with their sham-operated counterparts. Our findings indicate that computer-aided identification of specific pixel intensity ranges was

critical for ultrasonographic detection of changes in the expression of inflammatory mediators in neurosegmentally-linked skeletal muscles of rats after facet injury.

KEYWORDS

rat, neurogenic inflammation, rectus femoris, inflammatory regulators, first order echotextural variables

Impact statement

Early detection of biochemical changes in skeletal muscles could greatly improve the diagnosis and treatment of various myopathies. There is a great deal of evidence to suggest that ultrasonographic characteristics of skeletal muscles can be used to determine their chemical composition. The main objective of the present experiment was to use computer-assisted image analysis of muscle ultrasonograms to estimate the content of neuroinflammatory regulators. We have designed and written a computer algorithm (r-Algo) to identify the specific ranges of echointensity values with the strongest correlation to the biochemical constituents of muscles in rats following the experimental facet injury. Mean echointensity values for r-Algo–detected pixel ranges (associated with the expression of affected inflammatory regulators) differed significantly

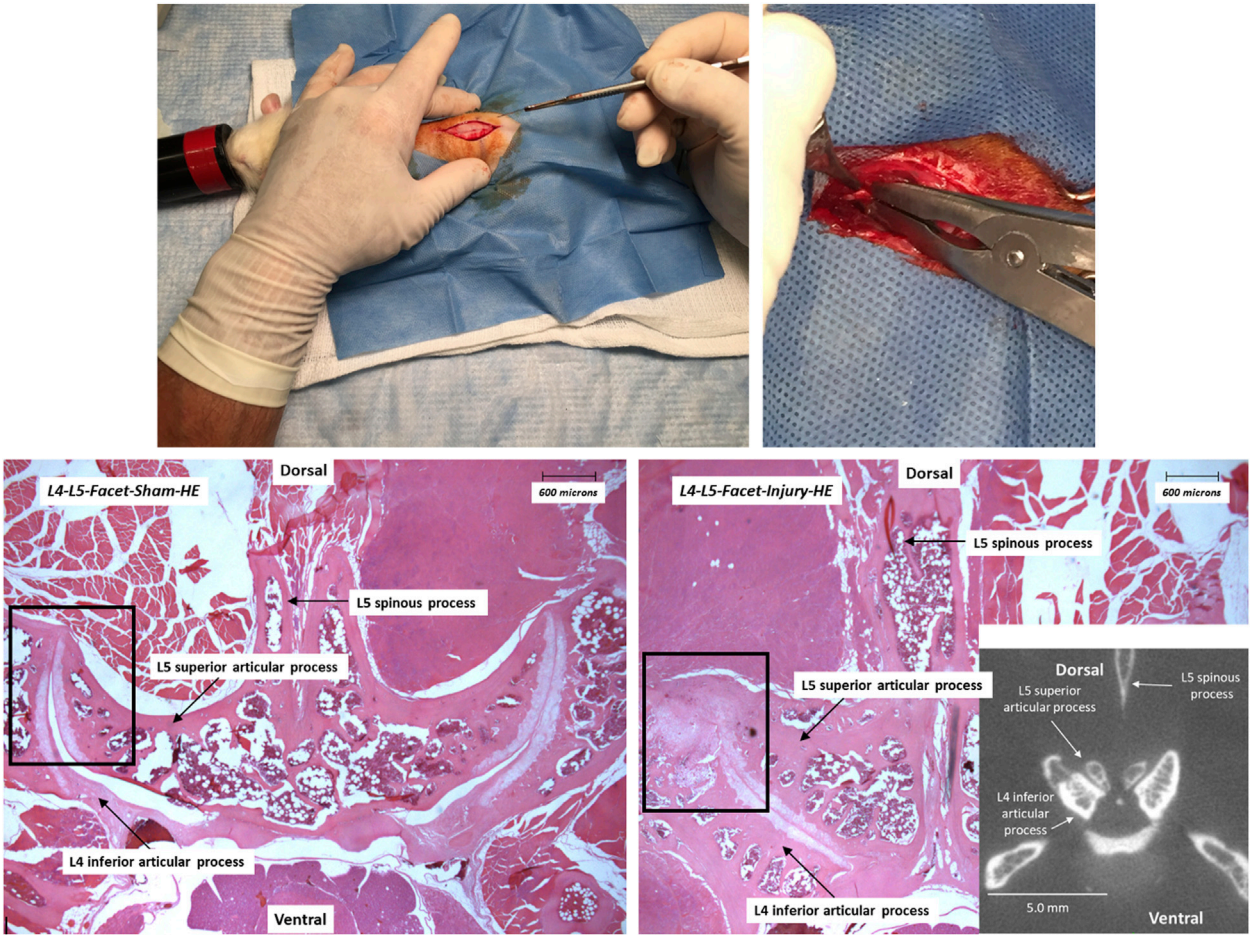

FIGURE 1
Experimental procedures (upper panels; scalpel incision and left L4-L5/L5-L6 joint compression using modified Kelly forceps) and histopathological (hematoxylin-eosin (HE) staining)/radiological (micro-CT) evaluations of the lumbar facet articular joint injury (L4-L5; lower panels) 21 days after surgical procedures in sham-operated (left) and surgery (right) rats. Targeted injury sites are delineated with rectangles. Photographic reproductions of histograms and a micro-CT scan insert show the intact L4-L5 facet joint in a sham-operated rat and the injured facet in a surgery group animal.

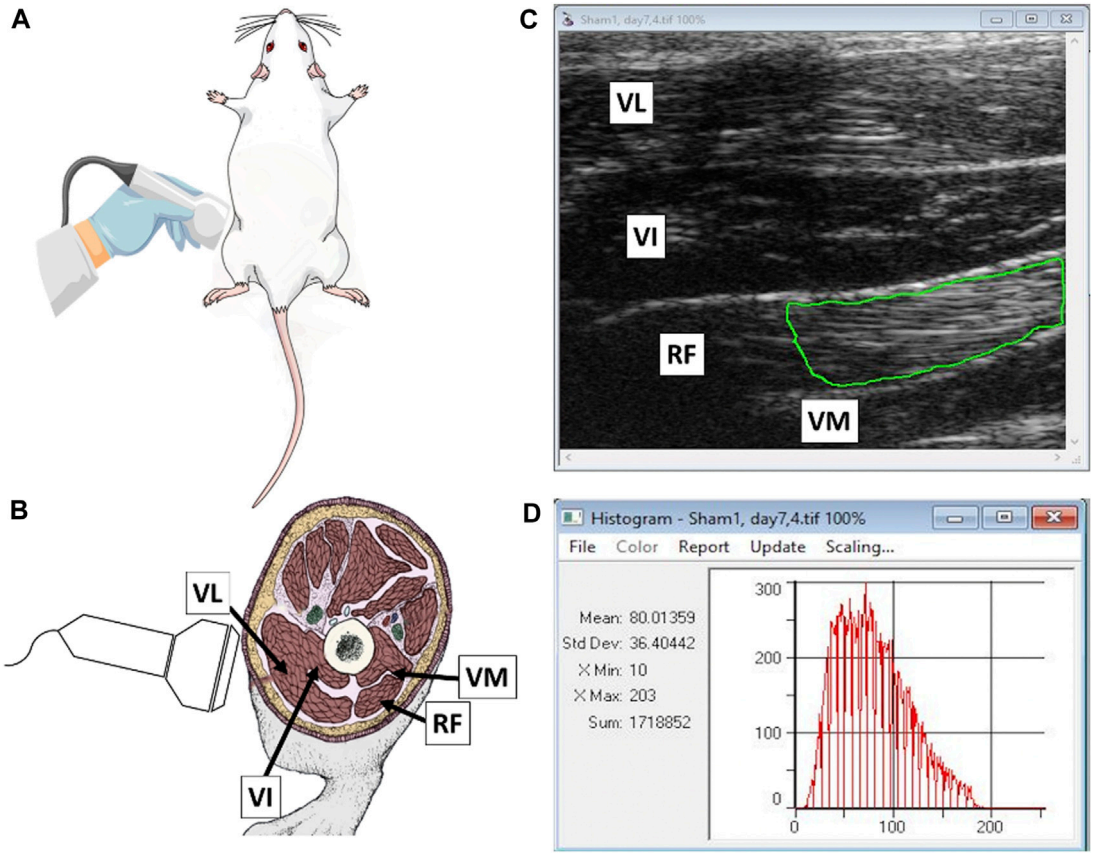

FIGURE 2
(A) Schematic illustration of the scanning technique employed to visualize hindlimb muscles of experimental rats; **(B)** topographic location of vastus lateralis (VL), vastus intermedius (VI), rectus femoris (RF) and vastus medialis (VM) muscles; **(C)** a normalized ultrasonogram containing individual muscles with a green line illustrating a possible positioning of a polygonal region of interest (ROI) used for determining echotextural characteristics of RF parenchyma; and **(D)** a summary of digital image analysis performed with ImageProPlus® computer software (Mean, mean numerical pixel values; Std Dev, pixel heterogeneity; X Min and X Max, minimal and maximal pixel intensity values within ROI; and Sum, a total number of pixels encapsulated by an ROI; a red graph is a pixel distribution histogram with pixel intensity values along the *x*-axis and the numbers of detected pixels of specific intensities on a *y*-axis).

between the surgery and sham-operated animals. These results indicate that r-Algo provides a novel and effective method of quantitative image analysis, with multiple potential applications in biomedical research, medicine, and industry.

Introduction

Muscle inflammation plays a significant role in the etiology of many diseases, including primary inflammatory myopathy and several muscular dystrophies [1]. Various approaches are available for diagnosing and monitoring muscle inflammation, including magnetic resonance imaging (MRI), computed tomography (CT), and skeletal muscle biopsies; however, these techniques are invasive (muscle biopsies), expose the individual to ionizing radiation (CT), or have limited accessibility (MRI) [2, 3]. Still, developing a non-invasive or minimally invasive method for detecting and monitoring microstructural and biochemical alterations during myositis (idiopathic or neurologic) has lagged behind [1, 4].

Ultrasound imaging (grey-scale B-mode) is a safe diagnostic method that permits visualization of internal organs and tissues with relatively high spatial resolution [5]. Its advantages can mainly be attributed to "real-time" capabilities and the fact that it enables the clinicians to sample patients with much greater frequency than with other imaging techniques, thereby providing greater sensitivity/specificity to the diagnosis and treatment responses of patients [4, 5]. This technique is increasingly used for soft tissue evaluations in a wide range of medical fields [4]. However, the interpretation of ultrasonographic findings is heavily dependent on the diagnosticians' expertise and image quality. Furthermore, B-mode image echointensity is variable and likely dependable on the machine/system settings and operator, making comparisons across diagnostic centers difficult and inconsistent [4]. In 1989,

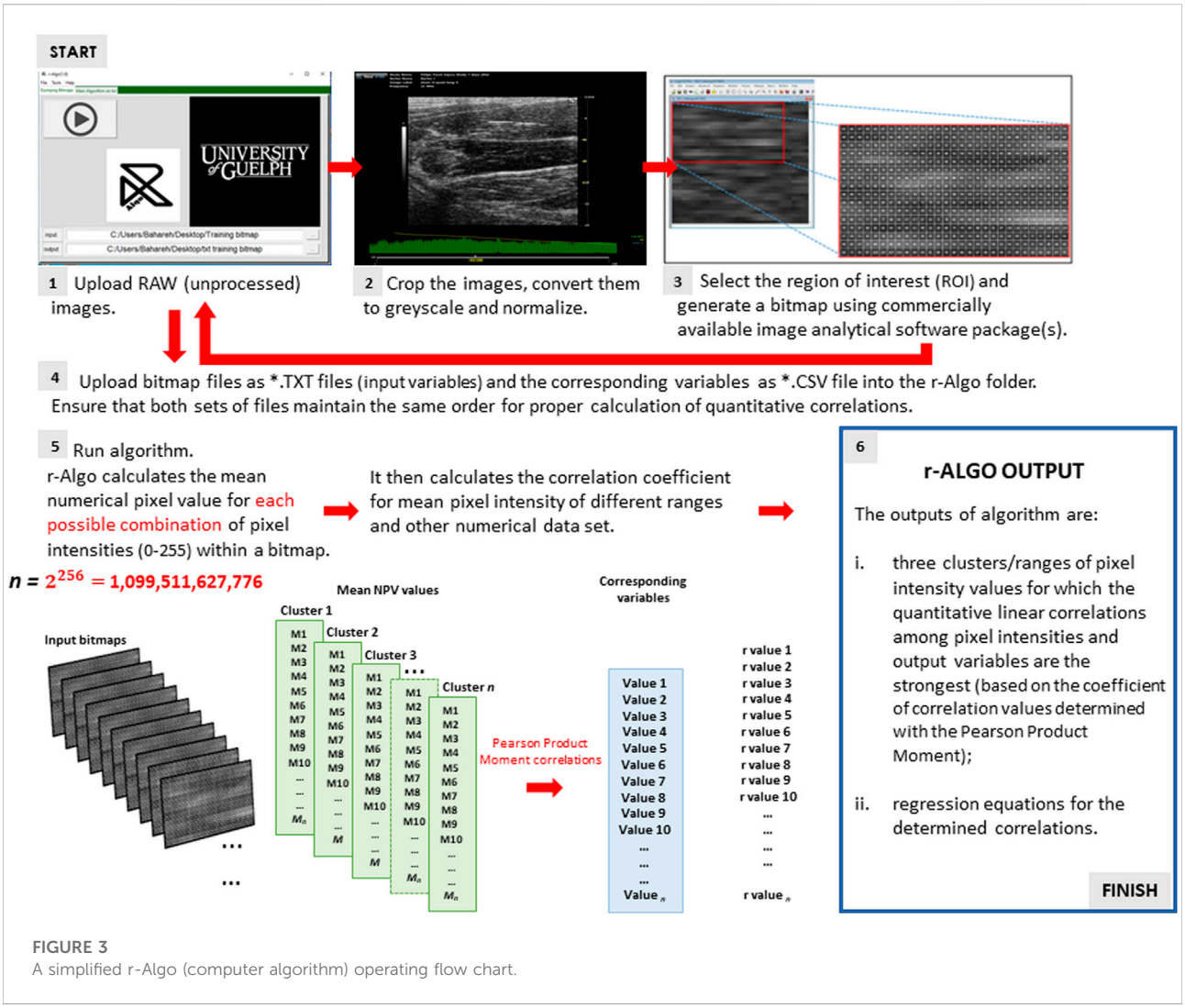

FIGURE 3
A simplified r-Algo (computer algorithm) operating flow chart.

Heckmatt et al. [6] developed quantitative sonography of skeletal muscles, which is less dependent on operator's experience as well as more objective and accurate compared with visual inspection of ultrasonograms. Using this approach, muscle echotextural features are computed within a specific region of interest (ROI) [6]. Since then, numerical echo intensity (EI) values have become the most commonly used ultrasound-based measure of skeletal muscle status [7–10]. Several ensuing studies confirmed that muscle EI was a useful and practical surrogate measure of skeletal muscle health and functional capacity [7–10], particularly in diagnosing and evaluating the progression of numerous neuromuscular disorders associated with the inflammatory process [11]. However, EI still provides limited information on muscle chemical constituents [12]. The biochemical composition of skeletal muscles is known to change during the development of pathological conditions [1, 4]. Therefore, it is important to describe the accompanying echotextural changes in order for transcutaneous ultrasonography to become a useful technique in detecting and frequently monitoring muscle inflammation. Recently, Pinto and Pinto [13] observed that EI capturing a complete range of pixel intensities or numerical pixel values of the organ of interest (ranging from 0 (absolute black) to 255 (absolute white)) might convey inadequate information on their chemical composition and/or the extent of histomorphological changes. Therefore, assessing EI parameters and pixel distribution within different EI clusters of the grey-scale histogram may provide more accurate information on muscle internal characteristics [13]. New ultrasound image processing and analysis methods are urgently needed to obtain critical information on tissue chemical composition.

Given these lines of evidence, we developed a computer algorithm (provisionally called r-Algo). First, the program screens the numerical pixel values in the images/specified ROIs. Next, it identifies the conglomerates or groups of pixel values for which the linear correlations between echogenic and other quantitative characteristics of the tissue (including those determined *ex situ*

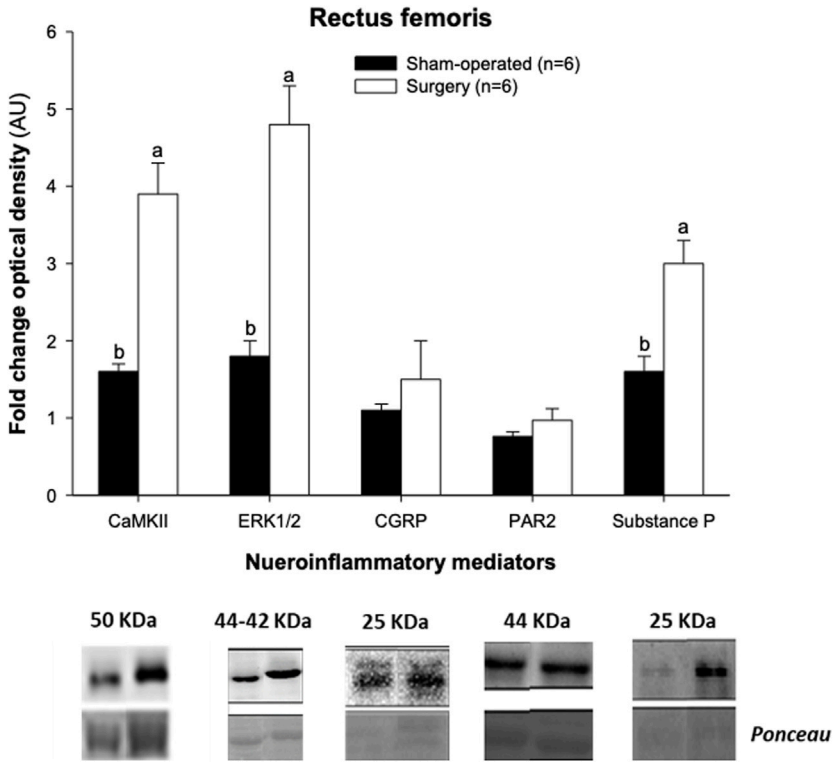

FIGURE 4
Relative protein expression of inflammatory mediators determined in left rectus femoris homogenates obtained post-mortem 21 days after experimental procedures from sham-operated and experimental surgery (lumbar L4-L6 facet injury) Kyoto Wistar rats. Ponceau is the generic name for a family of azo dyes used for gel staining. CaMKII, Ca^{2+}/calmodulin-dependent protein kinase II; ERK1/2, proline-directed kinases; CGRP, calcitonin-gene related peptide; and PAR2, protease-activated receptor-2. ab, $p < 0.05$.

with various laboratory techniques) are strongest (based on the value of correlation coefficient-r). The r-Algo calculates mean numerical pixel values for each possible combination of pixels in the image bitmap (with luminance values ranging from 0 to 255), and computes correlation coefficients between pixel intensity for all pixel ranges/clusters (input variables) and any equinumerous data set (output variables), using the Pearson Product moment analysis. Lastly, the software reports a continuous pixel range or a scattered group of pixels for which the strongest linear correlation between the two sets of quantitative data (echotextural and other) has been identified.

The aim of this work was to develop methodological and statistical criteria whereby the linear association between the combination of nominal pixel values and protein expression of inflammatory mediators in the affected skeletal muscles of rats could be established. In addition, we applied the r-Algo program to: i. assess the suitability of using the predictive pixel intensity ranges for detecting differences in the expression levels of inflammatory mediators; and ii. compare this approach with the EI banding method using two "arbitrary" pixel ranges most commonly employed in the past studies (with the 50- and 25-pixel intervals). The existence of such quantitative relationships would greatly enhance the sensitivity and specificity of this clinically-feasible diagnostic approach (ultrasound imaging combined with computer-aided image analysis) for the monitoring and management of inflammatory muscle disease.

Materials and methods

Experimental procedures

The Animal Care Committee of the University of Guelph (Guelph, ON, Canada) had approved all experimental procedures involving live animals. The present retrospective study used the original data and ultrasound images obtained and analyzed by Duarte et al. [14] and Ahmadi et al. [15], but with the new discriminating image analysis of muscle ultrasonograms. Twelve sexually mature male Wistar Kyoto rats, aged 13 ± 5 months, were housed (2–3 animals per cage) in a room with a 12-hour alternating light-dark cycle and a stable temperature (23.0 ± 1.0°C). All animals received pellet diet *ad libitum*. Animals were divided into two groups: surgery (animals that subsequently underwent facet compression at lumbar segments L4-L6 on the left side;

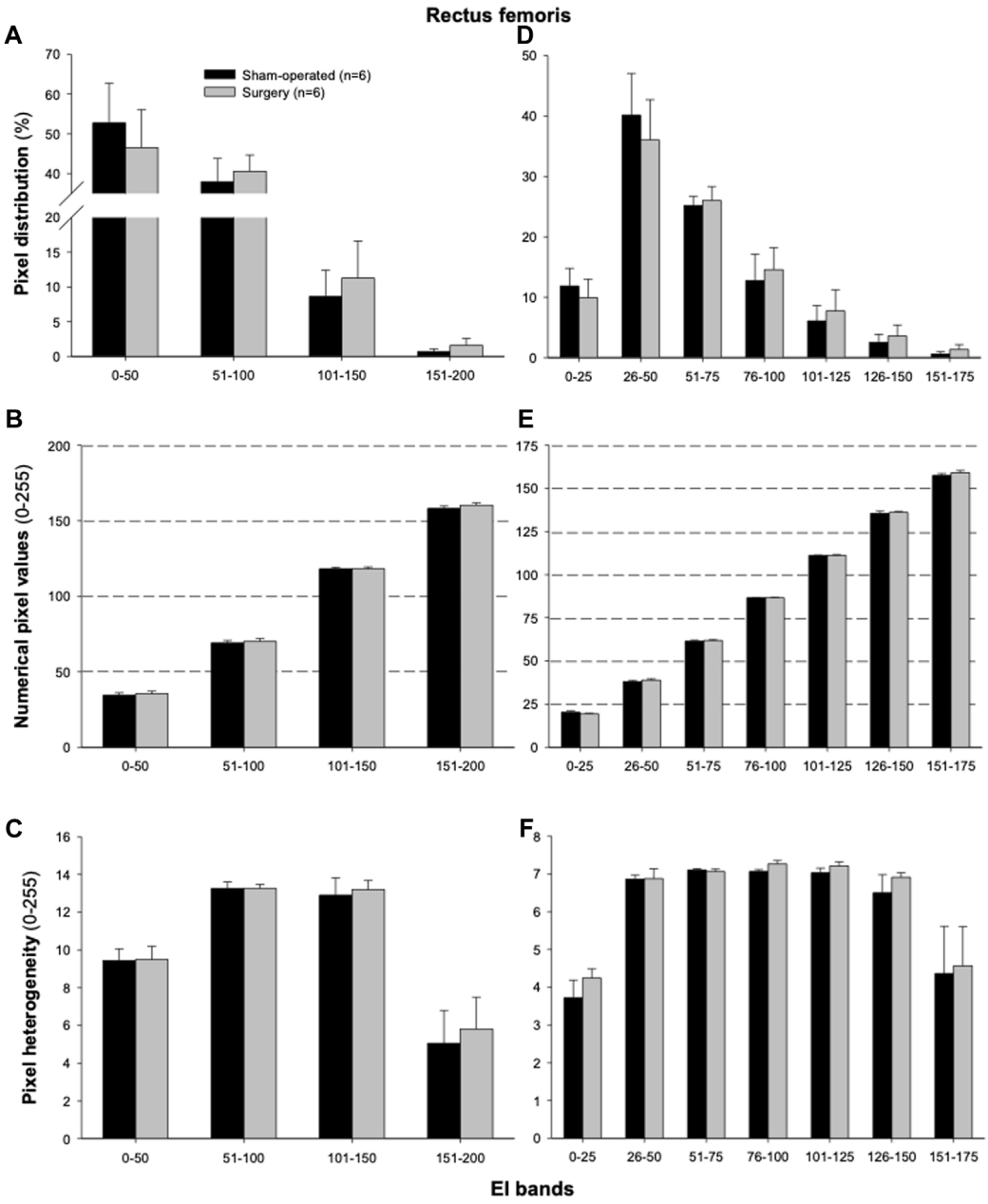

FIGURE 5
Mean (±SEM) pixel frequency distribution **(A,D)**, intensity [numerical pixel values; **(B,E)**], and heterogeneity **(C,F)** of the rectus femoris muscle ultrasonograms for echointensity (EI) bands with the 50- **(A–C)** or 25-pixel intervals **(D–F)**. Ultrasonographic images of the hindlimbs were taken 3 weeks after the lumbar (L4-L6) facet injury in six sham-operated and six surgically treated rats.

Figure 1), and sham-operated (animals with left side facets exposed but without facet compression) [16, 17]. A non-steroidal anti-inflammatory drug carprofen (5 mg/kg body mass) was administered subcutaneously 30 min before surgical procedures. Both surgery and sham animals were anesthetized using 4% isoflurane and had a local anesthesia applied over the incision site (2–5 mg/kg of 50/50 lidocaine/bupivacaine). Once animals were anesthetized, a posterior midline incision of skin and subcutaneous tissue was made along the L2 to L6 spinous processes. A lumbar muscle at the L3-L4-L5 spinous process (multifidus) was resected to expose the lumbar facet capsule. In the experimental facet surgery group, the left L4-L5 and L5-L6 facet joints were then compressed with modified Kelly forceps. All muscles were sutured (braided 4-0 coated vicryl) and the skin

TABLE 1 A summary of correlational analyses among pixel frequency distribution (EI%) within individual echointensity bands (EI 0–50 to EI 151–200) and the protein expression of inflammatory mediators measured in the rectus femoris muscle of sham-operated rats and their surgically treated counterparts that underwent experimental lumbar facet (L4-L6) injury.

Expression of inflammatory regulators	EI% (EI band)	*r*	*p*-value
CaMKII	EI% (0–50)	−0.30	0.36
	EI% (51–100)	0.16	0.63
	EI% (101–150)	0.37	0.27
	EI% (151–200)	0.48	0.13
ERK1/2	EI% (0–50)	−0.13	0.71
	EI% (51–100)	0.10	0.78
	EI% (101–150)	0.12	0.72
	EI% (151–200)	0.22	0.51
CGRP	EI% (0–50)	0.04	0.90
	EI% (51–100)	0.19	0.58
	EI% (101–150)	−0.24	0.48
	EI% (151–200)	−0.19	0.57
PAR2	EI% (0–50)	0.06	0.86
	EI% (51–100)	0.08	0.81
	EI% (101–150)	−0.18	0.59
	EI% (151–200)	−0.16	0.64
Substance P	EI% (0–50)	−0.02	0.94
	EI% (51–100)	−0.09	0.79
	EI% (101–150)	0.10	0.78
	EI% (151–200)	0.26	0.43

Abbreviations used are follows: CaMKII, Ca^{2+}/calmodulin-dependent protein kinase II; ERK1/2, proline-directed kinases; CGRP, calcitonin-gene related peptide; and PAR2, protease-activated receptor-2.

was closed using stainless-steel staples. After regaining consciousness, rats were returned to their cages and maintained in the same conditions as prior to surgical manipulations. The effectiveness of surgical procedures was verified 21 days later with histopathological examinations and micro-CT scans (Figure 1).

Ultrasound scanning and image acquisition

Transcutaneous ultrasonography of various muscle groups in the rats of the present sudy has been detailed previously [14, 15]. All ultrasound images of the rectus femoris muscle 21 days after surgical interventions were recorded in B-mode using the Vevo 2100 Visuals Sonic Ultrasound Diagnostic Medical Imaging System (Visual Sonic Inc., Toronto, ON, Canada; Figure 2). The equipment settings for transducer frequency (24 MHz), overall and near/far gain, contrast, and focal points were kept constant throughout the entire study. To eliminate a scale bar and all typed characters in the image text area, digital images were cropped, converted to grayscale images with a bit depth of eight ranges and pixel intensity from 0 (absolute black) to 255 (absolute white), and then normalized using a r-Algo and the following formula: $G_i = T\ (f_i - f_{min})/(f_{max} - f_{min})$, where f_i was the original intensity in the range (f_{min}, f_{max}) and G_i was the corresponding scaled intensity to lie within (0,T).

Western blotting of inflammatory regulators

All animals were euthanized with carbon dioxide on Day 21 of the experiment (Day 0 = surgery) and the samples of the rectus femoris were collected for Western blot analyses of inflammatory regulators, as described previously by Ahmadi et al. [15]. Muscle samples (each 20–30 mg) were frozen and then homogenized with cell lysis buffer (NP40 CLB-FNN0021; Thermo Scientific Fisher, Canada) containing protease inhibitor and serine protease inhibitor

TABLE 2 A summary of correlational analyses among pixel frequency distribution (EI%) within individual echointensity bands (EI 0–25 to EI 151–175) and the protein expression of inflammatory mediators measured in the rectus femoris muscle of sham-operated rats and their surgically-treated counterparts that underwent experimental lumbar facet (L4-L6) injury.

Expression of inflammatory regulators	EI% (EI band)	*r*	*p*-value
CaMKII	EI% (0–25)	−0.25	0.46
	EI% (26–50)	−0.30	0.37
	EI% (51–75)	−0.11	0.76
	EI% (76–100)	0.25	0.45
	EI% (101–125)	0.36	0.27
	EI% (126–150)	0.37	0.26
	EI% (151–175)	0.48	0.14
ERK1/2	EI% (0–25)	−0.08	0.81
	EI% (26–50)	−0.15	0.65
	EI% (51–75)	0.03	0.94
	EI% (76–100)	0.11	0.76
	EI% (101–125)	0.12	0.73
	EI% (126–150)	0.12	0.72
	EI% (151–175)	0.22	0.51
CGRP	EI% (0–25)	−0.18	0.60
	EI% (26–50)	0.13	0.69
	EI% (51–75)	0.57	0.07
	EI% (76–100)	−0.05	0.87
	EI% (101–125)	−0.27	0.43
	EI% (126–150)	−0.19	0.58
	EI% (151–175)	−0.17	0.61
PAR2	EI% (0–25)	−0.13	0.69
	EI% (26–50)	0.15	0.66
	EI% (51–75)	0.28	0.41
	EI% (76–100)	−0.04	0.91
	EI% (101–125)	−0.19	0.57
	EI% (126–150)	−0.15	0.65
	EI% (151–175)	−0.15	0.66
Substance P	EI% (0–25)	0.05	0.88
	EI% (26–50)	−0.06	0.86
	EI% (51–75)	−0.14	0.68
	EI% (76–100)	−0.04	0.90
	EI% (101–125)	0.09	0.80
	EI% (126–150)	0.11	0.75
	EI% (151–175)	0.26	0.44

Abbreviations used are follows: CaMKII, Ca^{2+}/calmodulin-dependent protein kinase II; ERK1/2, proline-directed kinases; CGRP, calcitonin-gene related peptide; and PAR2, protease-activated receptor-2.

TABLE 3 A summary of correlational analyses among mean numerical pixel values (NPV) and pixel heterogeneity (SD of numerical pixel values) within individual echointensity bands (EI 0–50 to EI 151–200) and the protein expression of inflammatory mediators measured in the rectus femoris muscle of sham-operated rats and their surgically treated counterparts that underwent experimental lumbar facet (L4-L6) injury.

Expression of inflammatory regulators	NPV (EI band)	*r*	*p*-value	SD (EI band)	*r*	*p*-value
CaMKII	NPV (0–50)	0.31	0.36	SD (0–50)	−0.16	0.64
	NPV (51–100)	0.32	0.34	SD (51–100)	−0.05	0.89
	NPV (101–150)	0.09	0.79	SD (101–150)	0.12	0.73
	NPV (151–200)	0.26	0.44	SD (151–200)	0.23	0.50
ERK1/2	NPV (0–50)	0.10	0.77	SD (0–50)	0.007	0.98
	NPV (51–100)	0.15	0.65	SD (51–100)	0.05	0.87
	NPV (101–150)	−0.06	0.85	SD (101–150)	−0.02	0.96
	NPV (151–200)	0.42	0.20	SD (151–200)	0.11	0.74
CGRP	NPV (0–50)	0.08	0.82	SD (0–50)	−0.02	0.96
	NPV (51–100)	−0.18	0.60	SD (51–100)	0.01	0.97
	NPV (101–150)	0.28	0.40	SD (101–150)	0.31	0.35
	NPV (151–200)	−0.07	0.83	SD (151–200)	−0.06	0.85
PAR2	NPV (0–50)	0.10	0.76	SD (0–50)	−0.12	0.73
	NPV (51–100)	−0.12	0.72	SD (51–100)	−0.11	0.74
	NPV (101–150)	0.18	0.60	SD (101–150)	0.14	0.67
	NPV (151–200)	−0.51	0.11	SD (151–200)	−0.36	0.27
Substance P	NPV (0–50)	−0.005	0.99	SD (0–50)	0.13	0.71
	NPV (51–100)	0.03	0.94	SD (51–100)	−0.10	0.77
	NPV (101–150)	−0.03	0.92	SD (101–150)	0.009	0.98
	NPV (151–200)	0.52	0.10	SD (151–200)	0.19	0.57

Abbreviations used are follows: CaMKII, Ca^{2+}/calmodulin-dependent protein kinase II; ERK1/2, proline-directed kinases; CGRP, calcitonin-gene related peptide; and PAR2, protease-activated receptor-2.

phenylmethylsulphonyl fluoride (PMSF). A copper-based assay using bicinchoninic acid (BCA) protein detection kit (Pierce BCA Protein Assay; Thermo Scientific, Canada) was used to determine protein content in the homogenized samples [18]. Equal amounts of muscle sample proteins (15 μg) were separated by sodium dodecyl sulfate-polyacrylamide gel (15%) electrophoresis and transferred for 1 h at 0.2 A onto a polyvinylidene difluoride membrane. Membranes were blocked in 5% non-fat skim milk tris-buffered saline (TBS-T) containing 0.1% tween-20 for 1 h at room temperature followed by an overnight incubation at 4°C with primary antibodies diluted in 5% bovine serum albumin. The primary antibodies used were as follows: anti-substance P antibody at 1:500 (orb215527), anti-calcitonin-gene related peptide (CGRP) 1:250 (orb182870) and anti-protease-activated receptor-2 (PAR2) antibody at 1:500 (orb385619); Biorbyt Ltd., San Franciso, CA, United States; anti-proline-directed kinases (ERK1/2) antibody at 1:1,000 (#9102); and anti-Ca^{2+}/calmodulin-dependent protein kinase II (CaMKII) antibody at 1:1,000 (#4436); Cell Signaling Technology, Denver, MA, United States. After three washes in TBS-T, the membranes were incubated at room temperature for 1 h with the secondary antibody (anti-rabbit—1: 2000, A0545; Sigma-Aldrich, Oakville, ON, Canada). Protein bands were detected using enhanced chemiluminescence (PerkinElmer; Waltham, MA, United States) and relative protein content was quantified by densitometry using a chemiluminescence detection system (Alpha Innotech Fluorchem HD2, Fisher Scientific, Hampton, NH, United States); all results were normalized against the loading control (alpha-tubulin protein, ab7291; Abcam, Cambridge, MA, United States).

Image analysis based on arbitrarily chosen clusters of echointensity values (EI bands)

The regions of interest in the images containing the largest cross-sectional area of the rectus femoris were delineated using a polygonal tool and subjected to the bitmap analysis using ImageProPlus® analytical software (Media Cybernetics Inc.,

TABLE 4 A summary of correlational analyses among mean numerical pixel values (NPV) and pixel heterogeneity (SD of numerical pixel values) within individual echointensity bands (EI 0–25 to EI 151–175) and the protein expression of inflammatory mediators measured in the rectus femoris muscle of sham-operated rats and their surgically treated counterparts that underwent experimental lumbar facet (L4-L6) injury.

Expression of inflammatory regulators	NPV (EI band)	*r*	*p*-value	SD (EI band)	*r*	*p*-value
CaMKII	NPV (0–25)	−0.31	0.35	SD (0–25)	0.35	0.29
	NPV (26–50)	0.39	0.24	SD (26–50)	−0.21	0.53
	NPV (51–75)	0.35	0.30	SD (51–75)	0.04	0.90
	NPV (76–100)	0.124	0.72	SD (76–100)	0.24	0.47
	NPV (101–125)	0.06	0.85	SD (101–125)	0.12	0.72
	NPV (126–150)	0.158	0.64	SD (126–150)	0.16	0.64
	NPV (151–175)	0.09	0.79	SD (151–175)	0.06	0.87
ERK1/2	NPV (0–25)	−0.28	0.41	SD (0–25)	0.32	0.33
	NPV (26–50)	0.20	0.55	SD (26–50)	−0.07	0.83
	NPV (51–75)	0.16	0.63	SD (51–75)	−0.32	0.34
	NPV (76–100)	0.03	0.92	SD (76–100)	0.54	0.09
	NPV (101–125)	0.04	0.90	SD (101–125)	0.41	0.21
	NPV (126–150)	0.01	0.97	SD (126–150)	0.26	0.45
	NPV (151–175)	0.49	0.12	SD (151–175)	0.11	0.75
CGRP	NPV (0–25)	0.21	0.53	SD (0–25)	−0.31	0.36
	NPV (26–50)	0.003	0.99	SD (26–50)	0.25	0.46
	NPV (51–75)	−0.23	0.50	SD (51–75)	−0.28	0.39
	NPV (76–100)	−0.38	0.24	SD (76–100)	0.02	0.95
	NPV (101–125)	0.09	0.79	SD (101–125)	0.21	0.54
	NPV (126–150)	0.27	0.43	SD (126–150)	0.28	0.41
	NPV (151–175)	0.07	0.83	SD (151–175)	0.08	0.81
PAR2	NPV (0–25)	0.25	0.46	SD (0–25)	−0.30	0.38
	NPV (26–50)	−0.02	0.96	SD (26–50)	0.13	0.71
	NPV (51–75)	−0.16	0.64	SD (51–75)	−0.21	0.53
	NPV (76–100)	−0.51	0.11	SD (76–100)	0.16	0.64
	NPV (101–125)	0.18	0.60	SD (101–125)	0.08	0.81
	NPV (126–150)	0.13	0.70	SD (126–150)	0.09	0.78
	NPV (151–175)	−0.54	0.08	SD (151–175)	−0.43	0.19
Substance P	NPV (0–25)	−0.46	0.16	SD (0–25)	0.45	0.16
	NPV (26–50)	0.13	0.69	SD (26–50)	−0.006	0.99
	NPV (51–75)	0.03	0.94	SD (51–75)	−0.45	0.17
	NPV (76–100)	0.16	0.64	SD (76–100)	0.35	0.29
	NPV (101–125)	0.08	0.82	SD (101–125)	0.41	0.22
	NPV (126–150)	0.06	0.86	SD (126–150)	0.16	0.63
	NPV (151–175)	0.57	0.07	SD (151–175)	0.17	0.62

Abbreviations used are follows: CaMKII, Ca^{2+}/calmodulin-dependent protein kinase II; ERK1/2, proline-directed kinases; CGRP, calcitonin-gene related peptide; and PAR2, protease-activated receptor-2.

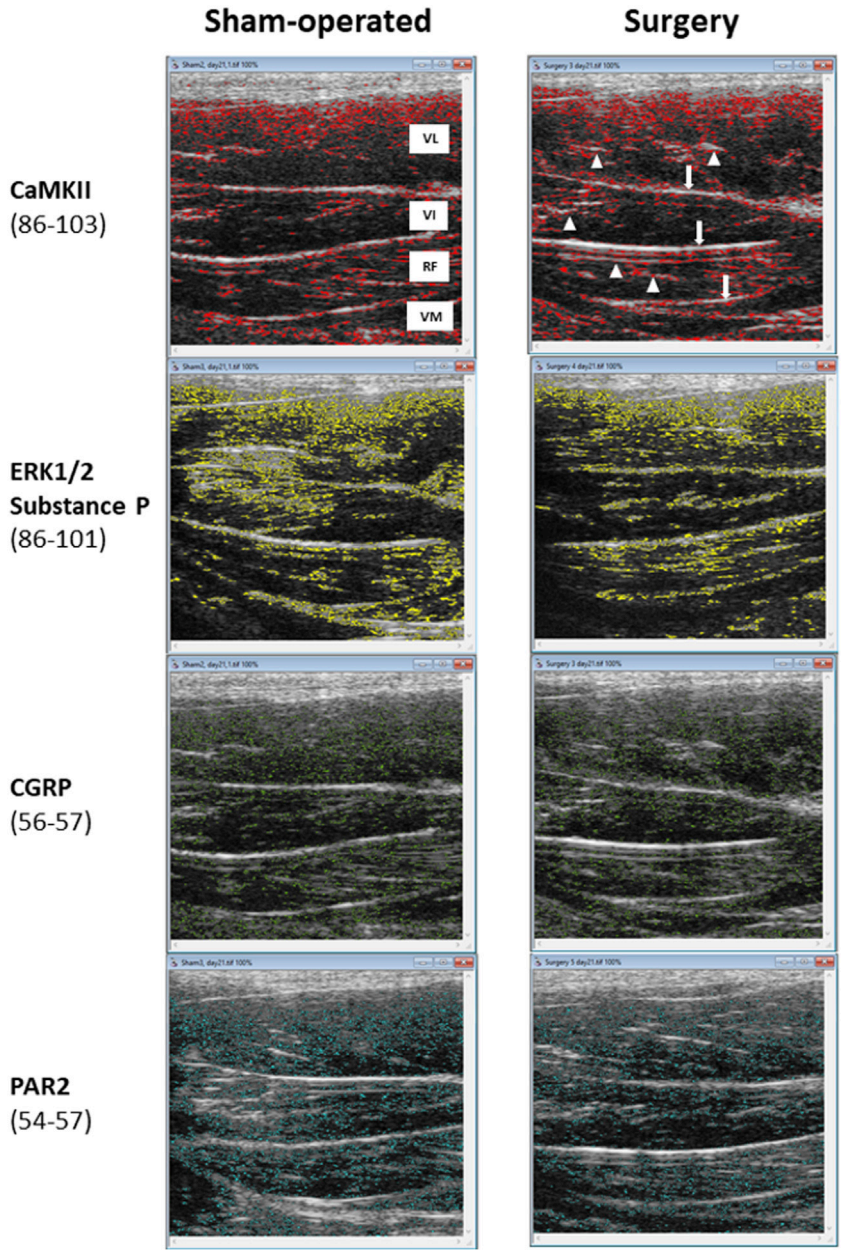

FIGURE 6
The threshold mapping of specific pixel intensity ranges identified by the r-Algo computer program for which mean numerical pixel values were highly and significantly correlated with the protein expression of neuroinflammatory regulators in the rectus femoris muscle of rats (sham-operated and surgery) after the experimental L4-L6 facet injury. Abbreviations in the top left panel are as follows: VL-vastus lateralis; VI-vastus intermedius; RF-rectus femoris; and VM-vastus medialis. White arrows in a top right panel indicate the perimysial layers and arrowheads point at scattered epimysial septa.

Rockville, MD, United States). Bitmap analysis organizes and displays the values of individual pixels in a bitmapped image/rectangular ROI. Using the "Save" command on the "Histogram and Bitmap Analysis" file tab, the results of the analysis were stored in a file for processing with other applications at a later date. All tabulated pixels from the grayscale (B-mode) matrix were exported to a customized Excel spreadsheet to calculate the mean pixel intensity (numerical pixel values-NPV) and heterogeneity (standard deviation (SD) of mean numerical pixel values) in the ranges of: i. 0–50, 51–100, 101–150, 151–200, and 201–255 or 0–25, 26–50, 51–75, 76–100, 101–1,025, 126–150, 151–175, 176–200, 201–225, 226–250, and 251–255.

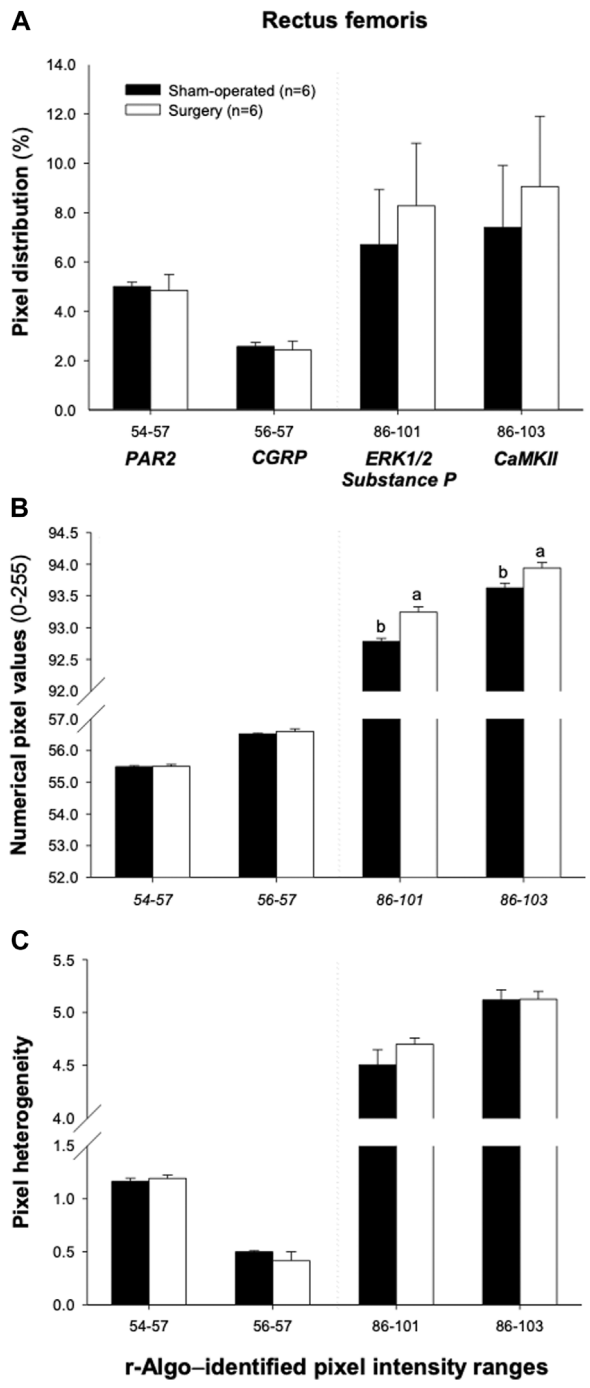

FIGURE 7
Mean (±SEM) pixel frequency distribution **(A)**, intensity [numerical pixel values; **(B)**], and heterogeneity **(C)** of the rectus femoris muscle ultrasonograms, for specific echointensity (EI) ranges identified by the r-Algo computer program (for which mean numerical pixel values were highly and significantly correlated with the protein expression of neuroinflammatory regulators). Ultrasonographic images of the hindlimbs were obtained in 6 sham-operated and 6 surgery rats that underwent the experimental L4-L6 facet injury. Abbreviations used are follows: Ca^{2+}/calmodulin-dependent protein kinase II (CaMKII); proline-directed kinases (ERK1/2); calcitonin-gene related peptide (CGRP); and protease-activated receptor-2 (PAR2).

Image analysis using in-house Python algorithm r-Algo

The mean value for pixel intensities for each possible combination of individual pixel values (0–255) within each bitmap (2^{256} = 1,099,511,627,776) were calculated by r-Algo. The program also computed coefficients of correlation between averaged values for all pixel value combinations/clusters (input variables) and the expression of inflammatory mediators (output variables: Figure 3). Lastly, the r-Algo identified a pixel range with the strongest linear correlation (highest correlation coefficient) for each output variable.

Statistical comparisons and correlational analyses

All statistical tests were completed using the SigmaPlot® program (Systat Software Inc., San Jose, CA, United States). The percentages of pixels in different numerical pixel value ranges (EI bands 50 and 25) as well as the differences in mean pixel intensity and heterogeneity values between the two groups of animals (surgery and sham-operated) were analyzed for each EI range by Student *t*-test. Similarly, pixel distribution, as well as mean pixel intensity and heterogeneity values for specific pixel ranges identified with the r-Algo, were compared between surgery and sham-operated rats by Student *t*-test. Correlational analyses between first order echotextural variables or pixel frequencies/distribution and the expression of inflammatory regulators utilized the Pearson Product Moment test. p-value < 0.05 was considered statistically significant and all results are expressed as mean ± standard error of the mean (SEM).

Results

Western blot studies revealed an occurrence of a 2.4-fold, 2.7-fold and 1.9-fold rise in CaMKII, ERK1/2 and substance P concentrations, respectively, in the rectus femoris of surgery rats compared with sham-operated animals (Figure 4). No effect of facet injury on the protein expression of CGRP or PAR2 in the rectus femoris was noted on Day 21 after initial experimental interventions ($p > 0.05$). The mean pixel intensity for the rectus femoris muscle did not vary significantly between surgery and sham-operated groups of experimental rats (67.5 ± 8.1 compared with 67.8 ± 7.7, respectively), and there were no correlations ($p > 0.05$) among echotextural variables determined in original ROIs and protein expression of the inflammatory regulators studied.

The proportions of pixels (pixel frequency distribution), as well as mean pixel intensity and heterogeneity values for different EI bands, are shown in Figure 5. Only one surgery group rat and no sham-operated animals had pixel intensities for the rectus femoris muscle in the 201–255 range. Similarly, only one sham-

10.3389/ebm.2024.10064

TABLE 5 A summary of correlational analyses among pixel frequency distribution (EI%) within individual echointensity bands identified by the r-Algo program and the protein expression of inflammatory mediators measured in the rectus femoris muscle of sham-operated rats and their surgically treated counterparts that underwent experimental lumbar facet (L4-L6) injury.

Expression of inflammatory regulators	r-Algo EI band	*r*	*p*-value
CaMKII	EI% (54–57)	−0.45	0.16
	EI% (56–57)	−0.25	0.46
	EI% (86–101)	0.33	0.32
	EI% (86–103)	0.33	*0.32*
ERK1/2	EI% (54–57)	0.05	0.88
	EI% (56–57)	−0.05	0.88
	EI% (86–101)	0.16	*0.64*
	EI% (86–103)	0.15	0.67
CGRP	EI% (54–57)	0.41	0.21
	EI% (56–57)	−0.21	*0.53*
	EI% (86–101)	−0.14	0.67
	EI% (86–103)	−0.16	0.64
PAR2	*EI% (54–57)*	0.06	*0.86*
	EI% (56–57)	−0.52	0.10
	EI% (86–101)	−0.12	0.72
	EI% (86–103)	−0.12	0.72
Substance P	EI% (54–57)	0.12	0.72
	EI% (56–57)	0.08	0.82
	EI% (86–101)	0.06	*0.86*
	EI% (86–103)	0.04	0.89

EI band ranges specific for the individual inflammatory mediators listed in the first column are indicated with italics. Abbreviations used are follows: CaMKII: Ca^{2+}/calmodulin-dependent protein kinase II; ERK1/2: proline-directed kinases; CGRP: calcitonin-gene related peptide; and PAR2: protease-activated receptor-2.

operated rat and three surgery rats had pixel intensity values within the 176–200 range. All animals' ultrasonograms contained numerical pixel values in the lower intensity ranges or bands (≤175). There were no significant differences in the mean pixel intensity and heterogeneity for different EI bands between the surgery and sham-operated groups (Figures 5B, C, E, F). There were no significant correlations ($p > 0.05$) among pixel percentages (Tables 1, 2) or first order echotextural variables in the 50 or 25 EI bands (Tables 3, 4) and the expression of inflammatory regulators studied.

The ranges of pixel intensities identified with the r-Algo program, for which there were the strongest linear relationships with the protein expression of inflammatory mediators measured in the rectus femoris of surgery and sham-operated rats, were as follows: PAR2: 54–57; CGRP: 56–57; ERK1/2 and substance P: 86–101, and CaMKII: 86–103. Images illustrating the spatial distribution of pixels within the pixel ranges above are given in Figure 6. There were no differences ($p > 0.05$) in the percentages of pixels within specific ranges (relative to all pixels in ROI) between the surgery and sham-operated groups (Figure 7A). Mean NPVs for the pixel ranges corresponding to ERK1/2 and substance P (86–101) and CaMKII (86–103) were greater ($p < 0.05$) in surgery rats compared with their sham-operated counterparts (Figure 7B). However, no significant differences were observed for pixel heterogeneity values of any specific pixel range (Figure 7C). There were no significant correlations among the percentages of pixels in the pixel ranges determined with the r-Algo and the expression levels of inflammatory mediators (Table 5). Pearson Product Moment analyses revealed a lack of linear relationships among NPV values in the non-corresponding pixel ranges and the expression of inflammatory regulators. There were no significant correlations among pixel heterogeneity and the expression of inflammatory regulators except for pixel heterogeneity SD (56–57) and CGRP protein expression ($r = -0.94$, $p = 0.00002$) and SD (56–57; an NPV region partially overlapping the 54–57 region specific for PAR2) and PAR2 protein expression in the rectus femoris of rats ($r = -0.78$, $p = 0.004$; Table 6).

TABLE 6 A summary of correlational analyses among mean numerical pixel values (NPV) and pixel heterogeneity (SD of numerical pixel values) within individual echointensity bands identified by the r-Algo program and the protein expression of inflammatory mediators measured in the rectus femoris muscle of sham-operated rats and their surgically treated counterparts that underwent experimental lumbar facet (L4-L6) injury.

Expression of inflammatory regulators	NPV (r-Algo EI band)	*r*	*p*-value	SD (r-Algo EI band)	*r*	*p*-value
CaMKII	NPV (54–57)	0.24	0.48	SD (54–57)	0.18	0.60
	NPV (56–57)	−0.02	0.96	SD (56–57)	−0.04	0.92
	NPV (86–101)	0.65	0.03	SD (86–101)	0.39	0.23
	NPV (86–103)	0.77	0.005	SD (86–103)	0.27	0.42
ERK1/2	NPV (54–57)	0.02	0.94	SD (54–57)	0.06	0.87
	NPV (56–57)	0.25	0.46	SD (56–57)	−0.25	0.46
	NPV (86-101)	0.87	0.0005	SD (86–101)	0.44	0.18
	NPV (86–103)	0.53	0.09	SD (86–103)	−0.07	0.83
CGRP	NPV (54–57)	−0.70	0.02	SD (54–57)	0.12	0.72
	NPV (56–57)	0.94	*0.00001*	SD (56–57)	−0.94	0.00002
	NPV (86–101)	0.02	0.95	SD (86–101)	−0.15	0.66
	NPV (86–103)	−0.26	0.45	SD (86–103)	−0.34	0.31
PAR2	*NPV (54–57)*	−0.82	*0.002*	SD (54–57)	−0.06	0.86
	NPV (56–57)	0.69	0.02	SD (56–57)	−0.78	0.004
	NPV (86–101)	−0.03	0.94	SD (86–101)	−0.33	0.32
	NPV (86–103)	−0.16	0.63	SD (86–103)	−0.45	0.17
Substance P	NPV (54–57)	0.15	0.65	SD (54–57)	−0.09	0.79
	NPV (56–57)	0.11	0.754	SD (56–57)	−0.07	0.83
	NPV (86–101)	0.78	*0.005*	SD (86–101)	0.49	0.12
	NPV (86–103)	0.46	0.15	SD (86–103)	0.05	0.89

EI band ranges specific for the individual inflammatory mediators listed in the first column are indicated with italics. Abbreviations used are follows: CaMKII, Ca^{2+}/calmodulin-dependent protein kinase II; ERK1/2, proline-directed kinases; CGRP, calcitonin-gene related peptide; and PAR2, protease-activated receptor-2.

Discussion

Transcutaneous ultrasonography has evolved significantly over the past decade. The advent of high-frequency micro-ultrasound systems enabled detection of a wide range of pathological muscle conditions, not only in clinical settings but also in non-clinical fields, particularly in studies involving small laboratory rodents [11, 19, 20]. Although ultrasound technique offers a secure means to observe the development or progression of the disease and to assess the effectiveness of treatment(s) applied, only a limited number of studies have explored the functional and morphological aspects of rodent skeletal muscles using ultrasonography [19, 20]. Despite their highly organized microarchitecture, striated muscles exhibit significant structural heterogeneity caused mainly by varying proportions of different muscle fiber types [21], fascial tissue [22, 23], innervation [24], and blood/lymphatic drainage [25]. Changes in muscle echogenicity could be related to microscopic changes occurring in any of these compartments [26]. A major difficulty in detecting and/or quantifying factors critical to inflammatory outcomes in skeletal muscles lies in the complexity of their pathomorphological arrangement. Methodical analysis of ultrasongrams is crucial for achieving proper standardization in non-medical and medical ultrasonography (i.e., enhancing the interpretation of preclinical data and thus facilitating the broader application of ultrasound imaging in clinical settings).

Muscle echogenicity is frequently used to evaluate its structural and functional integrity [19]. Several methods can be employed to assess muscle echotextural parameters. The simplest method is to visually compare the echogenicity of the muscle to that of other structures, such as subcutaneous tissue [19]. The results obtained using this approach are often imprecise due to the potential human error interpreting the differences among multiple "shades of grey" [27]. Semi-quantitative method described by Heckmatt [6] and comparing muscle echointensity with bone echogenicity has greater sensitivity to accurately diagnose pathological conditions of skeletal muscles compared with visual assessment. However,

quantitative methods utilizing the computation of echointensity values in a region of interest (ROI) have proven to be the most sensitive (90 percent overall) in detecting an array of neuromuscular disorders [6], including neuromuscular diseases (NMDs) in children [11, 28], Duchenne and Becker muscular dystrophy [29], Floppy disease [30], and spina bifida aperta [31].

Recently, Pinto and Pinto [13] have shown that assessing the concentration of pixels within different clusters of pixel echointensities (EI bands) of the grey-scale histogram can provide more accurate information on muscle constituents than the whole-image quantitative analysis. In contrast to the results of Pinto and Pinto [13], we found no significant differences in pixel echointensity, heterogeneity and distribution concentration in the rectus femoris muscle (neurosegmentally-linked myotomes) between the sham and surgery groups of rats when using the EI bands technique (with either 50- or 25-pixel intervals). Clearly, partitioning the "pixel pallete" into five or eleven bands did not "capture" or "sequester" pixel intensity values associated with the changes in an affected myotome.

Alternatively, a new method of image processing and analysis using the r-Algo, an algorithm written in Python, did identify specific ranges of pixel intensities for which mean numerical pixel values of rectus femoris were strongly correlated ($r \geq 0.77$) [32] with the protein expression of inflammatory mediators determined in our study. Mean pixel intensities for the identified regions that corresponded to inflammatory regulators differing significantly between sham-operated and surgery rats, also varied between the two subsets of animals. However, pixel frequency distribution and heterogeneity for these ranges did not vary between the surgery and sham-operated groups, and with the two exceptions (SD (54–57) vs. CGRP and SD (56–57) vs. PAR2) they did not relate to the expression of inflammatory regulators studied. Moreover, the specific EI ranges were identical for substance P and ERK1/2 (86–101), and there was a considerable overlap between the ERK1/2-substance P range (86–101) and that for CaMKII (86–103). This is intriguing since not only were the three inflammatory factors the only ones whose expression was affected 3 weeks after the experimental facet injury, but they also function synergistically during the course of neurogenic inflammation. Substance P has been shown to regulate the activation of inflammatory signaling pathways via ERK1/2 activation in macrophages, neutrophils, smooth muscle cells and muscle lymphatics, and this cascade of intracellular events mediated jointly by substance and ERK1/2 is dependent on intracellular increase in calcium [33]. Changes in p-CaMKII expression result in altered activity of the sarcoendoplasmic reticulum calcium ATPase (SERCA) pump involved in Ca^{2+} transport in muscle cells [34]. Both CGRP and PAR2, albeit exhibiting similar expression levels in the rectus femoris of surgery and sham-operated rats, also had overlapping r-Algo identified pixel intensity ranges, and their role during the neurogenic inflammation is clearly synergistis: activation of PAR2 stimulates the release of SP and CGRP from sensory nerve endings, reinforcing the neurogenic inflammation milieu [35, 36]. Collectively, these observations can be interpreted to suggest that range-specific pixel luminosity values were primary echotextural variables altered in response to the specific alterations elicited in the skeletal muscles of experimental rats by individual inflammatory regulators.

Additional ultrasonogram mapping was performed in an attempt to determine the spatial distribution of the pixels in specific ranges within the ultrasonographic images of the rectus femoris muscle. By performing the threshold mapping using ImageProPlus® program, the pixels specific for CaMKII, ERK1/2 and substance P were observed mainly near the fibroadipose septa of the muscle. It has been shown that inflammatory processes not only alter the echointensity of muscle fascicles, but also the echointensity of fibroadipose septa as they fill with inflammatory exudates [37]. Furthermore, perimysium and epimysium (fibroadipose septa) contain nerve endings that release neuropeptides, including substance P, and it has been shown that substance P stimulates transforming growth factor-1 (TGF-1), which leads to the development of fibrotic tissue in those regions of the muscle [38]. Even though it is only a speculation, it is attractive to suggest that r-Algo-aided detection of numerical pixel values associated with specific biochemical constituents may serve as an indicator of their locality and/or the extent of histomorphological changes induced by their elevated expression or accumulation.

Conclusion

Our present results indicate that identifying specific pixel intensity ranges was necessary to find significant quantitative correlations between mean numerical pixel values and protein expression of inflammatory mediators (related to putative microstructural changes in the neurosegmentally-linked skeletal muscles of rats after experimental facet injury). The application of this method of image processing and analysis may enable the extraction of critical information on quantitative relationships among first-order ultrasonographic image attributes and an array of output variables (e.g., chemical constituents or histomorphological features of the ultrasonographically examined tissue of interest). This potential feature of r-Algo warrants further studies.

Author contributions

BA: conceptualization, data curation, investigation, Formal analysis, methodology, writing–original draft, writing–review and editing. FD: conceptualization, funding acquisition, data curation, writing–review and editing. JS: conceptualization, formal analysis, funding acquisition, writing–review and editing, project

administration, and supervision. PB: conceptualization, formal analysis, funding acquisition, writing–review and editing, project administration, and supervision. All authors contributed to the article and approved the submitted version.

Data availability statement

The original contributions of the study are included in the article/supplementary material. Further inquiries can be directed to the corresponding author.

Ethics statement

All animal procedures employed in the present study were approved by the Animal Care Committee at the University of Guelph (Guelph, Ontario, Canada).

Funding

The Brazilian National Council for Scientific and Technological Development (CNPq), Canada Foundation for Innovation, and the Department of Biomedical Sciences at the University of Guelph co-funded this study. Additionally, the authors declare that this study received funding from Ontario Pork. The funder was not involved in the study design, data collection, analysis, interpretation, or the writing of this article, nor did they influence the decision to submit it for publication.

Acknowledgments

We are indebted to Zachary Silverman and Arvin Asgharyan Rezai (work-study and summer students in the Department of Biomedical Sciences, Ontario Veterinary College) for their work on the Python version of the r-Algo computer program and desktop app; Jakub (Kuba) Bartlewski (University of Guelph) for threshold image mapping and graphical illustration of the present manuscript; and Dr. David J. Hobson of the Research Innovation Office, University of Guelph, for his invaluable guidance with the r-Algo patenting process.

Conflict of interest

The authors declare that the research was conducted in the absence of any commercial or financial relationships that could be construed as a potential conflict of interest.

References

1. Dahlqvist JR, Salim R, Thomsen C, Vissing J. A quantitative method to assess muscle edema using short TI inversion recovery MRI. *Sci Rep* (2020) **10**:7246. doi:10.1038/s41598-020-64287-8

2. Hilton-Jones D. Diagnosis and treatment of inflammatory muscle diseases. *J Neurol Neurosurg Psychiatry* (2003) **74**:ii25–ii31. doi:10.1136/jnnp.74.suppl_2.ii25

3. Paris MT, Mourtzakis M. Muscle composition analysis of ultrasound images: a narrative review of texture analysis. *Ultrasound Med Biol* (2021) **47**:880–95. doi:10.1016/j.ultrasmedbio.2020.12.012

4. Kristofoor E L, Jemima A. Muscle ultrasound in inflammatory myopathies: a critical review. *J Rheum Dis Treat* (2019) **5**:069. doi:10.23937/2469-5726/1510069

5. Wells PNT, Liang HD. Medical ultrasound: imaging of soft tissue strain and elasticity. *J R Soc Interf* (2011) **8**:1521–49. doi:10.1098/rsif.2011.0054

6. Heckmatt J, Rodillo E, Doherty M, Willson K, Leeman S. Quantitative sonography of muscle. *J Child Neurol* (1989) **4**:S101–6. doi:10.1177/088307388900400115

7. Fujikake T, Hart R, Nosaka K. Changes in B-mode ultrasound echo intensity following injection of bupivacaine hydrochloride to rat hind limb muscles in relation to histologic changes. *Ultrasound Med Biol* (2009) **35**:687–96. doi:10.1016/j.ultrasmedbio.2008.10.008

8. Glover GH. Overview of functional magnetic resonance imaging. *Neurosurg Clin North America* (2011) **22**:133–9. doi:10.1016/j.nec.2010.11.001

9. Hammer HB, Fagerhol MK, Wien TN, Kvien TK. The soluble biomarker calprotectin (a S100 protein) is associated to ultrasonographic synovitis scores and is sensitive to change in patients with rheumatoid arthritis treated with adalimumab. *Arthritis Res Ther* (2011) **13**:R178. doi:10.1186/ar3503

10. Reimers CD, Fleckenstein JL, Witt TN, Müller-Felber W, Pongratz DE. Muscular ultrasound in idiopathic inflammatory myopathies of adults. *J Neurol Sci* (1993) **116**:82–92. doi:10.1016/0022-510x(93)90093-e

11. Pillen S, Verrips A, Van Alfen N, Arts IMP, Sie LTL, Zwarts MJ. Quantitative skeletal muscle ultrasound: diagnostic value in childhood neuromuscular disease. *Neuromuscul Disord* (2007) **17**:509–16. doi:10.1016/j.nmd.2007.03.008

12. Naimo MA, Varanoske AN, Hughes JM, Pasiakos SM. Skeletal muscle quality: a biomarker for assessing physical performance capabilities in young populations. *Front Physiol* (2021) **12**:706699. doi:10.3389/fphys.2021.706699

13. Pinto RS, Pinto MD. Moving forward with the echo intensity mean analysis: exploring echo intensity bands in different age groups. *Exp Gerontol* (2021) **145**:111179. doi:10.1016/j.exger.2020.111179

14. Duarte FCK, Hurtig M, Clark A, Brown S, Simpson J, Srbely J. Experimentally induced spine osteoarthritis in rats leads to neurogenic inflammation within neurosegmentally linked myotomes. *Exp Gerontol* (2021) **149**:111311. doi:10.1016/j.exger.2021.111311

15. Ahmadi B, Issa S, Duarte FC, Srbely J, Bartlewski PM. Ultrasonographic assessment of skeletal muscles after experimentally induced neurogenic inflammation (facet injury) in rats. *Exp Biol Med* (2022) **247**:1873–84. doi:10.1177/15353702221119802

16. Duarte FCK, Zwambag DP, Brown SHM, Clark A, Hurtig M, Srbely JZ. Increased substance P immunoreactivity in ipsilateral knee cartilage of rats exposed to lumbar spine injury. *Cartilage* (2020) **11**:251–61. doi:10.1177/1947603518812568

17. Henry JL, Yashpal K, Vernon H, Kim J, Im HJ. Lumbar facet joint compressive injury induces lasting changes in local structure, nociceptive scores, and inflammatory mediators in a novel rat model. *Pain Res Treat* (2012) **2012**:1–11. doi:10.1155/2012/127636

18. Cervone DT, Dyck DJ. Acylated and unacylated ghrelin do not directly stimulate glucose transport in isolated rodent skeletal muscle. *Physiol Rep* (2017) **5**:e13320. doi:10.14814/phy2.13320

19. Albayda J, Van Alfen N. Diagnostic value of muscle ultrasound for myopathies and myositis. *Curr Rheumatol Rep* (2020) **22**:82. doi:10.1007/s11926-020-00947-y

20. Mele A, Mantuano P, Boccanegra B, Conte E, Liantonio A, De Luca A. Preclinical ultrasonography in rodent models of neuromuscular disorders: the state of the art for diagnostic and therapeutic applications. *Int J Mol Sci* (2023) **24**(5):4976. doi:10.3390/ijms24054976

21. Talbot J, Maves L. Skeletal muscle fiber type: using insights from muscle developmental biology to dissect targets for susceptibility and resistance to muscle disease. *WIREs Dev Biol* (2016) **5**:518–34. doi:10.1002/wdev.230

22. Gillies AR, Lieber RL. Structure and function of the skeletal muscle extracellular matrix. *Muscle Nerve* (2011) **44**:318–31. doi:10.1002/mus.22094

23. Zullo A, Fleckenstein J, Schleip R, Hoppe K, Wearing S, Klingler W. Structural and functional changes in the coupling of fascial tissue, skeletal muscle, and nerves during aging. *Front Physiol* (2020) **11**:592. doi:10.3389/fphys.2020.00592

24. Vejsada R, Hník P. Radicular innervation of hindlimb muscles of the rat. *Physiol Bohemoslov* (1980) **29**:385–92.

25. Ranjbar K, Fayazi B. Vascularisation of skeletal muscle. Muscle cells - recent advances and future perspectives. In: Valarmathi MT, editor. *Muscle cells*. IntechOpen (2019). doi:10.5772/intechopen.85903

26. Kawai T. Shear wave elastography for chronic musculoskeletal problem. In: *Elastography-Dana stoian and alina popescu*. IntechOpen (2022). doi:10.5772/intechopen.102024

27. Dambrosio F, Amy D, Colombo A. B-mode color sonographic images in obstetrics and gynecology: preliminary report. *Ultrasound Obstet Gynecol* (1995) **6**:208–15. doi:10.1046/j.1469-0705.1995.06030208.x

28. Brockmann K, Becker P, Schreiber G, Neubert K, Brunner E, Bönnemann C. Sensitivity and specificity of qualitative muscle ultrasound in assessment of suspected neuromuscular disease in childhood. *Neuromuscul Disord* (2007) **17**:517–23. doi:10.1016/j.nmd.2007.03.015

29. Zaidman CM, Connolly AM, Malkus EC, Florence JM, Pestronk A. Quantitative ultrasound using backscatter analysis in Duchenne and Becker muscular dystrophy. *Neuromuscul Disord* (2010) **20**:805–9. doi:10.1016/j.nmd.2010.06.019

30. Aydınlı N, Baslo B, Çalışkan M, Ertaş M, Özmen M. Muscle ultrasonography and electromyography correlation for evaluation of floppy infants. *Brain Dev* (2003) **25**:22–4. doi:10.1016/s0387-7604(02)00119-5

31. Verbeek RJ, van der Hoeven JH, Sollie KM, Maurits NM, Bos AF, den Dunnen WFA, et al. Muscle ultrasound density in human fetuses with spina bifida aperta. *Early Hum Dev* (2009) **85**:519–23. doi:10.1016/j.earlhumdev.2009.04.008

32. Guilford JP. *Fundamental statistics in psychology and education*. New York: McGraw-Hill (1965).

33. Tanabe T, Otani H, Bao L, Mikami Y, Yasukura T, Ninomiya T, et al. Intracellular signaling pathway of substance P-induced superoxide production in human neutrophils. *Eur J Pharmacol* (1996) **299**:187–95. doi:10.1016/0014-2999(95)00816-0

34. Eilers W, Jaspers RT, de Haan A, Ferrié C, Valdivieso P, Flück M. CaMKII content affects contractile, but not mitochondrial, characteristics in regenerating skeletal muscle. *BMC Physiol* (2014) **14**:7. doi:10.1186/s12899-014-0007-z

35. Steinhoff M, Vergnolle N, Young SH, Tognetto M, Amadesi S, Ennes HS, et al. Agonists of proteinase-activated receptor 2 induce inflammation by a neurogenic mechanism. *Nat Med* (2000) **6**:151–8. doi:10.1038/72247

36. Vergnolle N, Ferazzini M, D'Andrea MR, Buddenkotte J, Steinhoff M. Proteinase-activated receptors: novel signals for peripheral nerves. *Trends Neurosciences* (2003) **26**:496–500. doi:10.1016/s0166-2236(03)00208-x

37. Mittal GA, Wadhwani R, Shroff M, Sukthankar R, Pathan E, Joshi VR. Ultrasonography in the diagnosis and follow-up of idiopathic inflammatory myopathies--a preliminary study. *J Assoc Physicians India* (2003) **51**:252–6.

38. Frara N, Fisher PW, Zhao Y, Tarr JT, Amin M, Popoff SN, et al. Substance P increases CCN2 dependent on TGF-beta yet Collagen Type I via TGF-beta1 dependent and independent pathways in tenocytes. *Connect Tissue Res* (2018) **59**:30–44. doi:10.1080/03008207.2017.1297809

EBM Experimental Biology and Medicine

TYPE Original Research
PUBLISHED 31 January 2024
DOI 10.3389/ebm.2024.10021

OPEN ACCESS

*CORRESPONDENCE
Farzin Farzaneh,
farzin.farzaneh@kcl.ac.uk

†Deceased

‡These authors have contributed equally to this work

RECEIVED 05 October 2023
ACCEPTED 04 January 2024
PUBLISHED 31 January 2024

CITATION
Zareian N, Eremin O, Pandha H, Baird R, Kwatra V, Funingana G, Verma C, Choy D, Hargreaves S, Moghimi P, Shepherd A, Lobo DN, Eremin J, Farzaneh F, Kordasti S and Spicer J (2024), A phase 1 trial of human telomerase reverse transcriptase (hTERT) vaccination combined with therapeutic strategies to control immune-suppressor mechanisms. *Exp. Biol. Med.* 249:10021. doi: 10.3389/ebm.2024.10021

A phase 1 trial of human telomerase reverse transcriptase (hTERT) vaccination combined with therapeutic strategies to control immune-suppressor mechanisms

Nahid Zareian[1], Oleg Eremin[2†], Hardev Pandha[3], Richard Baird[4], Vineet Kwatra[1], Gabriel Funingana[4], Chandan Verma[2], Desmond Choy[1], Steven Hargreaves[5], Pejvak Moghimi[6], Adrian Shepherd[6], Dileep N. Lobo[2,7], Jennifer Eremin[2], Farzin Farzaneh[1*], Shahram Kordasti[1‡] and James Spicer[1‡]

[1]School of Cancer and Pharmaceutical Sciences, King's College London, London, United Kingdom, [2]Nottingham Digestive Diseases Centre, NIHR Nottingham Biomedical Research Centre, Queen's Medical Centre, Nottingham University Hospitals NHS Trust and University of Nottingham, Nottingham, United Kingdom, [3]Department of Microbiology and Cellular Sciences, University of Surrey, Guildford, United Kingdom, [4]Cancer Research UK Cambridge Centre, Cambridge, United Kingdom, [5]Research Department of Pathology, UCL Cancer Institute, Faculty of Medical Sciences, University College London (UCL), London, United Kingdom, [6]The Institute of Structural and Molecular Biology (ISMB), Birkbeck, University of London, London, United Kingdom, [7]MRC Versus Arthritis Centre for Musculoskeletal Ageing Research, Queen's Medical Centre, School of Life Sciences, University of Nottingham, Nottingham, United Kingdom

Abstract

The presence of inhibitory immune cells and difficulty in generating activated effector T cells remain obstacles to development of effective cancer vaccines. We designed a vaccine regimen combining human telomerase reverse transcriptase (hTERT) peptides with concomitant therapies targeting regulatory T cells (Tregs) and cyclooxygenase-2 (COX2)-mediated immunosuppression. This Phase 1 trial combined an hTERT-derived 7-peptide library, selected to ensure presentation by both HLA class-I and class-II in 90% of patients, with oral low-dose cyclophosphamide (to modulate Tregs) and the COX2 inhibitor celecoxib. Adjuvants were Montanide and topical TLR-7 agonist, to optimise antigen presentation. The primary objective was determination of the safety and tolerability of this combination therapy, with anti-cancer activity, immune response and detection of antigen-specific T cells as additional endpoints. Twenty-nine patients with advanced solid tumours were treated. All were multiply-pretreated, and the majority had either colorectal or prostate cancer. The most common adverse events were injection-site reactions, fatigue and nausea. Median progression-free survival was 9 weeks, with no complete or partial responses, but 24% remained progression-free for ≥6 months. Immunophenotyping showed post-vaccination expansion of $CD4^+$ and

CD8⁺ T cells with effector phenotypes. The *in vitro* re-challenge of T cells with hTERT peptides, TCR sequencing, and TCR similarity index analysis demonstrated the expansion following vaccination of oligoclonal T cells with specificity for hTERT. However, a population of exhausted PD-1⁺ cytotoxic T cells was also expanded in vaccinated patients. This vaccine combination regimen was safe and associated with antigen-specific immunological responses. Clinical activity could be improved in future by combination with anti-PD1 checkpoint inhibition to address the emergence of an exhausted T cell population.

KEYWORDS

hTERT, vaccination, TLR agonist, phase-1 trial, CD8⁺ T-cells

Impact statement

Difficulty in generating activated effector T cells and the presence of inhibitory immune cells are obstacles to development of tumour vaccines. hTERT is overexpressed in >90% of malignancies. We conducted a Phase 1 trial, in which patients with different multiply-pretreated solid tumours were vaccinated with an hTERT-derived 7-peptide library, with a novel adjuvant strategy, selected to ensure presentation by both HLA class-I and class-II in 90% of a European population. Adjuvants were Montanide and topical TLR-7 agonist, to optimise antigen presentation. Oral low-dose cyclophosphamide, to modulate regulatory T cells, was combined with celecoxib to block cyclooxygenase-2-mediated immunosuppression. The primary objective was determination of vaccine/adjuvant safety and tolerability, with immune response and detection of antigen-specific T cells as exploratory endpoints. This vaccine was safe. The data demonstrates the induction of immunological responses, including clonal expansion of hTERT reactive T cells and clinical disease stabilisation for over 6 months in a quarter of these therapy-resistant patients.

Introduction

Immune therapy of cancer using vaccination strategies has had limited success to date, due to low immunogenicity of selected antigens, poor stimulation of effector T cells, and incomplete tumour specificity. Human telomerase reverse transcriptase (hTERT) is expressed at elevated levels in >90% of human tumours [1–3], and offers a potential target for active vaccination mediated immune therapy of cancer. Recognition of hTERT peptides by αβ T cells is HLA-restricted, requiring the selection of subsets of patients with specific HLA haplotypes (e.g., HLA-A2) in previous hTERT vaccination studies. In order to maximise eligibility for vaccination, we chose to use an hTERT peptide library compatible with multiple HLA haplotypes. This library was predicted to be suitable for direct presentation by at least one HLA class-I and one HLA class-II allele in over 90% of a European population [4–6]. The uptake and processing of long peptides, which involves the active uptake, processing and presentation of such peptides by the professional antigen presenting cells, require no HLA-selection [7]. No long peptides were included in our hTERT library.

The selected hTERT library consisted of seven peptides identified as immunogenic self-antigens that are predicted to bind directly, without intracellular processing, to common HLA proteins (4 to class I and 3 to class II) [8–12]. These were subsequently confirmed to have a high binding affinity to the predicted HLAs.[1] We also used a novel adjuvant strategy. Adjuvants employed were Montanide (ISA-51 VG), a water-in-oil emulsion composed of a mineral oil and a mannide mono-oleate surfactant, injected intradermally with the peptide library. In addition, imiquimod, an agonist for toll-like receptor 7 (TLR-7) was applied topically, in order to stimulate innate and acquired immune responses [13]. Each 3-weekly dose of vaccine was preceded by oral low dose cyclophosphamide (50 mg twice daily for the first 10 days of each cycle), in order to reduce immune suppressive regulatory T cells (Tregs) and myeloid derived suppressor cells (MDSCs) [14–17]. A cohort of 15 patients also received celecoxib, to inhibit cyclooxygenase-2 (COX-2), with the intention of suppressing pro-tumourigenic prostaglandin levels. This trial is the first step in a strategy termed "Combined Adjuvants for Synergistic Activation of Cellular immunity" (CASAC) [18, 19].

The aim of this study was to investigate the safety of this vaccine, and also to assess whether it could induce an antigen-specific cell-mediated immune response in a cohort of patients with advanced, therapy resistant solid tumours. Multi-dimensional immunophenotyping and T cell receptor (TCR) sequencing analysis were used to assess the specificity and magnitude of post-vaccination immunological responses.

1 http://www.syfpeithi.de/

Materials and methods

Trial design

We conducted a Phase 1 clinical trial in patients with advanced metastatic solid tumours for whom further standard therapy was unavailable or not suitable. This was an open label, fixed dose trial (see trial flow chart, Supplementary Figure S1). The primary objective of the study was to assess the safety and tolerability of the vaccine and associated therapy. Secondary objectives were to document vaccination-mediated stimulation of antigen-specific cellular immune responses (CD4+/CD8+ T cell), and to assess any clinical evidence of anti-tumour activity. The trial was approved by the Medicines and Healthcare products Regulatory Agency (EudraCT Number 2014-003025-18). Patients were recruited and treated at three UK cancer centres.

Patients

Eligible patients were aged ≥16, had histologically proven solid cancer, prior anti-cancer treatment completed ≥4 weeks previously, with no further suitable anti-cancer therapy option being available, and with a WHO performance status ≤2. Excluded comorbidities were autoimmune disorders, ongoing immune-suppressive therapy including steroids, central nervous system malignancies (primary and secondary), coronary artery disease, other major cardiac disease (documented left ventricular ejection fraction <50%), poorly controlled hypertension (diastolic >100 mmHg), and requirement for anticoagulation.

Trial treatment

Patients received 10 days of oral cyclophosphamide (50 mg twice daily orally on days 1–10), followed by the hTERT peptide vaccination emulsified in the Montanide adjuvant delivered intradermally on day 15 of 3-weekly cycles, and topical imiquimod (Meda Pharmaceuticals, Stockholm, Sweden). Of the 29 patients recruited, 15 were allocated non-randomly to receive additional continuous daily oral celecoxib, provided there was no contra-indication to receiving non-steroidal anti-inflammatory drugs. Seven GMP grade peptides were synthesised (4 class-I hTERT peptides: designated p324/325, p611, p865, p973; and 3 class-II hTERT peptides: p672, p766, p1123; designation numbers signify amino acid residue in the full-length hTERT protein; American Peptide Company, Sunnyvale, CA, United States) and transferred to a GMP facility (Rayne Institute, King's College London), where peptides were formulated as a mixture at equimolar concentrations (10 μg/mL). The hTERT peptide sequences, frequency of HLA linkage (haplotype population prevalence), and their avidity scores (SYFPEITHI database for MHC-peptide-prediction, University of Tubingen, Germany[1]) are listed in Supplementary Figure S2. These hTERT peptides bind with high affinity to specific HLA molecules; the vaccine was designed to permit the presentation of at least one Class-I and one Class-II peptide by the HLAs present in >90% of patients.

Immediately prior to vaccination, the seven peptides in 1 mL phosphate buffered saline were thawed and emulsified at the bedside by mixing with 1 mL Montanide ISA-51 VG. The emulsion was injected intradermally (2 mL) at multiple sites, at each injection site with a volume of 0.1–0.2 mL, in a 5 cm × 5 cm area of the anterior abdominal wall. New vaccination sites were used for each subsequent cycle. Patients received up to 8 cycles of vaccination in the absence of tumour progression or intolerable toxicity. Patients considered to be benefiting from treatment were allowed to continue beyond eight cycles.

Patient evaluation

Patients were clinically assessed at baseline and every cycle for disease symptoms and treatment-related adverse events. This included analysis of blood samples for renal and liver function tests, full blood count and, where relevant, tumour markers. Serial CT scans performed every 3 cycles were used to evaluate measurable disease. A sub-set of patients underwent additional intradermal injections (100 μL) of peptide mixture only (without either Montanide adjuvant or imiquimod) in cycles 1, 3 and 6 to investigate delayed type hypersensitivity (DTH) responses. Peripheral blood samples were collected from patients prior to, during and post-vaccination, to characterise patients' cellular immune response to vaccination.

Immunophenotyping

Frozen peripheral blood mononuclear cells (PBMCs) were used for immunophenotyping [Supplementary Material (materials and methods)]. To assess the specificity of the response to vaccine peptides, cells obtained from HLA-A0201 patients were challenged *in vitro* with the hTERT peptide library overnight, in the absence of any adjuvants but in the presence of protein transport inhibitor GolgiPlug (BD Biosciences, Erembodegem, Belgium). An irrelevant WT1-derived HLA-A0201-presented peptide 126–134 (RMFPNAPYL, referred to as RMF), served as a control. Cells were subsequently fixed, permeabilised, and stained with a selection of antibodies specific to T cells, regulatory T cells, T cell degranulation, T cell activation, immune check-points, T cell apoptosis markers and cytokines: CD3, CD8, CD4, CD45RO, CD127, CD25, CD107a, CD137, CD69, CD154, CD95, TCR Vd2g9, FoxP3, HLA-DR, CTLA-4, PD-1, TIM-3, IL-2, TNF-α and IFN-γ.

TABLE 1 Summary of patient characteristics.

Tumour (n = 29)	
Colorectal	12
Prostate	5
Lung	2
Pancreas	2
Breast	2
Oesophago-gastric	2
Cervix	1
Mesothelioma	1
Ovary	1
Renal	1
Age (median, rage)	62 (35–74)
Male	66%
Female	34%

Characteristics of twenty-nine patients with different solid tumour types that underwent vaccination.

TABLE 2 Treatment-related adverse events.

n (%)	Grade 1/2	Grade 3
*Injection site reaction	14 (45%)	
Fatigue	7 (23%)	
Nausea	5 (16%)	
Diarrhoea	3 (10%)	
Lymphocytopenia	3 (10%)	
ALP elevation	1 (3%)	1 (3%)
Anaemia	2 (6%)	
Anorexia	2 (6%)	
Weight loss	2 (6%)	

Adverse events reported as related to study medications in more than one patient.
No grade 4 events were observed.
ALP, alkaline phosphatase.
*Injection site reaction includes erythema, oedema, pruritis and discharge.

Ex vivo T cell stimulation assay

Patients' PBMCs were subjected to two weekly cycles of *ex vivo* stimulation in culture, in the presence of hTERT peptides at 70 μg/mL in X-Vivo 15 (Lonza, Bioscience) to allow more detailed immunopenotyping of antigen-specific lymphocyte populations. These cultures were supplemented with 5 ng/mL of interleukins (IL)-4 and -7 on the first and second day. The culture was maintained for 2 weeks with addition of fresh medium, containing 40 IU/mL IL-2 (Peprotech, London, United Kingdom), every second day. After 2 weeks, genomic DNA was extracted for TCR-β chain analysis by high-throughput sequencing.

TCR-β chain sequencing

DNA was extracted (Qiagen's DNeasy mini-columns, QIAGEN Inc., Germantown, MD, United States) from PBMC either without *in vitro* stimulation or after two rounds of hTERT peptide stimulation over 2 weeks. All TCR-β characterisation was performed by Adaptive Biotechnologies Corp (Seattle, WA, United States), using the ImmunoSEQ TCR-β human assay [Supplementary Material (materials and methods)].

Statistical analysis

The analyses of statistical significance of the differences between groups (pre- and post-vaccination) were performed using the Brown-Forsythe test. All other tests, unless otherwise indicated, were performed using the Student's t-test. A p-value ≤ 0.05 was considered statistically significant. For the statistical analysis of TCR-β chain similarity index, all Hamming distances were calculated for each of the pairwise patient-combinations [20]. The average and the standard deviation values for Hamming distances were calculated to generate standard error.

Results

Safety and anti-tumour activity

Twenty-nine patients with different solid tumour types underwent vaccination (Table 1). All patients had received prior systemic therapy, in many cases multiple lines of treatment; no further standard therapy was available or considered suitable. The study treatment was generally very well tolerated and almost all treatment-related adverse events were low grade (≤2). The most common events were injection site reactions, fatigue and nausea (Table 2). Erythema and limited cutaneous induration confined to the vaccinated area was commonly seen, usually maximal after 1 week and gradually fading thereafter. Two patients experienced a hypersensitivity reaction at the vaccination site with a much more marked area of localised oedema and overlying erythema, associated with pruritis. These patients were withdrawn from the study. No other treatment discontinuations due to treatment-related toxicity occurred. In the subset of patients who received intradermal injections of peptide only (without the Montanide adjuvant) no DTH responses were observed, so the injection site reactions were likely to be due to the use of adjuvant. There were no RECIST radiological or tumour marker responses. Seven

patients (24%) had disease that remained stable for at least 6 months after trial initiation.

Post-vaccination immune phenotyping of patient PBMCs (immune response to vaccine)

We first used screening with conventional flow cytometry, using a limited number of antibodies (CD3, CD8, CD107a, CD137, TNF-α, IFN-γ, and IL-2) to identify potential T cell responses following vaccination. Sufficient serial PBMC samples were obtained from 24 patients enrolled in the trial for immunophenotyping. We characterised changes in immune cell populations of un-challenged PBMCs from patients following vaccination. The proportions of both memory $CD4^+$ and $CD8^+$ T cells ($CD45RO^+$) were significantly higher in the post-vaccination samples ($p = 0.01$ and $p = 0.04$, respectively; data not shown).

We then re-challenged cells *ex vivo* with hTERT, or an irrelevant peptide as control. The proportions of both $CD4^+$ and $CD8^+$ cells expressing cytokines IL-2 ($p = 0.01$, $p = 0.02$), TNF-α ($p = 0.03/p = 0.02$) and IFN-γ ($p = 0.03/p = 0.02$) increased significantly compared to pre-vaccination levels in response to re-challenge with hTERT, but not in response to the irrelevant peptide.

Deep immunophenotyping analysis of unchallenged/challenged patient samples

To further analyse the phenotype of T cells following vaccination, with and without hTERT rechallenge, we used a multi-colour flowcytometer with the capacity to analyse 20 markers [using multidimensional flow cytometry with a panel of 17 markers (CD3, CD8, CD4, CD45RO, CD127, CD25, CD107a, CD137, CD69, CD154, CD95, TCR Vd2g9, FoxP3, HLA-DR, CTLA-4, PD-1, TIM-3, TNF-α, IFN-γ and IL-2)]. (BD FACSymphony™ flowcytometer), as well as an in-house automated clustering algorithm for analysis of multidimensional flowcytometry data[2] as described in Supplementary Material (Materials and Methods). Initially, various clusters of $CD8^+$ and $CD4^+$ T cells were identified in unchallenged samples by visualization of t-distributed stochastic neighbour embedding (viSNE).

We have then used downstream clustering methods to determine the detailed phenotypes of the expanded T cells post-vaccination in both the unchallenged state and following *in vitro* re-challenge of the PBMC, respectively. In the unchallenged PBMC, expanded $CD4^+$ T cells expressed significantly higher levels of activation markers after vaccination, including CD154 ($p = 0.01$), HLA-DR ($p = 0.006$), CD107a ($p = 0.005$) as well as the exhaustion marker PD1 ($p = 0.01$), and Fas marker CD95 ($p = 0.007$); exhausted $CD4^+$ T cells display reduced production of effector cytokines such as TNF-α and IFN-γ and increased Fas death markers (Figure 1).

Similarly, post-vaccination $CD8^+$ T cells expressed significantly higher levels of activation markers including CD154 ($p = 0.02$) and CD107a ($p = 0.008$), as well as Fas/CD95 ($p = 0.01$). While the number of Tregs was decreased post-vaccination ($CD4^+$, $CD25^{high}$, $CD27^{low}$), this decrease did not reach statistical significance (Figure 1C).

hTERT specificity of T cell response

After *in vitro* overnight stimulation with hTERT, or an irrelevant peptide as control, the proportions of both $CD4^+$ and $CD8^+$ T cells expressing cytokines IL-2 ($p = 0.01$, $p = 0.02$), TNF-α ($p = 0.03/p = 0.02$) and IFN-γ ($p = 0.03/p = 0.02$) increased significantly in response to re-challenge, compared to pre-vaccination levels (Figure 2), but not in response to the irrelevant peptide (Supplementary Figure S3). There were no changes in NK, γδ T cell or Treg populations following vaccination (Supplementary Figure S4).

To confirm these findings and to eliminate any bias, automated unsupervised clustering PhenoGraph was applied independently and it further confirmed these observations in both unchallenged (Figure 1B) and the *in vitro* re-challenged (Figure 2C) PBMC samples. Unsupervised clustering PhenoGraph has identified a cluster of cells, the phenotype of which has altered after vaccination. Subsequent statistical analysis of these cell clusters showed that the frequency of some of these cell clusters changed after vaccination. The most notable of these changes is a significant increase in the population of activated memory $CD8^+$ T cells in the unchallenged PBMCs (Figure 1B). A further overnight *in vitro* stimulation of the PBMCs with the hTERT peptides present in the VAPER vaccine identified additional populations of T cell subsets with significantly enhanced antigen-specific activation markers in both memory CD4 and CD8 T cells as presented in Figure 2. The re-challenged cells also expressed significantly higher cytokines TNF-α, IFN- γ and IL-2 after vaccination. In contrast with the phenotype of T cells exposed to hTERT peptides *ex vivo*, stimulation with the irrelevant peptide RMF did not result in $CD8^+$ or $CD4^+$ T cell expansion, nor was there an increase in T cell subsets displaying activation, memory or apoptotic markers in the post-vaccination samples (data not shown). This suggests that expansion after vaccination was substantially hTERT-specific.

2 Available at: https://github.com/kordastilab/cytoClustR

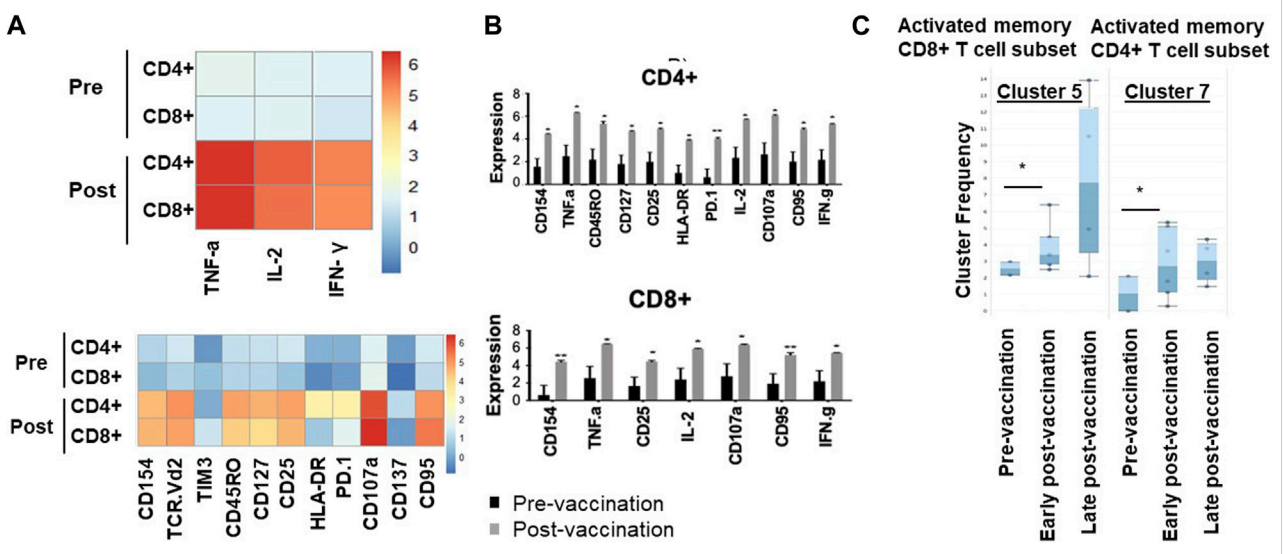

FIGURE 1
Memory and activated hTERT-responsive CD4⁺ and CD8⁺ T cells increase post-vaccination. **(A)** Median expression of the selected markers in pre- and post-vaccination PBMCs from 24 patients as identified by clustering algorithm CytoClustR on a subset of 400,000 cells proportionally selected from all samples. Each row represents a cell cluster and each column represents a marker. Heatmap plot generated from SPADE analysis. Expression values were transformed using the arcsin function in a cofactor of 5. The plot shows a difference in the immunological signature between pre- and post-vaccination T lymphocytes, a phenotype that shows increased presence of memory (CD45RO) activated (CD107a, HLA.DR) $CD8^+$ T cells. These stimulated cells appear to express inhibitory co-receptors (PD-1, TIM3), as well as CD95 (APO-1/Fas), which are known to be increased in post-vaccination T cells. **(B,C)** Quantitation of T cell activation markers in different clusters of unstimulated cells, with significantly increasedexpression post-vaccination in a cluster (cluster 5) $CD8^{hi}$, $HLADR^{hi}$, $PD\text{-}1^{hi}$, $CTLA4^{hi}$, $TIM\text{-}3^{hi}$ $CD45RO^{hi}$, $CD95^{hi}$, $CD107a^{hi}$, $CD137^{hi}$. Error bars are standard error of mean. Two-way Anova analysis of variance test was used for statistical analysis. $*p < 0.05$.

The antigen specificity of expanded T cells

TCR Vβ CDR3 sequencing of patients' T cells was performed, pre- and post-vaccination, to assess the antigen-specificity of responses to vaccination. Six patients with maintained stable disease (SD) and two with early disease progression (PD) were selected for study. TCR-β sequence analysis of PBMC DNA revealed the emergence of oligoclonal populations of T cells after hTERT vaccination in both SD and PD patients. The 20 most prevalent clones are presented in Figure 3A and Supplementary Figure S5A.

To investigate the specificity of TCR clones, TCR-β clonality was also analysed after two rounds of *ex vivo* stimulation with hTERT peptides over 2 weeks, in the absence of any adjuvants. This data showed further hTERT-driven expansion of a subset of the oligoclonal T cells which was predominantly evident in patients with maintained stable disease (median: 6.9%; range: 1.1%–23%) compared to patients with progressive disease (3.1%), providing evidence for hTERT specificity of a subset of the clonally expanded T cells (Figure 3B; Supplementary Figure S5B). We then examined TCR similarity, among the T cell clones that had increased in frequency after *in vitro* hTERT stimulation, by calculating the pairwise Hamming distances across the CDR3 sequences of these clones, as a measure of the likelihood of two separate TCRs recognising the same HLA/antigen complex. The Hamming distances amongst CDR3 sequences in the top 20 hTERT-expanded T cell clones, i.e., the most prevalent clones were substantially shorter in the vaccinated patients who maintained stable disease (SD) compared with patients who had developed a progressive disease. These results provide a strong indication of similarity between different TCR clones in the group with SD, and further support for hTERT-specificity of oligoclonally expanded T cells appearing after vaccination (Figure 3C).

Discussion

hTERT is overexpressed in >90% of cancer cells but not in normal tissues, apart from stem cells and mitotically active normal cell populations [1–3, 21–27]; therefore representing an attractive tumour antigen target for therapeutic vaccination in a range of cancers [28]. hTERT peptides are naturally processed by tumour cells, and are presented in the context of HLA class-I and -II molecules [29]. Therapeutic hTERT peptide vaccination has been previously investigated in patients with cancer, and shown to be safe [30]. Clinical responses have been variable [31–33], but vaccination-induced stimulation of prominent specific T cell responses have been previously documented [9, 34–36], and hTERT peptides bind with high

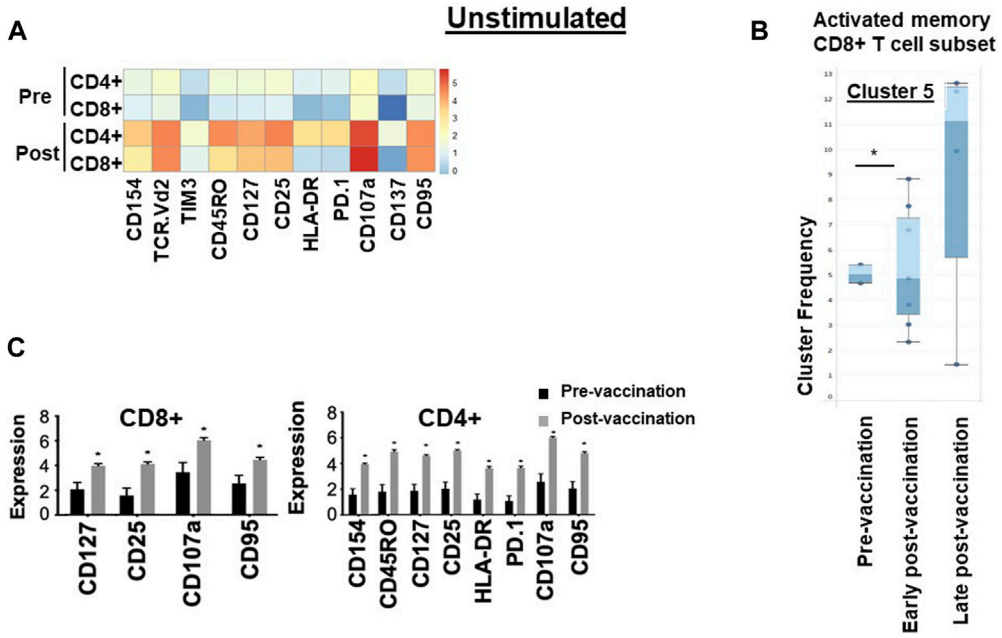

FIGURE 2
Immunological signature of PBMCs from patients in the VAPER study. **(A)** Median expression of the selected markers in pre- and post-vaccination PBMCs from 24 patients as identified by clustering algorithm CytoClustR on a subset of 400,000 cells proportionally selected from all samples. Each row represents a cell cluster and each column represents a marker. Heatmap plot generated from SPADE analysis. Expression values were transformed using the arcsin function in a cofactor of 5. The plot shows a difference in the immunological signature between pre- and post-vaccination T lymphocytes, a phenotype that shows increased presence of memory (CD45RO) activated (CD107a, HLA.DR) $CD8^+$ T cells. These stimulated cells appear to express inhibitory co-receptors (PD-1, TIM3), as well as CD95 (APO-1/Fas), which are known to be increased in post-vaccination T cells. **(B,C)** Quantitation of T cell activation markers in different clusters of stimulated cells, with significantly increased expression post-vaccination in two clusters of cells (cluster 5 and cluster 7).Cluster 5: $CD8^{hi}$, $HLADR^{hi}$, $PD\text{-}1^{hi}$, $CTLA4^{hi}$, $TIM\text{-}3^{hi}$ $TCRVD2^{hi}$ $CD45RO^{hi}$ $CD137^{hi}$ $CD107a^{hi}$, $IL\text{-}2^{hi}$, $TNF\text{-}a^{hi}$, Cluster 7: $CD4^{hi}$, $HLADR^{hi}$, $PD\text{-}1^{hi}$, $CTLA4^{hi}$, $TIM\text{-}3^{hi}$ $CD45RO^{hi}$ $CD107a^{hi}$, $IL\text{-}2^{hi}$Error bars are standard error of mean. Two-way Anova analysis of variance test was used for statistical analysis. $*p < 0.05$. The re-challenged cells showed a similar phenotype with unchallenged cells; in addition re-challenged cells also expressed significantly higher cytokines TNF-a, IFN-g and IL-2 after vaccination.

affinity to particular HLA haplotypes. However, class-I binding hTERT peptides used in previous trials have limited therapeutic applicability because of HLA haplotype heterogeneity in patients [4, 33, 37–39]. In this trial we have used a combination of peptides selected for high binding affinities to a number of commonly expressed HLA haplotypes. This strategy aimed to ensure that at least one component of the peptide library is likely to be effectively presented by the HLAs that are present in 90% of European patients. HLA haplotyping was not necessary to use this treatment; we selected a pool of seven hTERT peptides to ensure presentation by both HLA class-I and class-II in 90% of patients. For the future studies, a wider mixture of peptides that can be presented by different HLA classes, combined with suitable adjuvants, can possibly be used to cover a larger population of patients.

We applied the TLR-7 agonist imiquimod topically, with the aim of promoting antigen uptake by dendritic cells (DCs) and activation of the release of pro-inflammatory cytokines [40]. Stimulation of immature DCs with TLR agonists upregulates CCR7, increasing their migration to draining lymph nodes [41]. Animal models have shown that imiquimod can enhance dendritic cell survival, as well as promoting tumour–specific T cell priming, trafficking and accumulation in lymph nodes [42, 43]. Appropriately formulated adjuvants such as Montanide provide a depot for the prolonged release of antigens, preventing rapid degradation, and ensuring a continuous delivery of antigen to the regional lymph nodes. Trials using Montanide have demonstrated significant enhancement of T cell immune responses and improved clinical outcomes [44, 45]. Combination of hTERT peptides with Montanide has previously led to the induction of effective $CD8^+$ T cell responses [46]. Metronomic low dose cyclophosphamide depletes Tregs whilst preserving overall lymphocyte numbers [47], and augmented effector T cell responses are also reported [48–51].

The vaccination strategy developed here is safe, with hypersensitivity to the Montanide/peptide mix being the only adverse event warranting treatment discontinuation. There were no RECIST responses in this phase 1 trial conducted in patients with therapy-resistant, metastatic disease. Despite their advanced cancers, maintained stable disease for at least 6 months was observed in 24% of patients, with a range of tumour types (colorectal, lung, pancreas, prostate, breast, cervix, ovary, upper GI and pleural).

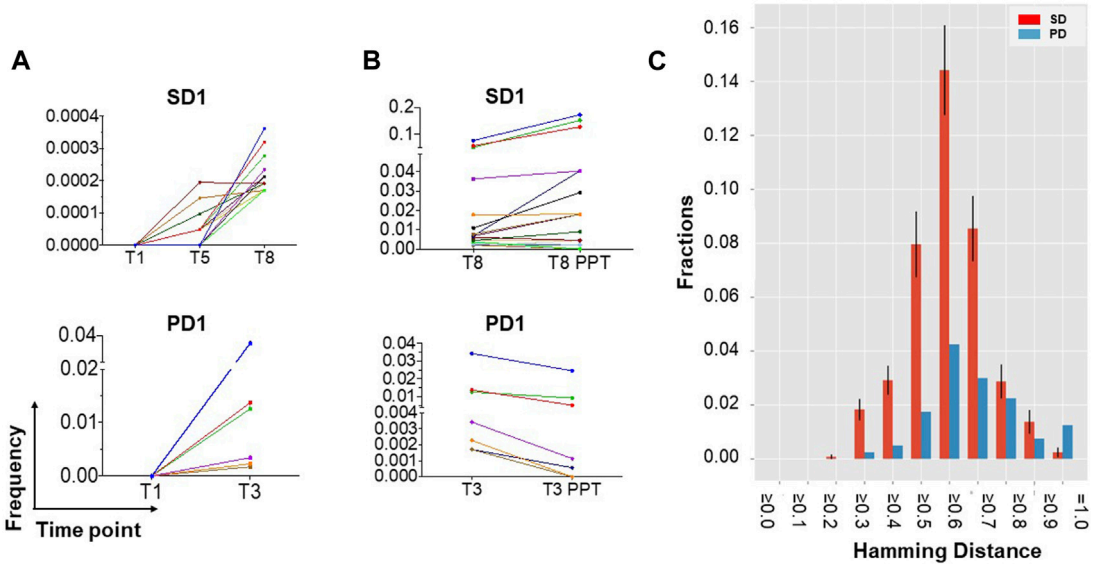

FIGURE 3
TCR-β sequencing identifies the emergence of new clonal populations of T cells after hTERT vaccination. **(A)** New clonal populations of T cells emerge after vaccination in patients with both maintained stable disease (SD) and disease progression (PD). DNA was extracted from fresh frozen PBMCs collected prior to and after vaccination and analysed for TCR-β oligoclonality. TCR sequence analysis identifies the emergence of oligoclonal populations of T cells at the frequencies indicated, the 20 most prevalent of which are presented for 1 patient each with SD or with PD, representative of a total of 6 SD and 2 PD patients analyzed. Time points are indicated in weeks from starting vaccination (for example, T8 = week 8). **(B)** Evidence for hTERT specificity among expanded T cells clones. TCR-β oligoclonality was further analysed following 2 weeks of *ex vivo* stimulation with hTERT peptides, in order to assess T cell specificity for hTERT. hTERT-driven expansion of a subset of the oligoclonal T cells is most evident in patients with maintained SD rather than PD. **(C)** Sequence similarity analysis (distance score by Hamming metric) supports true hTERT specificity of T cell clones responding to *ex vivo* culture with hTERT peptide. The Hamming distance (HD) amongst the peptide sequences encoded by the CDR3 region of TCR-β was measured in the 20 most prevalent clones of T cells that had expanded after *in vitro* stimulation with hTERT. Samples from six patients with stable disease (SD; red bars) are compared with those from two with more rapidly progressing disease (PD; blue bars). Mean and standard deviation values for HD are shown ≥ the corresponding x-axis value. Error bars are calculated only for the SD group, which includes more than one inter-patient pairwise comparison. HD is scaled between zero (identity) and one (no similarity). The left-skewness of the PD group distribution and higher fractions of lower HD values for the SD group indicates a strong convergence at the sequence level for patients with SD, and therefore a higher similarity in the MHC antigen targets recognized by the oligoclonally expanded T cells, compared to the PD group.

Strong $CD4^+$ and $CD8^+$ T cell responses were evident following vaccination with this hTERT peptide mixture. Using an unbiased clustering method, we show that these expanded T cells have an activated phenotype but that they also express markers of exhaustion and apoptosis. This data suggests that combining hTERT vaccination with immune checkpoint blockade may further improve the magnitude and longevity of the overall immune response. Interestingly, we did not find a significant change in the frequency or phenotype of other immune cell populations such as NK cells, γδ T cells or Tregs after vaccination. A numerical reduction in Tregs did not reach statistical significance, possibly due to small sample size.

The expanded T cells showed far less sequence diversity in their CDR3 region as evident by the number of expanded clones post-vaccination. The dominant clones were further expanded following *in vitro* rechallenge with hTERT peptides but not the irrelevant peptide, indicating the hTERT-specificity of the clonally expanded T cells. However, considering the variety of HLA haplotype in these patients, finding similar CDR3 sequences to confirm that T cells from different patients share specificity is challenging. To overcome this issue, we calculated the Hamming-distance similarity index For the largest expanded clones as a proxy for convergence. Sequence convergence indicates sequence similarity between the CDR3 regions of different oligoclonally expanded T cell populations, supporting the conclusion that the expanded T cell clones from different patients have been selected to detect the same HLA-peptide complexes.

This trial is a first step in the clinical development of a cancer vaccine using a strategy that has been termed "Combined Adjuvants for Synergistic Activation of Cellular immunity" (CASAC) [18, 19]. Our pharmacodynamic data indicates that this vaccination strategy induces immunological responses against a tumour-associated self-antigen, hTERT. Specifically, we have demonstrated that hTERT peptide vaccination, in combination with adjuvants and metronomic cyclophosphamide therapy, can generate activated hTERT-specific CD4+/CD8+ T effector responses against this tumour associated antigen in cancer patients with therapy-resistant solid tumours. However, the best clinical responses seen in this trial were prolonged stable disease, and no tumour shrinkage by RECIST criteria occurred, possibly because of persistent

PD1-positive Tregs. Future combination of this vaccination strategy with PD-1/PD-L1-targeted immune checkpoint inhibition may improve clinical efficacy, as has been observed in other pairings of vaccination with checkpoint inhibitors [52–56].

Conclusion

We conclude that this vaccine combination is associated with antigen-specific immunological responses and can generate activated hTERT-specific CD4+/CD8+ effector responses against this tumour associated antigen in patients with therapy-resistant solid tumours. Clinical response could be improved by combination with anti-PD1 checkpoint inhibition to address the emergence of an exhausted T cell population.

Author contributions

OE, JS, FF, SK, JE, and DL conceived and supervised the study and wrote the manuscript. NZ performed and designed experiments, analysed the results, and wrote the manuscript. DC and SH performed the computations and analytic calculations. JS, HP, RB, VK, and GF recruited patients, delivered the clinical protocol and wrote the manuscript. CV performed sample preparation. PM and AS performed TCR similarity index analysis. All authors contributed to the article and approved the submitted version. This work is dedicated to the memory of late OE.

Author disclaimer

The views expressed are those of the authors and not necessarily those of the NIHR or the Department of Health and Social Care.

Data availability statement

The datasets presented in this study can be found in online repositories. The names of the repository/repositories and accession number(s) can be found in the article/Supplementary Material.

Ethics statement

The studies involving humans were approved by the Research Ethics Committees of The United Kingdom. The studies were conducted in accordance with the local legislation and institutional requirements. The participants provided their written informed consent to participate in this study.

Funding

The trial was funded by the Candles Charity [Grant Number 1125834] and sponsored by King's Health Partners. The authors acknowledge additional financial support from the UK Department of Health and Cancer Research UK via Experimental Cancer Medicine Centre grants to King's Health Partners and the University of Cambridge/Addenbrooke's Hospital. These centres also hold National Institute for Health Research Biomedical Research Centre (BRC) awards. In Cambridge [Grant Number #BRC-1215-20014] also supports the Cambridge Clinical Research Centre where study participants were seen. We acknowledge the BRC Immune Monitoring Core Facility team at Guy's and St Thomas' NHS Foundation Trust [Grant Number IS-BRC-1215-20006] for flow cytometry facilities and assistance, and the Cancer Research UK King's Health Partners Centre at King's College London [Grant Number C604/A25135].

Conflict of interest

The authors declare that the research was conducted in the absence of any commercial or financial relationships that could be construed as a potential conflict of interest.

Supplementary material

The Supplementary Material for this article can be found online at: https://www.ebm-journal.org/articles/10.3389/ebm.2024.10021/full#supplementary-material

References

1. Kim NW. Clinical implications of telomerase in cancer. *Eur J Cancer* (1997) **33**(5):781–6. doi:10.1016/s0959-8049(97)00057-9

2. Kim NW, Piatyszek MA, Prowse KR, Harley CB, West MD, Ho PLC, et al. Specific association of human telomerase activity with immortal cells and cancer. *Science* (1994) **266**(5193):2011–5. doi:10.1126/science.7605428

3. Shay JW, Wright WE. The reactivation of telomerase activity in cancer progression. *Trends Genet* (1996) **12**(4):129–31. doi:10.1016/0168-9525(96)30018-8

4. Lilleby W, Gaudernack G, Brunsvig PF, Vlatkovic L, Schulz M, Mills K, et al. Phase I/IIa clinical trial of a novel hTERT peptide vaccine in men with metastatic hormone-naive prostate cancer. *Cancer Immunol Immunother* (2017) **66**(7): 891–901. doi:10.1007/s00262-017-1994-y

5. Mizukoshi E, Nakagawa H, Kitahara M, Yamashita T, Arai K, Sunagozaka H, et al. Immunological features of T cells induced by human telomerase reverse transcriptase-derived peptides in patients with hepatocellular carcinoma. *Cancer Lett* (2015) **364**(2):98–105. doi:10.1016/j.canlet.2015.04.031

6. Mehrotra S, Britten CD, Chin S, Garrett-Mayer E, Cloud CA, Li M, et al. Vaccination with poly(IC:LC) and peptide-pulsed autologous dendritic cells in patients with pancreatic cancer. *J Hematol Oncol* (2017) **10**(1):82. doi:10.1186/s13045-017-0459-2

7. Bijker MS, van den Eeden SJF, Franken KL, Melief CJM, Offringa R, van der Burg SH. CD8+ CTL priming by exact peptide epitopes in incomplete Freund's adjuvant induces a vanishing CTL response, whereas long peptides induce sustained CTL reactivity. *J Immunol* (2007) **179**(8):5033–40. doi:10.4049/jimmunol.179.8.5033

8. Schroers R, Huang XF, Hammer J, Zhang J, Chen SY. Identification of HLA DR7-restricted epitopes from human telomerase reverse transcriptase recognized by CD4+ T-helper cells. *Cancer Res* (2002) **62**(9):2600–5.

9. Minev B, Hipp J, Firat H, Schmidt JD, Langlade-Demoyen P, Zanetti M. Cytotoxic T cell immunity against telomerase reverse transcriptase in humans. *Proc Natl Acad Sci U S A* (2000) **97**(9):4796–801. doi:10.1073/pnas.070560797

10. Vonderheide RH, Anderson KS, Hahn WC, Butler MO, Schultze JL, Nadler LM. Characterization of HLA-A3-restricted cytotoxic T lymphocytes reactive against the widely expressed tumor antigen telomerase. *Clin Cancer Res* (2001) **7**(11):3343–8.

11. Cortez-Gonzalez X, Sidney J, Adotevi O, Sette A, Millard F, Lemonnier F, et al. Immunogenic HLA-B7-restricted peptides of hTRT. *Int Immunol* (2006) **18**(12):1707–18. doi:10.1093/intimm/dxl105

12. Bernardeau K, Kerzhero J, Fortun A, Moreau-Aubry A, Favry E, Echasserieau K, et al. A simple competitive assay to determine peptide affinity for HLA class II molecules: a useful tool for epitope prediction. *J Immunological Methods* (2011) **371**(1-2):97–105. doi:10.1016/j.jim.2011.06.018

13. Goldinger SM, Dummer R, Baumgaertner P, Mihic-Probst D, Schwarz K, Hammann-Haenni A, et al. Nano-particle vaccination combined with TLR-7 and -9 ligands triggers memory and effector CD8(+) T-cell responses in melanoma patients. *Eur J Immunol* (2012) **42**(11):3049–61. doi:10.1002/eji.201142361

14. Veltman JD, Lambers MEH, van Nimwegen M, de Jong S, Hendriks RW, Hoogsteden HC, et al. Low-dose cyclophosphamide synergizes with dendritic cell-based immunotherapy in antitumor activity. *J Biomed Biotechnol* (2010) **2010**:1–10. doi:10.1155/2010/798467

15. Greten TF, Ormandy LA, Fikuart A, Höchst B, Henschen S, Hörning M, et al. Low-dose cyclophosphamide treatment impairs regulatory T cells and unmasks AFP-specific CD4+ T-cell responses in patients with advanced HCC. *J Immunother* (2010) **33**(2):211–8. doi:10.1097/cji.0b013e3181bb499f

16. Fontana A, Bocci G, Galli L, D'Arcangelo M, Derosa L, Fioravanti A, et al. Metronomic cyclophosphamide in elderly patients with advanced, castration-resistant prostate cancer. *J Am Geriatr Soc* (2010) **58**(5):986–8. doi:10.1111/j.1532-5415.2010.02833.x

17. Sevko A, Sade-Feldman M, Kanterman J, Michels T, Falk CS, Umansky L, et al. Cyclophosphamide promotes chronic inflammation-dependent immunosuppression and prevents antitumor response in melanoma. *J Invest Dermatol* (2013) **133**(6):1610–9. doi:10.1038/jid.2012.444

18. Tye GJ, Ioannou K, Amofah E, Quartey-Papafio R, Westrop SJ, Krishnamurthy P, et al. The combined molecular adjuvant CASAC enhances the CD8+ T cell response to a tumor-associated self-antigen in aged, immunosenescent mice. *Immun Ageing* (2015) **12**:6. doi:10.1186/s12979-015-0033-0

19. Wells JW, Cowled CJ, Farzaneh F, Noble A. Combined triggering of dendritic cell receptors results in synergistic activation and potent cytotoxic immunity. *J Immunol* (2008) **181**(5):3422–31. doi:10.4049/jimmunol.181.5.3422

20. MacKay DJC. *Information theory, inference, and learning algorithms*. Cambridge, UK; New York: Cambridge University Press xii (2003). p. 628.

21. Nakamura TM, Morin GB, Chapman KB, Weinrich SL, Andrews WH, Lingner J, et al. Telomerase catalytic subunit homologs from fission yeast and human. *Science* (1997) **277**(5328):955–9. doi:10.1126/science.277.5328.955

22. Shay JW, Gazdar AF. Telomerase in the early detection of cancer. *J Clin Pathol* (1997) **50**(2):106–9. doi:10.1136/jcp.50.2.106

23. Umbricht CB, Sherman ME, Dome J, Carey LA, Marks J, Kim N, et al. Telomerase activity in ductal carcinoma *in situ* and invasive breast cancer. *Oncogene* (1999) **18**(22):3407–14. doi:10.1038/sj.onc.1202714

24. Ahmed A, Tollefsbol TO. Telomerase, telomerase inhibition, and cancer. *J Anti-Aging Med* (2003) **6**(4):315–25. doi:10.1089/109454503323028911

25. Castelo-Branco P, Choufani S, Mack S, Gallagher D, Zhang C, Lipman T, et al. Methylation of the TERT promoter and risk stratification of childhood brain tumours: an integrative genomic and molecular study. *Lancet Oncol* (2013) **14**(6):534–42. doi:10.1016/s1470-2045(13)70110-4

26. Koziel JE, Fox MJ, Steding CE, Sprouse AA, Herbert BS. Medical genetics and epigenetics of telomerase. *J Cell Mol Med* (2011) **15**(3):457–67. doi:10.1111/j.1582-4934.2011.01276.x

27. Ramakrishnan S, Eppenberger U, Mueller H, Shinkai Y, Narayanan R. Expression profile of the putative catalytic subunit of the telomerase gene. *Cancer Res* (1998) **58**(4):622–5.

28. Vonderheide RH. Prospects and challenges of building a cancer vaccine targeting telomerase. *Biochimie* (2008) **90**(1):173–80. doi:10.1016/j.biochi.2007.07.005

29. Inderberg-Suso EM, Trachsel S, Lislerud K, Rasmussen AM, Gaudernack G. Widespread CD4+ T-cell reactivity to novel hTERT epitopes following vaccination of cancer patients with a single hTERT peptide GV1001. *Oncoimmunology* (2012) **1**(5):670–86. doi:10.4161/onci.20426

30. Brunsvig PF, Aamdal S, Gjertsen MK, Kvalheim G, Markowski-Grimsrud CJ, Sve I, et al. Telomerase peptide vaccination: a phase I/II study in patients with non-small cell lung cancer. *Cancer Immunol Immunother* (2006) **55**(12):1553–64. doi:10.1007/s00262-006-0145-7

31. Bernhardt SL, Gjertsen MK, Trachsel S, Møller M, Eriksen JA, Meo M, et al. Telomerase peptide vaccination of patients with non-resectable pancreatic cancer: a dose escalating phase I/II study. *Br J Cancer* (2006) **95**(11):1474–82. doi:10.1038/sj.bjc.6603437

32. Vetsika EK, Konsolakis G, Aggouraki D, Kotsakis A, Papadimitraki E, Christou S, et al. Immunological responses in cancer patients after vaccination with the therapeutic telomerase-specific vaccine Vx-001. *Cancer Immunol Immunother* (2012) **61**(2):157–68. doi:10.1007/s00262-011-1093-4

33. Bolonaki I, Kotsakis A, Papadimitraki E, Aggouraki D, Konsolakis G, Vagia A, et al. Vaccination of patients with advanced non-small-cell lung cancer with an optimized cryptic human telomerase reverse transcriptase peptide. *J Clin Oncol* (2007) **25**(19):2727–34. doi:10.1200/jco.2006.10.3465

34. Arai J, Yasukawa M, Ohminami H, Kakimoto M, Hasegawa A, Fujita S. Identification of human telomerase reverse transcriptase-derived peptides that induce HLA-A24-restricted antileukemia cytotoxic T lymphocytes. *Blood* (2001) **97**(9):2903–7. doi:10.1182/blood.v97.9.2903

35. Vonderheide RH, Hahn WC, Schultze JL, Nadler LM. The telomerase catalytic subunit is a widely expressed tumor-associated antigen recognized by cytotoxic T lymphocytes. *Immunity* (1999) **10**(6):673–9. doi:10.1016/s1074-7613(00)80066-7

36. Aloysius MM, Mc Kechnie AJ, Robins RA, Verma C, Eremin JM, Farzaneh F, et al. Generation *in vivo* of peptide-specific cytotoxic T cells and presence of regulatory T cells during vaccination with hTERT (class I and II) peptide-pulsed DCs. *J Transl Med* (2009) **7**:18. doi:10.1186/1479-5876-7-18

37. Greten TF, Forner A, Korangy F, N'Kontchou G, Barget N, Ayuso C, et al. A phase II open label trial evaluating safety and efficacy of a telomerase peptide vaccination in patients with advanced hepatocellular carcinoma. *BMC Cancer* (2010) **10**:209. doi:10.1186/1471-2407-10-209

38. Kotsakis A, Papadimitraki E, Vetsika EK, Aggouraki D, Dermitzaki EK, Hatzidaki D, et al. A phase II trial evaluating the clinical and immunologic response of HLA-A2(+) non-small cell lung cancer patients vaccinated with an hTERT cryptic peptide. *Lung Cancer* (2014) **86**(1):59–66. doi:10.1016/j.lungcan.2014.07.018

39. Menez-Jamet J, Gallou C, Rougeot A, Kosmatopoulos K. Optimized tumor cryptic peptides: the basis for universal neo-antigen-like tumor vaccines. *Ann Transl Med* (2016) **4**(14):266. doi:10.21037/atm.2016.05.15

40. Shi M, Chen X, Ye K, Yao Y, Li Y. Application potential of toll-like receptors in cancer immunotherapy: systematic review. *Medicine (Baltimore)* (2016) **95**(25):e3951. doi:10.1097/md.0000000000003951

41. Gunn MD, Kyuwa S, Tam C, Kakiuchi T, Matsuzawa A, Williams LT, et al. Mice lacking expression of secondary lymphoid organ chemokine have defects in lymphocyte homing and dendritic cell localization. *J Exp Med* (1999) **189**(3):451–60. doi:10.1084/jem.189.3.451

42. Rechtsteiner G, Warger T, Osterloh P, Schild H, Radsak MP. Cutting edge: priming of CTL by transcutaneous peptide immunization with imiquimod. *J Immunol* (2005) **174**(5):2476–80. doi:10.4049/jimmunol.174.5.2476

43. Prins RM, Craft N, Bruhn KW, Khan-Farooqi H, Koya RC, Stripecke R, et al. The TLR-7 agonist, imiquimod, enhances dendritic cell survival and promotes tumor antigen-specific T cell priming: relation to central nervous system antitumor immunity. *J Immunol* (2006) **176**(1):157–64. doi:10.4049/jimmunol.176.1.157

44. Aucouturier J, Ascarateil S, Dupuis L. The use of oil adjuvants in therapeutic vaccines. *Vaccine* (2006) **24**(S2):44–5. doi:10.1016/j.vaccine.2005.01.116

45. Karbach J, Gnjatic S, Bender A, Neumann A, Weidmann E, Yuan J, et al. Tumor-reactive $CD8^+$ T-cell responses after vaccination with NY-ESO-1 peptide, CpG 7909 and Montanide® ISA-51: association with survival. *Int J Cancer* (2010) **126**(4):909–18. doi:10.1002/ijc.24850

46. Mavroudis D, Bolonakis I, Cornet S, Myllaki G, Kanellou P, Kotsakis A, et al. A phase I study of the optimized cryptic peptide TERT(572y) in patients with advanced malignancies. *Oncology* (2006) **70**(4):306–14. doi:10.1159/000096252

47. Ghiringhelli F, Menard C, Puig PE, Ladoire S, Roux S, Martin F, et al. Metronomic cyclophosphamide regimen selectively depletes CD4+CD25+ regulatory T cells and restores T and NK effector functions in end stage cancer patients. *Cancer Immunol Immunother* (2007) **56**(5):641–8. doi:10.1007/s00262-006-0225-8

48. Radojcic V, Bezak KB, Skarica M, Pletneva MA, Yoshimura K, Schulick RD, et al. Cyclophosphamide resets dendritic cell homeostasis and enhances antitumor immunity through effects that extend beyond regulatory T cell elimination. *Cancer Immunol Immunother* (2010) **59**(1):137–48. doi:10.1007/s00262-009-0734-3

49. Li Y, Lu W, Yang J, Edwards M, Jiang S. Survivin as a biological biomarker for diagnosis and therapy. *Expert Opin Biol Ther* (2021) **21**(11):1429–41. doi:10.1080/14712598.2021.1918672

50. Negrini S, De Palma R, Filaci G. Anti-cancer immunotherapies targeting telomerase. *Cancers (Basel)* (2020) **12**(8):2260. doi:10.3390/cancers12082260

51. Fenoglio D, Traverso P, Parodi A, Tomasello L, Negrini S, Kalli F, et al. A multi-peptide, dual-adjuvant telomerase vaccine (GX301) is highly immunogenic in patients with prostate and renal cancer. *Cancer Immunol Immunother* (2013) **62**(6):1041–52. doi:10.1007/s00262-013-1415-9

52. Curran MA, Glisson BS. New hope for therapeutic cancer vaccines in the era of immune checkpoint modulation. *Annu Rev Med* (2019) **70**:409–24. doi:10.1146/annurev-med-050217-121900

53. Chung V, Kos FJ, Hardwick N, Yuan Y, Chao J, Li D, et al. Evaluation of safety and efficacy of p53MVA vaccine combined with pembrolizumab in patients with advanced solid cancers. *Clin Transl Oncol* (2019) **21**(3):363–72. doi:10.1007/s12094-018-1932-2

54. Massarelli E, William W, Johnson F, Kies M, Ferrarotto R, Guo M, et al. Combining immune checkpoint blockade and tumor-specific vaccine for patients with incurable human papillomavirus 16-related cancer: a phase 2 clinical trial. *JAMA Oncol* (2019) **5**(1):67–73. doi:10.1001/jamaoncol.2018.4051

55. Weber JS, Kudchadkar RR, Yu B, Gallenstein D, Horak CE, Inzunza HD, et al. Safety, efficacy, and biomarkers of nivolumab with vaccine in ipilimumab-refractory or -naive melanoma. *J Clin Oncol* (2013) **31**(34):4311–8. doi:10.1200/jco.2013.51.4802

56. Gibney GT, Kudchadkar RR, DeConti RC, Thebeau MS, Czupryn MP, Tetteh L, et al. Safety, correlative markers, and clinical results of adjuvant nivolumab in combination with vaccine in resected high-risk metastatic melanoma. *Clin Cancer Res* (2015) **21**(4):712–20. doi:10.1158/1078-0432.ccr-14-2468

EBM Experimental Biology and Medicine

TYPE Original Research
PUBLISHED 29 February 2024
DOI 10.3389/ebm.2024.10108

OPEN ACCESS

*CORRESPONDENCE
Bing Xu,
xubing@xmu.edu.cn
Jingwei Yao,
381060985@qq.com
Li Zhang,
957837242@qq.com

†These authors have contributed equally to this work

RECEIVED 09 July 2023
ACCEPTED 25 September 2023
PUBLISHED 29 February 2024

CITATION
Chen Q, Hong Y, Chen W, Lin F, Zeng J, Huang Y, Zhang L, Yao J and Xu B (2024), Prognostic implications of cGAS and STING gene expression in acute myeloid leukemia.
Exp. Biol. Med. 249:10108.
doi: 10.3389/ebm.2024.10108

Prognostic implications of cGAS and STING gene expression in acute myeloid leukemia

Qiuling Chen[1,2†], Yan Hong[2†], WeiFeng Chen[3†], Feng Lin[2,3], Jiawei Zeng[1,2], Yueting Huang[2], Li Zhang[2*], Jingwei Yao[2*] and Bing Xu[2*]

[1]The School of Clinical Medicine, Fujian Medical University, Fuzhou, Fujian, China, [2]Department of Hematology, The First Affiliated Hospital of Xiamen University and Institute of Hematology, School of Medicine, Xiamen University, Xiamen, China, [3]Department of Hematology, Shantou Central Hospital, Shantou, Guangdong, China

Abstract

Acute myeloid leukemia (AML) is one of the most threatening hematological malignances. cGAS-STING pathway plays an important role in tumor immunity and development. However, the prognostic role of cGAS-STING pathway in AML remains unknown. Firstly, The expression of cGAS and STING was analyzed by bioinformatics analysis. Subsequently, Bone marrow samples were collected from 120 AML patients and 15 healthy individuals in an independent cohort. The cGAS and STING expression was significantly elevated in AML patients compared with healthy controls. Patients with high cGAS and STING expression had a higher NRAS/KRAS mutation rate and lower complete remission (CR) rate. High cGAS and STING expression was significantly associated with lower overall survival (OS) and disease-free survival (DFS). Our findings revealed that the expression levels of cGAS and STING in AML are elevated. High expression of cGAS and STING correlated with worse OS and DFS and may be a useful biomarker for inferior prognosis in AML patients.

KEYWORDS

cGAS, STING, expression, prognosis, acute myeloid leukemia

Impact statement

Acute myeloid leukemia (AML) is an aggressive hematopoietic malignancy with a high incidence rate and poor clinical prognosis. However, the current understanding of the molecular mechanism of AML development and progress is very limited. In our study, we evaluated the expression of cGAS and STING by collecting bone marrow samples from 120 AML patients and 15 healthy individuals, and found that cGAS-STING pathway was involved in the pathogenesis of AML. The high expression of cGAS and STING is related to the worse OS and DFS, which may be useful biomarkers for the poor prognosis of AML

patients. Our research fills the gap in the pathogenesis of AML and provides potential biomarkers for clinical diagnosis and treatment.

Introduction

Acute myeloid leukemia (AML) is an aggressive hematopoietic malignant disease resulted in high morbidity and unfavorable clinical outcome [1]. Cytogenetics is the backbone for risk stratification, facilitating the classification of AML patients into favorable, intermediate, and poor prognostic groups. However, more than half of AML patients are classified as an intermediate cytogenetic risk group but their clinical outcomes turn out to be distinct [2, 3]. A large percentage of AML patients will suffer from disease recurrences due to the heterogeneous AML clones [4, 5]. The current perception of molecular mechanisms on the development and progression of AML is limited to date [6]. Thus, the identification of new molecular biomarker and revealing of novel mechanism are needed to prompt a more precise risk stratification and develop targeted therapies for AML.

As a vital DNA sensor, cyclic guanosine monophos-phate (GMP)-adenosine monophosphate (AMP) (cGAMP) synthase (cGAS) initiated an innate immunity pathway through binding deviant DNA in the cytosol. cGAMP can activate stimulator of interferon genes (STING), leading to a signaling cascade which produces type I interferons and other functional cytokines [7]. cGAS-STING pathway was previously introduced as a crucial initiator of innate immune and anti-virus responses [8]. Recent studies have revealed the multiple role of cGAS-STING pathway in cancer. Activated cGAS-STING pathway in tumor cells lead to upregulation of various inflammatory genes, such as Type I interferon and impedes the neoplastic progression [9]. There are also related reports in AML, and therefore, many scientists have attempted to increase the expression of type I interferons by upregulating STING, thus achieving the goal of treating AML [10–13]. Yet, mounting evidence indicates that cGAS-STING pathway might provoke inflammation, leading to tumor transformation, development and metastasis in certain diseases [14–16]. Consequently, the relationship between the expression levels of cGAS and Sting in AML and patient prognosis remains unclear.

In this study, we found that cGAS and STING expression levels were higher in AML patients compared with healthy controls by using Gene Expression Profiling Interactive Analysis (GEPIA) and Gene-Set Enrichment Analysis (GSEA) with further validation performed in our cohort. Furthermore, we investigated the impact of cGAS and STING expression on the clinical outcomes of AML patients. Our results indicated that higher expression of cGAS and STING was associated with inferior survival in AML patients.

Materials and Methods

Datasets

The GEPIA[1] integrated the two databases including The Cancer Genome Atlas (TCGA)[2] and the Genotype-Tissue Expression Project (GTEx)[3]. This platform can perform gene expression analysis based on RNA-seq expression data for 9,736 tumor samples and 8,587 control samples [17]. In this study, the GEPIA was used to analyze the expression of cGAS and STING in different tumors. Two gene expression profile datasets (GSE63270 and GSE30029) which involved expression data for healthy and AML bone marrow samples were downloaded from Gene Expression Omnibus (GEO,[4]) [18].

Clinical patients and reverse transcribed quantitative PCR (RT-qPCR)

A total of 120 non-M3 AML patients diagnosed in our department during 2018–2020 were enrolled in the present study. Additionally, 15 healthy allo-HSCT donors were enrolled as control. All patients were diagnosed and classified according to French -American—British (FAB) group and World Health Organization (WHO) classification. Complete remission (CR) was defined by <5% blast cells in the bone marrow and normalization of the peripheral blood counts at 4 weeks after starting induction therapy, without any evidence of extramedullary disease. The written informed consents were provided from all patients in accordance with Declaration of Helsinki.

Ficoll-Hypaque density gradient column (Cytova, Uppsala, Sweden) was used to isolate monocytes. The total RNA was isolated from monocytes by Trizol (Invitrogen, United States), then reverse transcribed into cDNA using BioTeke super RT Kit (BioTeke, Beijing, China). RT-qPCR was performed with an ABI PRISM 7500 real-time PCR system (PE Applied Biosystems, Foster City, CA, United States). We selected β-actin as a control gene to compensate for variations in quality and quantity of RNA and cDNA. The amplification conditions were as follows: 95 °C for 2 min, followed by 40 cycles of 95 °C for 15 s and 60 °C for 30 s. Sequences were as follows:

cGAS - Forward: 5′- CACGAAGCCAAGACCTCCG -3′
cGAS - Reverse: 5′- GTCGCACTTCAGTCTGAGCA -3′
STING - Forward: 5′- CCAGAGCACACTCTCCGGTA -3′
STING - Reverse: 5′- CGCATTTGGGAGGGAGTAGTA -3′
β-actin - Forward: 5′- TGTGGCATCCACGAAACTAC -3′
β-actin - Reverse: 5′- GGAGCAATGATCTTGATCTTCA -3′

1 http://gepia.cancer-pku.cn
2 http://tcga-data.nci.nih.gov/tcga/
3 http://www.gtexportal.org/home/index.html
4 http://www.ncbi.nlm.nih.gov/geo

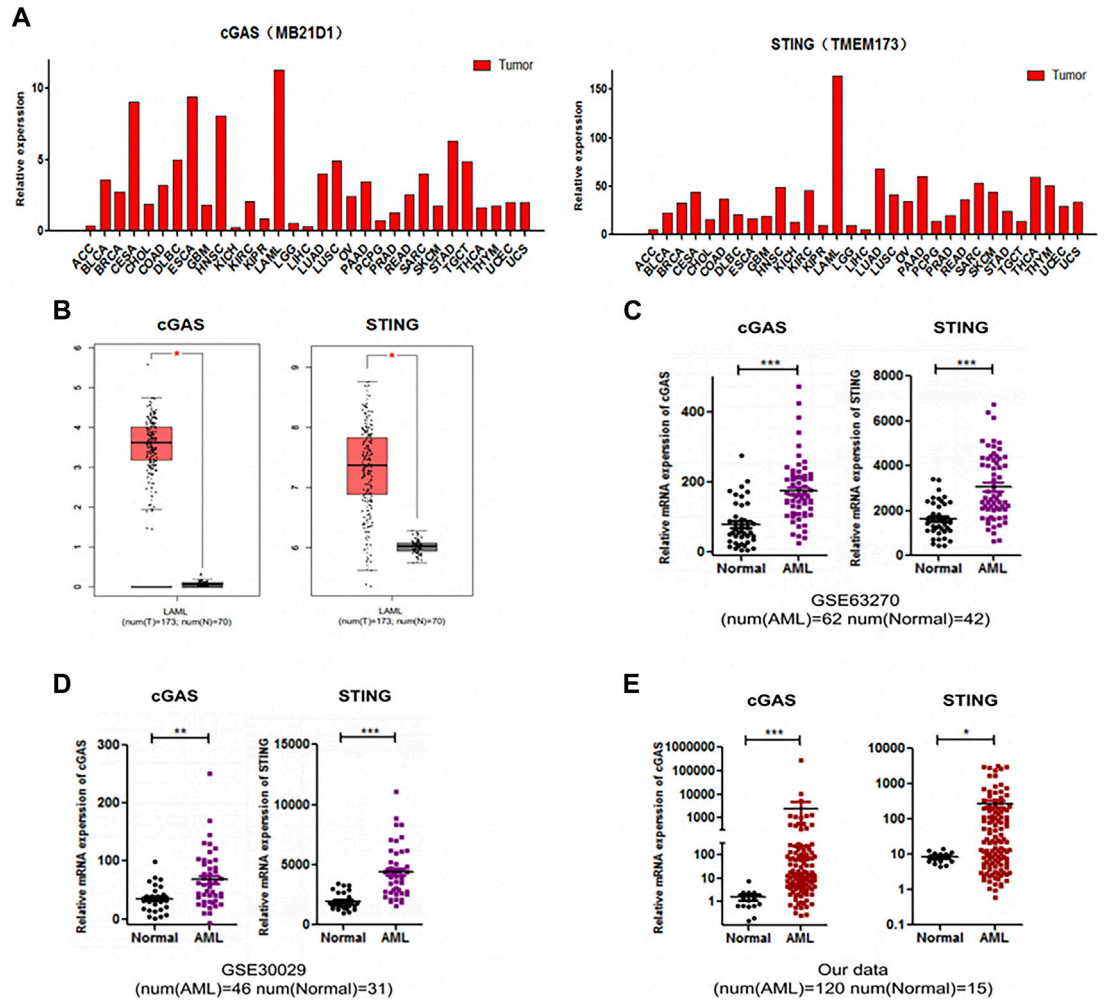

FIGURE 1
The expression levels of cGAS (MB21D1) and SING (TMEM173) were elevated in AML. **(A)** Analysis of the expression of cGAS and SING in different types of tumors, from GEPIA database. **(B–D)** Up-regulated cGAS and STING expression in AML patients compared with normal controls, from GEPIA database (173 AML and 70 normal controls), GEO: GSE63270 (62 AML and 42 normal controls) and GSE30029 (46 AML and 31 normal controls), respectively. **(E)** Validation of cGAS and STING expression of AML patients and normal controls in an independent cohort (120 AML and 15 normal controls). *$p < 0.05$; **$p < 0.01$; ***$p < 0.001$.

The relative expression levels of above genes were calculated using the $2^{-\Delta\Delta CT}$ method (fold change over control expression).

Statistical analysis

All data were analyzed with SPSS (version 20.0; Chicago, IL) and GraphPad Prism 5.0 (GraphPad Software Inc., United States). Overall survival (OS) was calculated from the date of diagnosis until death caused by any reason. Disease-free survival (DFS) was defined as the time from achievement of CR to relapse or the last follow-up. Mann–Whitney *U* test and Chi-square test were used for continuous and categorical variables respectively. The probabilities of OS and DFS were estimated using the Kaplan-Meier method. The expression of cGAS and STING as well as other variables were included in the univariate analysis. Only variables with $p < 0.1$ were included in a Cox proportional hazards model with time-dependent variables. Spear-man rank correlation was used to analyze the correlation between two variables. Unless otherwise specified, p values were based on two-sided hypothesis tests. Alpha was set at 0.05.

Results

Elevated expression levels of cGAS and STING in AML

Firstly, we analyzed the expression levels of cGAS and STING in different types of tumors using GEPIA database. The analysis

TABLE 1 Clinical characteristics of AML patients.

Variable	Total (n = 120)	cGAS expression levels			STING expression levels		
		Low (n = 60)	High (n = 60)	p-value	Low (n = 60)	High (n = 60)	p-value
Sex, male/female	70/50	31/29	38/22	0.268[a]	36/24	33/27	0.712[a]
Median age, year (range)	52 (3–91)	53 (3–86)	49 (5–91)	0.992[b]	52 (3–86)	51 (5–91)	0.940[b]
Median WBC, $\times10^9$/L (range)	18.81 (0.25–279.03)	17.26 (0.25–241.00)	20.05 (1.10–279.03)	0.735[b]	11.58 (0.25–241.00)	22.87 (1.10–279.03)	0.062[b]
Median Hemoglobin, g/L (range)	72 (21–130)	70 (21.0–130)	73 (33–130)	0.729[b]	69.5 (21.0–130.0)	73 (29–130)	0.555[b]
Median Platelet, $\times10^9$/L (range)	41 (3–487)	43 (3–487)	35 (5–157)	0.425[b]	44 (3–487)	35 (5–159)	0.910[b]
Median LDH, U/L (range)	431 (94–3,261)	436 (94–2,450)	390 (154–3,261)	0.410[b]	394 (94–2,450)	433 (150–3,261)	0.315[b]
BM blast, % (range)	59.2 (5.5–96.5)	60.8 (13.0–96.5)	51.2 (5.5–95.5)	0.371[b]	59.9 (20.5–96.5)	54.0 (5.5–95.5)	0.579[b]
Karyotype				0.268[a]			0.857[a]
Normal	55 (45.8%)	29 (48.3%)	26 (43.3%)		28 (46.7%)	27 (45.0%)	
Complex	12 (10.0%)	5 (8.3%)	7 (11.7%)		6 (10%)	6 (10%)	
t (8; 21) or inv (16) or t (16; 16)	17 (14.2%)	7 (11.7%)	10 (16.7%)		10 (16.7%)	7 (11.7%)	
Others	25 (20.8%)	16 (26.7%)	9 (15.0%)		12 (20.0%)	13 (21.7%)	
Missing	11 (9.2%)	3 (5.0%)	8 (13.3%)		4 (6.7%)	7 (11.7%)	
Risk Stratification				**0.040**[a]			0.138[a]
Low	21 (17.5%)	15 (25.0%)	6 (10.0%)		15 (25%)	6 (10%)	
Moderate	25 (20.8%)	15 (25.0%)	10 (16.7%)		13 (21.7%)	12 (20.0%)	
High	63 (53.3%)	27 (45.0%)	36 (61.7%)		28 (46.7%)	35 (58.3%)	
Missing	11 (9.2%)	3 (5.0%)	8 (13.3%)		4 (6.7%)	7 (11.7%)	
FLT-ITD mutation (+/−)	22/86	12/44	10/42	0.815[a]	10/45	12/41	0.637[a]
Isolated biallelic CEBPA mutation (+/−)	16/92	10/46	6/46	0.423[a]	8/47	8/45	1[a]
NPM1 mutation (+/−)	13/95	8/48	5/47	0.560[a]	7/48	6/47	1[a]
AML-ETO (+/−)	11/97	3/53	8/44	0.115[a]	6/49	5/48	1[a]
ASXL1 mutation (+/−)	21/87	10/46	11/41	0.807[a]	13/46	8/41	0.333[a]
RUNX1 mutation (+/−)	16/92	7/49	9/43	0.591[a]	8/47	8/45	1
IDH1 or IDH2 mutation (+/−)	25/83	13/43	12/40	1.000[a]	13/42	12/41	0.237[a]
DNMT3A mutation (+/−)	14/94	7/49	7/45	1.000[a]	6/49	8/45	0.576[a]
TET2 mutation (+/−)	18/90	10/46	8/44	0.800[a]	8/47	10/43	0.612[a]
NRAS or KRAS mutation (+/−)	17/91	4/51	13/40	**0.040**[a]	2/53	15/38	**0.002**[a]

(Continued on following page)

Experimental Biology and Medicine
Published by Frontiers Society for Experimental Biology and Medicine
10.3389/ebm.2024.10108

10.3389/ebm.2024.10108

TABLE 1 (*Continued*) Clinical characteristics of AML patients.

Variable	Total (n = 120)	cGAS expression levels			STING expression levels		
		Low (n = 60)	High (n = 60)	p-value	Low (n = 60)	High (n = 60)	p-value
CBFB-MYH11 (+/−)	5/103	4/52	1/51	0.365[a]	3/52	2/51	1[a]
CR (+/−)	69/28	43/6	26/22	**<0.0001**[a]	39/10	30/18	0.076[a]

Abbreviation: WBC, white blood cell; LDH, lactate dehydrogenase; BM, bone marrow; CR, complete remission.
[a]$\chi 2$ test.
[b]Mann-Whitney U test.
Bold values represent that $p \leq 0.05$.

revealed that cGAS and STING expression levels were higher in AML compared to other tumors (Figure 1A). In addition, the dataset from GEPIA which involved 173 AML and 70 healthy control samples showed that cGAS and STING gene expression was higher in AML samples than healthy controls (Figure 1B). We then analyzed available molecular data from GSE63270 (involved 62 AML and 42 normal controls) and GSE30029 (involved 46 AML and 31 normal controls). In both cohorts, cGAS and STING gene expression levels were higher in AML samples than normal controls in consistence with the result from GEPIA analysis ($p < 0.0001$, Figures 1C, D). To validate the results from above publicly available datasets, we collected bone marrow samples from 120 AML patients and 15 healthy donors and performed the detection of cGAS and STING gene expression. We found that the expression of cGAS and STING was also elevated in AML patients from our cohort ($p < 0.0001$, Figure 1E). Taken together, these results demonstrate that up-regulation of cGAS and STING is a common feature in AML.

Patient characteristics

The baseline characteristics of patients are shown in Table 1. We dichotomized the patients into two high and low groups based on the median values of cGAS and STING expression respectively. The distribution of risk stratification was significantly different in cGAS high and low groups with more patients at high risk in cGAS high group ($p = 0.040$). Patients with higher cGAS expression had a higher NRAS/KRAS mutation rate ($p = 0.040$) and lower CR rate ($p < 0.0001$). Similarly, patients in STING high group had a higher NRAS/KRAS mutation rate ($p = 0.002$) and tended to have a lower CR rate ($p = 0.076$). The other characteristics including age, white blood count, hemoglobin, platelet, lactate dehydrogenase, bone marrow blast percentage, karyotypes, FLT3-ITD mutation, isolated biallelic CEBPA mutation, NPM1 mutation and other mutation between patients with high and low cGAS or STING expression were not significantly different.

High cGAS and STING expression correlated to inferior survival in AML

We further analyzed the overall survival (OS) in an adjusted cohort which excluded 18 untreated patients, 18 patients received allo-HSCT and 5 patients lost to follow-up. The remaining patients received similar treatments. In analysis of disease-free survival (DFS), 6 patients who didn't achieve CR after treatment were further excluded. Kaplan-Meier analysis showed that patients with higher cGAS expression had a shorter OS (377.6 vs. 626.7 days, $p = 0.007$, Figure 2A) as well as a shorter DFS (312.2 vs. 543.9 days, $p = 0.012$, Figure 2B).

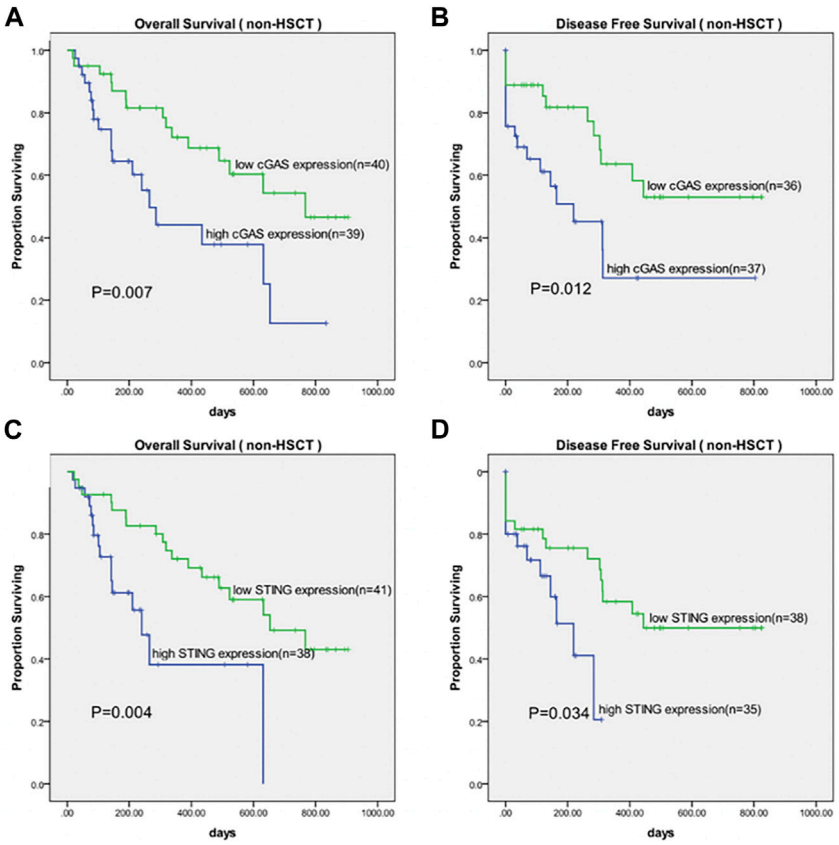

FIGURE 2
Kaplan-Meier survival curves of OS and DFS in patients grouped by median values of cGAS and STING expression. **(A)** Survival curves of OS in cGAS high and low groups. **(B)** Survival curves of DFS in cGAS high and low groups. **(C)** Survival curves of OS in STING high and low groups. **(D)** Survival curves of DFS in STING high and low groups. OS, overall survival; DFS, disease-free survival.

TABLE 2 Multivariate analysis of factors associated with OS and DFS.

Variable	Univariate analysis		Multivariate analysis	
	HR (95% CI)	*p*-value	HR (95% CI)	*p*-value
OS				
cGAS expression	2.910 (1.378–6.146)	0.005	2.348 (1.012–5.447)	0.047
STING expression	2.855 (1.282–6.358)	0.01		
DNMT3a mutation	2.543 (1.008–6.418)	0.048	3.420 (1.254–9.324)	0.016
TET2 mutation	2.039 (0.936–4.446)	0.073	2.521 (1.050–6.048)	0.038
allo-HSCT	0.205 (0.049–0.862)	0.031	0.171 (0.040–0.737)	0.018
DFS				
cGAS expression	2.411 (1.119–5.195)	0.025	2.420 (1.071–5.469)	0.034
DNMT3a mutation	2.568 (1.015–6.5)	0.047	3.900 (1.441–10.774)	0.008
TET2 mutation	2.481 (1.090–5.645)	0.03	2.936 (1.189–7.250)	0.02
allo-HSCT	0.198 (0.047–0.836)	0.028	0.158 (0.035–0.709)	0.016

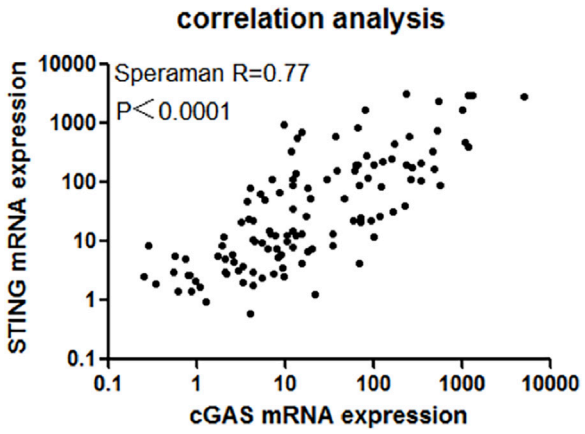

FIGURE 3
There existed a strong positive correlation between cGAS and STING expression (R = 0.77, 95% CI: 0.6884–0.8301, p < 0.0001).

Likewise, patients with higher STING expression had a shorter OS (332.9 vs. 612.7 days, p = 0.004, Figure 2C) as well as a shorter DFS (178.3 vs. 507.8 days, p = 0.034, Figure 2D).

Univariate and multivariate analysis of factors affecting OS and DFS

The correlation between high cGAS and STING expression with inferior survival in AML patients indicated cGAS and STING expression levels might be of prognostic importance for AML. The results of univariate and multivariate analysis of factors affecting OS and DFS were shown in Table 2. The factors shown in patient characteristics were included in univariate analysis and variables with p < 0.1 were further analyzed in multivariate analysis. In multivariate Cox regression analysis, high cGAS expression was associated with inferior OS (HR = 2.348, 95% CI: 1.012–5.447; p = 0.047) and DFS (HR = 2.420, 95% CI: 1.071–5.469; p = 0.034). Nevertheless, it showed that there was no association between STING gene expression and OS or DFS. Besides, DNMT3a mutation, TET2 mutation were shown to be associated with worse OS and DFS while receiving allo-HSCT was associated with improved OS and DFS.

Positive correlation between cGAS and STING gene expression

As the above results showed, cGAS and STING expression was up-regulated in AML patients compared with normal controls. Although cGAS and SING are the entry of cGAS-STING pathway, previous study showed cGAS and STING expression could be regulated inconsistently in NSCLC [19]. We wondered whether cGAS and STING were up-regulated in a synchronized manner on the context of AML. Our result showed that in AML, cGAS expression was positively correlated with STING expression (R = 0.77, 95% CI: 0.6884–0.8301, p < 0.0001, Figure 3).

Discussion

AML is a highly genetically heterogeneous malignant myeloproliferative disorder of bone marrow, accounting for ~10% of all hematological diseases [1, 20]. While the next-generation sequencing technology has been tremendously developed, numerous recurrent point mutations, epigenetic changes as well as cytogenetic abnormality have been thoroughly recognized [21, 22]. Cytogenetics combined with mutations form the basis of the risk classification system, which facilitates the risk stratification for patients. However, up to 50% patients have been diagnosed as intermediate risk AML with a wide range of clinical outcomes. Thus, the identification of vital mechanisms affecting AML management and patient survival may boost the development of AML specific targeted therapies and meticulous risk stratification.

The results from current study indicated that high cGAS and STING expression correlated to inferior survival in AML. In multivariate analysis, only cGAS expression was found to be an independent factor affecting OS and DFS. It was intriguing that the expression level of STING showed impact on OS but not on DFS. Since our result showed cGAS and STING had a strong positive correlation, there might exist an overlapped effect of cGAS and STING expression on the clinical outcomes. Besides, recent work has demonstrated that cGAS and STING may act in an independent way from one another. Upon etoposide-induced DNA damage, STING could be activated independently from the catalytic function of cGAS [23]. The exquisite molecular mechanism defining the acting pattern of cGAS and STING in AML remained undetermined. In this regard, future studies are needed to investigate whether combination of cGAS and STING expression detection is necessary and cGAS gene expression alone can be an indicator for prognosis in AML.

Previous studies indicated the activation of cGAS-STING pathway contributed to cancer suppression by promoting host immuno-surveillance and inducing cellular senescence [24–27]. In line with these findings, cGAS-STING pathway was identified as a prognostic biomarker for improved clinical outcomes in hepatocellular carcinoma and non-small cell lung cancer (NSCLC) [19, 28]. However, other studies revealed that cGAS-STING pathway promoted tumor development and progression in Lewis lung carcinoma, brain and colorectal cancer [14, 15, 29]. One possible mechanism was that chronic stimulation of cGAS-STING pathway might lead to inflammation-driven carcinogenesis [30]. The topic that pro-inflammatory mediators are linked to AML cell growth has gain traction in recent years. Plenty of studies reported that chronic immune-stimulatory or autoimmune disease could be sick factors for developing AML [31, 32]. Here, our results suggested that cGAS-STING pathway also had a potential role in driving malignant programs and suppressing antitumor functions in AML. Whether hyper-activation of cGAS-STING

pathway fueled the progression of AML via induction of inflammation requires further exploration. Also, future studies will be required to elucidate mechanism of hyper-activation cGAS-STING signaling in AML.

At present, NRAS/KRAS mutations are widely considered to be associated with poor prognosis in a variety of cancers, including colorectal cancer and serous ovarian cancer [33, 34]. NRAS mutations were identified in 10%–11% of AML, and KRAS mutations in an additional 5% [35, 36], however, how it affects cGAS-STING levels in AML has not been reported. Only one study in KRAS-mutant non-small-cell lung carcinoma lung cancer (NSCLC) may be relevant. In this study, the authors found that NRF2 promotes the transcription and expression of BRCA1 to repair DNA damage, leading to inactivation of the STING pathway [37]. In our study, the frequency of NRAS/KRAS mutation was higher in both cGAS and STING high group. TBK1 is the important downstream effector program of cGAS-STING signaling [7]. Previous work presented that TBK1 supported key, context specific tumorigenic activity in Ras-mutant/mesenchymal NSCLC [38]. The interaction between cGAS-STING pathway including its downstream signaling with NRAS/KRAS mutation on the context of AML would be an interesting area of research. Additionally, we found that elevated expression of cGAS was associated with higher risk stratification and a lower CR rate. Chromosomal instability (CIN) is a hallmark of cancer as well as a primary source of cytosolic dsDNA and it promotes the activation of cGAS-STING [39]. Intriguingly, some scholars found that cGAS could exert the function of maintaining CIN, which potentiated tumor evolution [40, 41]. In our study, AML patients had shown hyper-activation of the cGAS-STING pathway before treatment. The following chemotherapy further induced CIN, which might cooperate with cGAS-STING, leading to further perturbation of this pathway. Yet, the underlying mechanisms that define the effect of cGAS-STING pathway on treatment response in AML patients need further exploration.

In summary, our data revealed a prognosis role of cGAS-STING pathway for clinical outcomes and a positive correlation between cGAS and STING in AML. However, we recognize the limitations to our study, including the limited number of patients enrolled and the lack of relevant mechanism studied. In addition, the cGAS-STING downstream signaling programs including TBK1, IRF3, JAK2/STAT3, NF-κB were not studied in this study. Besides, it is important to note that the dichotomous roles of cGAS-STING in tumor immunity and development are cell and context - dependent [42]. Thus, in future study, a pinpoint cGAS-STING expression state should be better characterized in both immune cells and non-immune cells including tumor cells as well as stromal cell resident in bone marrow environment of AML patients. Despite various approaches for AML investigated, treatment resistance remains a leading cause of AML-related deaths [43]. Based on the results of this study, further studies of novel approaches targeting the cGAS-STING pathway in AML may provide potential for advancing AML therapeutic strategies.

Author contributions

Conceptualization, QLC and YH; Data curation, WFC, LZ, and YTH; Formal analysis, JWY, YH, and BX; Funding acquisition, FL, JWY, and BX; Methodology, QLC, JWZ, and WFC; Resources, QLC and BX; Software, FL, YTH, and BX; Supervision, JWY and BX; Validation, QLC and LZ; Writing the Original draft, JWY, QLC, and YH; Reviewing and editing the manuscript, JWY, QLC, and YH.

Data availability statement

The original contributions presented in the study are included in the article/supplementary material, further inquiries can be directed to the corresponding authors.

Ethics statement

The studies involving humans were approved by the Ethics Committee of The First Affiliate Hospital of Xiamen University (protocol code KY-2018-015 and 7 March 2018 of approval). The studies were conducted in accordance with the local legislation and institutional requirements. The participants provided their written informed consent to participate in this study.

Conflict of interest

The authors declare that the research was conducted in the absence of any commercial or financial relationships that could be construed as a potential conflict of interest.

Funding

The author(s) declare financial support was received for the research, authorship, and/or publication of this article. This work was supported by the National Natural Science Foundation of China (81770126, 81770161, and 81800163), the Xiamen Municipal Bureau of Science and Technology (No. 3502Z20224011, 3502Z20227346, and 3502Z20227261) and the Natural Science Foundation of Xiamen City (20231301).

Publisher's note

Please note that the review of this paper was conducted at the previous publisher, SAGE.

References

1. Estey E, Döhner H. Acute myeloid leukaemia. *The Lancet* (2006) **368**:1894–907. doi:10.1016/s0140-6736(06)69780-8

2. Grimwade D, Walker H, Oliver F, Wheatley K, Harrison C, Harrison G, et al. The importance of diagnostic cytogenetics on outcome in AML: analysis of 1,612 patients entered into the MRC AML 10 trial. *Blood* (1998) **92**:2322–33. doi:10.1182/blood.v92.7.2322.2322_2322_2333

3. Byrd JC, Mrozek K, Dodge RK, Carroll AJ, Edwards CG, Arthur DC, et al. Pretreatment cytogenetic abnormalities are predictive of induction success, cumulative incidence of relapse, and overall survival in adult patients with *de novo* acute myeloid leukemia: results from Cancer and Leukemia Group B (CALGB 8461). *Blood* (2002) **100**:4325–36. doi:10.1182/blood-2002-03-0772

4. Ho T-C, LaMere M, Stevens BM, Ashton JM, Myers JR, O'Dwyer KM, et al. Evolution of acute myelogenous leukemia stem cell properties after treatment and progression. *Blood* (2016) **128**:1671–8. doi:10.1182/blood-2016-02-695312

5. Ishikawa F, Yoshida S, Saito Y, Hijikata A, Kitamura H, Tanaka S, et al. Chemotherapy-resistant human AML stem cells home to and engraft within the bone-marrow endosteal region. *Nat Biotechnol* (2007) **25**:1315–21. doi:10.1038/nbt1350

6. Estey EH. Acute myeloid leukemia: 2019 update on risk-stratification and management. *Am J Hematol* (2018) **93**:1267–91. doi:10.1002/ajh.25214

7. Zhang X, Bai XC, Chen ZJ. Structures and mechanisms in the cGAS-STING innate immunity pathway. *Immunity* (2020) **53**:43–53. doi:10.1016/j.immuni.2020.05.013

8. Hopfner KP, Hornung V. Molecular mechanisms and cellular functions of cGAS-STING signalling. *Nat Rev Mol Cell Biol* (2020) **21**:501–21. doi:10.1038/s41580-020-0244-x

9. Kwon J, Bakhoum SF. The cytosolic DNA-sensing cGAS-STING pathway in cancer. *Cancer Discov* (2020) **10**:26–39. doi:10.1158/2159-8290.cd-19-0761

10. Curran E, Chen X, Corrales L, Kline DE, Dubensky TW, Jr, Duttagupta P, et al. STING pathway activation stimulates potent immunity against acute myeloid leukemia. *Cell Rep* (2016) **15**:2357–66. doi:10.1016/j.celrep.2016.05.023

11. Kogan AA, Topper MJ, Dellomo AJ, Stojanovic L, McLaughlin LJ, Creed TM, et al. Activating STING1-dependent immune signaling in TP53 mutant and wild-type acute myeloid leukemia. *Proc Natl Acad Sci U S A* (2022) **119**:e2123227119. doi:10.1073/pnas.2123227119

12. Song C, Liu D, Liu S, Li D, Horecny I, Zhang X, et al. SHR1032, a novel STING agonist, stimulates anti-tumor immunity and directly induces AML apoptosis. *Sci Rep* (2022) **12**:8579. doi:10.1038/s41598-022-12449-1

13. Song X, Peng Y, Wang X, Chen Q, Lan X, Shi F. The stimulator of interferon genes (STING) agonists for treating acute myeloid leukemia (AML): current knowledge and future outlook. *Clin Transl Oncol* (2022) **25**:1545–53. doi:10.1007/s12094-022-03065-6

14. Chen Q, Boire A, Jin X, Valiente M, Er EE, Lopez-Soto A, et al. Carcinoma-astrocyte gap junctions promote brain metastasis by cGAMP transfer. *Nature* (2016) **533**:493–8. doi:10.1038/nature18268

15. Lemos H, Mohamed E, Huang L, Ou R, Pacholczyk G, Arbab AS, et al. STING promotes the growth of tumors characterized by low antigenicity via IDO activation. *Cancer Res* (2016) **76**:2076–81. doi:10.1158/0008-5472.can-15-1456

16. Ahn J, Xia T, Konno H, Konno K, Ruiz P, Barber GN. Inflammation-driven carcinogenesis is mediated through STING. *Nat Commun* (2014) **5**:5166. doi:10.1038/ncomms6166

17. Tang Z, Li C, Kang B, Gao G, Li C, Zhang Z. GEPIA: a web server for cancer and normal gene expression profiling and interactive analyses. *Nucleic Acids Res* (2017) **45**:W98–w102. doi:10.1093/nar/gkx247

18. Barrett T, Wilhite SE, Ledoux P, Evangelista C, Kim IF, Tomashevsky M, et al. NCBI GEO: archive for functional genomics data sets--update. *Nucleic Acids Res* (2012) **41**:D991–5. doi:10.1093/nar/gks1193

19. Raaby Gammelgaard K, Sandfeld-Paulsen B, Godsk SH, Demuth C, Meldgaard P, Sorensen BS, et al. cGAS-STING pathway expression as a prognostic tool in NSCLC. *Transl Lung Cancer Res* (2021) **10**:340–54. doi:10.21037/tlcr-20-524

20. Döhner H, Estey EH, Amadori S, Appelbaum FR, Büchner T, Burnett AK, et al. Diagnosis and management of acute myeloid leukemia in adults: recommendations from an international expert panel, on behalf of the European LeukemiaNet. *Blood* (2010) **115**:453–74. doi:10.1182/blood-2009-07-235358

21. Ley TJ, Mardis ER, Ding L, Fulton B, McLellan MD, Chen K, et al. DNA sequencing of a cytogenetically normal acute myeloid leukaemia genome. *Nature* (2008) **456**:66–72. doi:10.1038/nature07485

22. Care MA, Barrans S, Worrillow L, Jack A, Westhead DR, Tooze RM. A microarray platform-independent classification tool for cell of origin class allows comparative analysis of gene expression in diffuse large B-cell lymphoma. *PLoS One* (2013) **8**:e55895. doi:10.1371/journal.pone.0055895

23. Dunphy G, Flannery SM, Almine JF, Connolly DJ, Paulus C, Jønsson KL, et al. Non-canonical activation of the DNA sensing adaptor STING by ATM and IFI16 mediates NF-κB signaling after nuclear DNA damage. *Mol Cell* (2018) **71**:745–60.e5. doi:10.1016/j.molcel.2018.07.034

24. Yang H, Wang H, Ren J, Chen Q, Chen ZJ. cGAS is essential for cellular senescence. *Proc Natl Acad Sci U S A* (2017) **114**:E4612–e20. doi:10.1073/pnas.1705499114

25. Glück S, Guey B, Gulen MF, Wolter K, Kang TW, Schmacke NA, et al. Innate immune sensing of cytosolic chromatin fragments through cGAS promotes senescence. *Nat Cell Biol* (2017) **19**:1061–70. doi:10.1038/ncb3586

26. Diamond MS, Kinder M, Matsushita H, Mashayekhi M, Dunn GP, Archambault JM, et al. Type I interferon is selectively required by dendritic cells for immune rejection of tumors. *J Exp Med* (2011) **208**:1989–2003. doi:10.1084/jem.20101158

27. Ahn J, Konno H, Barber GN. Diverse roles of STING-dependent signaling on the development of cancer. *Oncogene* (2015) **34**:5302–8. doi:10.1038/onc.2014.457

28. Qi Z, Yan F, Chen D, Xing W, Li Q, Zeng W, et al. Identification of prognostic biomarkers and correlations with immune infiltrates among cGAS-STING in hepatocellular carcinoma. *Biosci Rep* (2020) **40**:BSR20202603. doi:10.1042/BSR20202603

29. An X, Zhu Y, Zheng T, Wang G, Zhang M, Li J, et al. An analysis of the expression and association with immune cell infiltration of the cGAS/STING pathway in pan-cancer. *Mol Ther - Nucleic Acids* (2019) **14**:80–9. doi:10.1016/j.omtn.2018.11.003

30. Khoo LT, Chen LY. Role of the cGAS-STING pathway in cancer development and oncotherapeutic approaches. *EMBO Rep* (2018) **19**:e46935. doi:10.15252/embr.201846935

31. Ramadan SM, Fouad TM, Summa V, Hasan SK, Lo-Coco F. Acute myeloid leukemia developing in patients with autoimmune diseases. *Haematologica* (2012) **97**:805–17. doi:10.3324/haematol.2011.056283

32. Carey A, Edwards DK, Eide CA, Newell L, Traer E, Medeiros BC, et al. Identification of interleukin-1 by functional screening as a key mediator of cellular expansion and disease progression in acute myeloid leukemia. *Cell Rep* (2017) **18**:3204–18. doi:10.1016/j.celrep.2017.03.018

33. De Roock W, Claes B, Bernasconi D, De Schutter J, Biesmans B, Fountzilas G, et al. Effects of KRAS, BRAF, NRAS, and PIK3CA mutations on the efficacy of cetuximab plus chemotherapy in chemotherapy-refractory metastatic colorectal cancer: a retrospective consortium analysis. *Lancet Oncol* (2010) **11**:753–62. doi:10.1016/s1470-2045(10)70130-3

34. Emmanuel C, Chiew YE, George J, Etemadmoghadam D, Anglesio MS, Sharma R, et al. Genomic classification of serous ovarian cancer with adjacent borderline differentiates RAS pathway and TP53-mutant tumors and identifies NRAS as an oncogenic driver. *Clin Cancer Res* (2014) **20**:6618–30. doi:10.1158/1078-0432.ccr-14-1292

35. Bacher U, Haferlach T, Schoch C, Kern W, Schnittger S. Implications of NRAS mutations in AML: a study of 2502 patients. *Blood* (2006) **107**:3847–53. doi:10.1182/blood-2005-08-3522

36. Bowen DT, Frew ME, Hills R, Gale RE, Wheatley K, Groves MJ, et al. RAS mutation in acute myeloid leukemia is associated with distinct cytogenetic subgroups but does not influence outcome in patients younger than 60 years. *Blood* (2005) **106**:2113–9. doi:10.1182/blood-2005-03-0867

37. Xiaodan S, Peiyan Z, Hui L, Yan L, Ying C. NRF2 participates in the suppressive tumor immune microenvironment of KRAS/KEAP1 co-mutant non-small cell lung cancer by inhibiting the STING pathway. *Genes Dis* (2023) **10**:1727–30. doi:10.1016/j.gendis.2022.10.009

38. Cooper JM, Ou YH, McMillan EA, Vaden RM, Zaman A, Bodemann BO, et al. TBK1 provides context-selective support of the activated AKT/mTOR pathway in lung cancer. *Cancer Res* (2017) **77**:5077–94. doi:10.1158/0008-5472.can-17-0829

39. Wan D, Jiang W, Hao J. Research advances in how the cGAS-STING pathway controls the cellular inflammatory response. *Front Immunol* (2020) **11**:615. doi:10.3389/fimmu.2020.00615

40. Bakhoum SF, Cantley LC. The multifaceted role of chromosomal instability in cancer and its microenvironment. *Cell* (2018) **174**:1347–60. doi:10.1016/j.cell.2018.08.027

41. Liu H, Zhang H, Wu X, Ma D, Wu J, Wang L, et al. Nuclear cGAS suppresses DNA repair and promotes tumorigenesis. *Nature* (2018) **563**:131–6. doi:10.1038/s41586-018-0629-6

42. Ng KW, Marshall EA, Bell JC, Lam WL. cGAS-STING and cancer: dichotomous roles in tumor immunity and development. *Trends Immunol* (2018) **39**:44–54. doi:10.1016/j.it.2017.07.013

43. Witkowski MT, Lasry A, Carroll WL, Aifantis I. Immune-based therapies in acute leukemia. *Trends Cancer* (2019) **5**:604–18. doi:10.1016/j.trecan.2019.07.009

EBM Experimental Biology and Medicine

TYPE Original Research
PUBLISHED 15 February 2024
DOI 10.3389/ebm.2024.10114

OPEN ACCESS

*CORRESPONDENCE
Rebecca C. Christofferson,
rcarri1@lsu.edu

RECEIVED 07 August 2023
ACCEPTED 11 December 2023
PUBLISHED 15 February 2024

CITATION
Turner EA and Christofferson RC (2024), Exploring the transmission modalities of Bunyamwera virus.
Exp. Biol. Med. 249:10114.
doi: 10.3389/ebm.2024.10114

Exploring the transmission modalities of Bunyamwera virus

Erik A. Turner and Rebecca C. Christofferson*

Department of Pathobiological Sciences, Louisiana State University, Baton Rouge, LA, United States

Abstract

Bunyamwera virus (BUNV) (*Bunyamwera orthobunyavirus*) has been found in Sub-Saharan Africa and demonstrated recently as cocirculating with Rift Valley Fever Virus (RVFV). Little is known regarding the breadth of transmission modalities of Bunyamwera. Given its co-occurence with RVFV, we hypothesized the transmission system of BUNV shared similarities to the RVFV system including transmission by *Ae. aegypti* mosquitoes and environmentally mediated transmission through fomites and environmental contamination. We exposed *Ae. aegypti* mosquitoes to BUNV and evaluated their ability to transmit both vertically and horizontally. Further, we investigated the potential for a novel transmission modality via environmental contamination. We found that the LSU colony of *Ae. aegypti* was not competent for the virus for either horizontal or vertical transmission; but, 20% of larva exposed to virus via contaminated aquatic habitat were positive. However, transstadial clearance of the virus was absolute. Finally, under simulated temperature conditions that matched peak transmission in Rwanda, we found that BUNV was stable in both whole blood and serum for up to 28 days at higher total volume in tubes at moderate quantities (10^{3-5} genome copies/mL). In addition, infectiousness of these samples was demonstrated in 80% of the replicates. At lower volume samples (in plates), infectiousness was retained out to 6–8 days with a maximum infectious titer of 10^4 PFU/mL. Thus, the potential for contamination of the environment and/or transmission via contaminated fomites exists. Our findings have implications for biosafety and infection control, especially in the context of food animal production.

KEYWORDS

Orthobunyavirus, Bunyamwera, *Aedes aegypti*, environmental transmission, transovarial transmission

Impact statement

In many areas where infection control and/or the use of personal protective equipment is not common, there is a risk of transmission via fomites when pathogens are environmentally stable. Our findings demonstrate that BUNV, though an RNA virus, is very environmentally stable and retains infectiousness under certain conditions. Our findings establish the proof-of-principle for this novel transmission modality of environmental contamination of BUNV.

Introduction

Bunyamwera virus (BUNV) (*Bunyamwera orthobunyavirus*) has been found in Sub-Saharan Africa and demonstrated recently as cocirculating with Rift Valley Fever Virus (RVFV) [1]. RVFV is a mosquito-borne arbovirus of One Health importance. Infected ruminates can experience hemorrhagic fever, spontaneous abortions, and potentially death, especially in young animals [2]. This has not only the obvious animal health implications but can be economically devastating in areas where cattle are a main source of food and/or income [3]. Humans infected with RVFV can also experience hemorrhagic fever, ocular complications, sever flu like symptoms, and death [4]. Originally isolated during an outbreak in the Rift Valley of Kenya in 1930 [5], RVFV has since been found in countries in across Africa and on the Arabian peninsula [6]. As seen with other mosquito-borne viruses, viral transmission of RVFV can often be tied to environmental factors, such as heavy seasonal rainfall and flooding events [7].

During an outbreak of RVFV in Rwanda, BUNV was found to be the etiological agent of abortions in cattle where clinical diagnosis would have attributed such symptoms to RVFV [1]. These two viruses are from the same order (*Bunyavirales*) and are both arboviruses transmitted by mosquitoes [8–13]. BUNV has historically been found in Sub-Saharan Africa. While BUNV can infect humans as well, causing mild symptoms including fever, myalgia/arthralgia, and rashes, the virus has been most often associated with ruminate infection and disease, including spontaneous abortions [1, 14–18]. These symptoms overlap with RVFV, though the transmission patterns of BUNV remain to be fully characterized, and is likely under surveilled. However, given the coincident transmission of RVFV and BUNV, it is reasonable to hypothesize that the BUNV transmission system may share similarities with that of RVFV.

The current understanding of the RVFV transmission cycle includes outbreak/epidemic and maintenance subcycles (Supplementary Figure S1) [9]. The maintenance cycle involves mosquitoes–believed to be including the genus *Aedes*–obtaining infected bloodmeals, subsequently developing a systemic infection, including the ovaries, which results in transovarial transmission [19–21]. *Aedes* spp. eggs are resistant to desiccation [22, 23], allowing for survival through the dry season and, the return of seasonal rains facilitate the hatch of floodwater and container *Aedes* mosquito eggs and the subsequent emergence of infected adults [24]. This mechanism of maintenance through the dry season then seeds a seasonal outbreak, which transitions into the outbreak subcycle, as large numbers of *Culex* spp. mosquitoes hatch after rain events [25, 26]. Additional transmission pathways exist that do not involve the vector. RVFV is a bloodborne pathogen and transmission to humans occurs with handling of infectious fluids from ill livestock, as well as processing raw meat [27–29]. Risk of infection also increased with handling of abortive material [28], which suggests that environmentally mediated infections are an important piece of the transmission puzzle. Adding to the risk of environmentally mediated transmission of RVFV, stability and persistence of infection was noted when originally isolated, as it was found that RVFV is stable in a citrine solution at room temperature for over 7 days [5], and subsequently, this phenomena was replicated at a wide variety of temperatures [30–32], including a potential infection occurring from a sample months old [33]. Further, contamination of larval habitat has been shown to infect larva and emerge as infected adults, indicating that environmentally mediated transmission is a non-negligible part of RVFV transmission risk [34].

Aedes aegypti, an important vector of a multitude of human pathogens, is one of the *Aedes* spp. competent for RVFV and BUNV, and several strains were found to be competent vectors of a closely related North American *Orthobunyavirus* species, Cache Valley virus [35–40]. Transovarial transmission of RVFV in *Aedes aegypti* was implicated in the 2007 outbreak in Sudan [41] and has been shown to be successful and stable for three ovarian cycles [20], as well as for a related *Orthobunyavirus,* LaCrosse virus. But transovarial transmission has not been rigorously studied in *Ae. aegypti* for BUNV [42]. Previously, it was demonstrated that BUNV retained infectiousness in cell culture for up to 30 days at 37°C [43]. This sustained persistence led to the consideration of whether BUNV might overlap in the environmentally mediated transmission subcycle of RVFV, as well. Herein, we explore the potential that the BUNV transmission cycle is complex and multi-faceted, like that of RVFV. We investigate the competence of *Aedes aegypti* for vertical and horizontal transmission, and examine factors associated with risk for environmentally mediated transmission under relevant temperature conditions.

Materials and methods

Daily Rwandan temperature profile

To simulate relevant temperature conditions, publicly available weather data was mined to generate a daily temperature profile for RVF transmission season in Rwanda, May through July, per the 2018 outbreak [1]. A data scraper collected temperature data in half-hour increments from May 18th through July 12th, 2018, and the temperatures from the same time point each day were averaged to make a single average day. The environmental chamber was then programed to mimic these conditions and a digital thermometer was placed within to confirm the temperature (Supplementary Figure S2). Humidity was maintained at approximately 85% during the experiments roughly matching historical humidity in Rwanda [44].

Viruses and mosquitoes

BUNV was obtained from the World Arbovirus Reference Center at UTMB had been passaged through suckling mouse cells 47 times and Vero cells 6–8 times prior to the experimentation. Stocks were titered via crystal violet plaque assay and determined to be ~5.0 × 10^6 pfu/mL. *Aedes aegypti* mosquito (Rockefeller colony) eggs from were vacuum hatched for 45 min in ddH_20 and allowed to emerge as in [45].

qRT-PCR and plaque assay

Viral RNA extraction was performed via MagMax 96 viral isolation as in [43]. qRT-PCR was performed on a Roche Lightcycler 96, using Quantbio Ultratough master mix and previously published primers and probes [43]. Viral RNA quantification was analyzed via comparison to previously crystal violet plaqued stock from above. Standard crystal violet plaque assays were performed [46]. Virus titer was averaged from countable plaques at each dilution [47].

qRT-PCR sensitivity assay for mosquito pools

Ae. aegypti reared as above were allowed to mature to adults. Adult mosquitoes were cold anesthetized and separated by sex and placed in to 900 µL BA-1 media with 2 stainless steel BBs in a 2 mL locking Eppendorf tube in pools of 10 and homogenized as previously described [45] and a known titer of virus was added to each tube of titers of 10^5, 10^3, 10^1, and 10^0 pfu/mL. Five replicates per pools sex were performed at each titer.

Mosquito competence and transstadial transmission

Adult *Aedes aegypti* females, 2 days post emergence (dpe) were offered an infectious blood meal of ratio 2:1 of bovine blood in Alsevers (Hemostat Labs, Dixon, CA, United States) and BUNV infectious supernatant (total infectious titer 1.7 × 10^6) via the Hemotek feeding apparatus (Discovery Labs, Blackburn, United Kingdom). Engorged females were separated by aspiration and cold anesthetization, then placed in individual 4-ounce containers and provided 10% sucrose solution *ad libitum*. Each container was supplied with egg paper that was moistened daily and collected when eggs were observed for an additional 18 days. Three females died prior to the end of the experiment and were collected and tested for virus in the legs and bodies as described below. At 18 days post infectious bloodmeal, mosquitoes were processed to determine infection status of bodies, legs, and saliva as in [48].

There is mixed evidence for the role of second bloodmeals in enhancing vector competence [48–51]. Thus, a second cohort of mosquitoes was offered an infectious bloodmeal as above at 3–4 days post emergence. A second uninfected bloodmeal was offered starting at 4 days following the first bloodmeal [50] and repeated attempts were made until all females had taken a second bloodmeal (maximum 9 days following first bloodmeal). The mosquitoes were maintained as described above until processed following egg collection at 22–24 post initial, BUNV infectious bloodmeal.

Environmental mediated transmission of BUNV to *Ae. aegypti* (transstadial transmission)

Ae. aegypti were hatched and reared as described above. Fourth instar larva were collected and rinsed in ddH_20 and placed into water contaminated with BUNV. Briefly, BUNV supernatant was added to rearing water, and samples were collected at 0–5 days to establish the presence of BUNV RNA [34]. Exposed larva were allowed to mature and were collected as pupa, rinsed, and transferred to a cage for emergence. Pupa were separated based on number of days spent exposed to infected rearing water. Upon emergence, adult mosquitoes were cold anesthetized and separated by sex into pools of up to five based on exposure time. Remaining unemerged individuals were collected at 6 days post contaminated water exposure, rinsed as above, and collated into pools of up to ten for testing by qRT-PCR.

BUNV environmental stability study

To assess environmental stability of BUNV under environmentally relevant conditions, 110 µL of virus was added to 4.39 mL of two different substrate types–either whole blood or serum for a final concentration of 1 × 105 pfu/mL. The virus-substrate mixture was added to individual units (either falcon tubes or 6-well plates, see Supplementary Methods) and placed into the environmental chamber under Rwanda temperature conditions. Tubes were uncapped and the six-well plate lids lifted to allow air exposure; all units were placed in secondary containment for safety and contamination avoidance. Tubes were sampled at days 0, 1, 7, 21, and 28, while plates were sampled each day until dry. Plates were sampled daily until dry, which occurred between 6 and 8 days. Collected samples were placed into a −80°C freezer until further analysis. Samples were tested starting with the latest timepoint (tubes) or with the day before the plate was dry (Dry Day −1). If a sample was found not to be infectious at a timepoint (I.e., timepoint *X*), the timepoint immediately preceding (i.e., timepoint *X-1*) was tested and this pattern continued until we found the latest time of infectivity. Ten replicates of each unit type were conducted per substrate type. Samples were assayed for stability of RNA via qRT-PCR as above and for infectivity via a growth assay on Vero cells as in [43].

TABLE 1 Infection of larva through contaminated water and subsequent transstadial transmission.

Life stage	Number of pools (n = 5/pool)	Number of positive pools	Minimum rate of detection (%)	Average quantity recovered (genome equivalents/mL)
Larva	19	5 (26%)	8.33	1.17×10^1
Pupa	1	0	0	NA
Adult	18	0	0	NA

Results from exposure in contaminated rearing water reveal successful uptake of BUNV and/or viral RNA by larva, but unsuccessful transstadial transmission.

Statistics

For the sensitivity assay, a Kruskal Wallace non-parametric analysis of variance was used to determine if a difference in detection ability existed between sexes of the pools. A linear regression model was used to evaluate the relationship between the initial input into the mosquito pool and the qRT-PCR output. The limit of detection (LOD) was determined using a qPCR LOD calculation R script (at 95% confidence) [52, 53]. The lowest concentration of consistently detectable RNA was determined by running multiple iterations of a standard curve assay tied to a plaque assay. The plaque assay revealed that maximum stock titer was 5.3×10^6 PFU/mL. The standard curve runs determined that the consistent point at which there was below 95% confidence detection was 5.3×10^{-1} PFU/mL. Growth was assessed via non-parametric t-test between day 1 and day 7 where a significantly higher titer at day 7 indicated growth and thus infectiousness. To evaluate stability, RNA recovered at each timepoint was compared via a Kruskal-Wallace test where day was a factor; a *post hoc* Dunn's test (Bonferroni correction) test was performed where appropriate. Additionally, comparisons between RNA recovered from each substrate at the same timepoint or day until dry were done via Wilcoxon Ranked Sum tests. Significance was assessed at the $\alpha = 0.05$ level. Analyses were performed using R Studio (2023.03.1 + 446) and R (4.3.0) and associated packages [54]. Minimum infection rate was determined by calculating the rate of infection as if only one individual per positive pool was infected, as in [55].

Results

Sensitivity assay

The qRT-PCR assay used herein was highly sensitive for BUNV in the context of mosquito pool testing (LOD = 6.6 copies/mL with 95% confidence). There was no significant difference in the amount of viral RNA detected in pools of males versus females (Supplementary Figure S3, $p > 0.05$), indicating the assay was sensitive in pools of both sexes. There was only one discrepant result where 5/5 male pools versus 4/5 female pools were positive at the lowest titer of 10^0 pfu/mL. Combining sexes, at titers of 10^1 and above, successful detection of virus was 100% ($n = 10$). At 10^0, BUNV was detected in 90% of pools ($n = 10$, $p > 0.05$).

Ae. aegypti transmission capabilities for BUNV

We found our colony of *Ae. aegypti* were not competent for BUNV and thus not able to horizontally or vertically transmit the virus after a single bloodmeal ($n = 27$). A single mosquito that died at 1 day post exposure tested positive for a midgut infection, but was not included in the analysis as this was more than likely residual RNA from the infectious bloodmeal (midgut titer 1.3×10^3 pfu/mL). Mosquitoes receiving a second bloodmeal also showed no BUNV midgut infection ($n = 19$).

Rearing water contaminated with BUNV remained positive for RNA for the 5 days monitored. Initial quantification of RNA copies were approximately at $10^{4.5}$ genome equivalents/mL on days 0–1, while this dropped and remained consistent at $10^{2.5-3}$ for days 2–5. Attempts to quantify BUNV in rearing water via plaque assay were unsuccessful. Despite detection of BUNV RNA, no adult pool tested positive for BUNV. Similarly, a single pool of two pupa that had not emerged by day 6 were also negative for virus (Table 1, see Supplementary Methods). Additionally, larva that had not pupated by day 6 were also pooled and tested. Of the 19 pools, 5 (26%) tested positive for BUNV RNA with low titer (Table 1).

Extracellular stability of BUNV RNA under ecologically relevant conditions

Under simulated Rwandan conditions, in both whole blood and serum, BUNV RNA was detectable at moderate genome copies/mL up to 28 days in tubes (Figure 1A). The difference in average titer of genome copies between whole blood and sera was statistically significant at all time points ($p < 0.05$). Of interest, both in whole blood and sera, BUNV RNA remained moderately high out to day 28 (6.06×10^3 and 1.89×10^5, respectively). RNA was stable over all days collected for sera. In whole blood a significant decrease in RNA compared to baseline at day 0 was observed starting on day 21, but no further significant decrease was observed between days 21 and 28 (Figure 1A, $p < 0.05$). Unsurprisingly, liquid volume in plates evaporated quickly relative to tubes (Supplementary Figures S4–S5) and plate wells were dry between 6 and 8 days post inoculation. The last day of sampling is referred to as Day Dry—1 (Dry-1, see

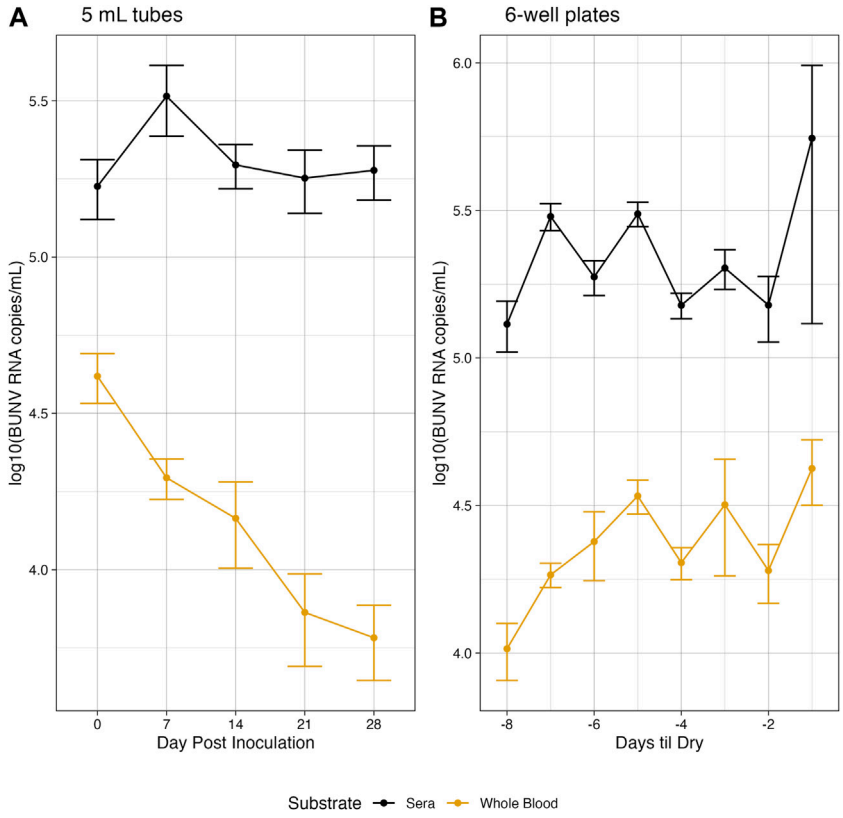

FIGURE 1
Environmentally stable BUNV. Genomic copies of BUNV recovered at each collection for both higher volume tubes **(A)** and lower volume plates **(B)** over time when exposed to Rwandan environmnetal temperatures.

Supplemental Methods). On average, 4.22×10^4 BUNV genome copies/mL was recovered on Dry-1 for whole blood, while the average recovered genome copies in sera was significantly more ($p < 0.05$) at 1.21×10^5 copies/mL on Dry-1 (Figure 1B). In sera the genome copies were stable as no significant differences were found between the RNA recovered on day 0 and Dry-1 ($p > 0.05$), while the RNA copies recovered in whole blood increased from day 0 to Dry −1 ($p < 0.05$). In a subset of plates ($n = 5$), media was added to dried out wells, collected, and subsequently tested for BUNV RNA (see Supplementary Methods). BUNV RNA was detected in the reconstituted samples, with an average of 6.87×10^4 RNA copies/mL in the reconstituted sera samples, and 6.74×10^4 RNA copies/mL in the reconstituted whole blood samples.

Infectivity of stable BUNV

For whole blood in tubes, the last day of infectiousness was day 28 for 80% (8/10) of samples and day 21 for the remining 20%. In tubes containing sera, the last day of infectiousness was day 21 for 50% (5/10) of replicates while the other 50% retained infectiousness out to day 28. Cytopathic effects (CPE) were observed in all infectious samples. Attempts to plaque sera and whole blood at these later time points were unsuccessful due to the consistency of the samples (see Supplementary Methods, Supplementary Figure S4). In 6-well plates, the range of days where infectiousness was retained was 5–7 days post inoculation but was dependent on the remaining volume in the well (Supplementary Figure S3; Supplementary Table S1). Relative to the first day of no volume, 50% (5/10) of the whole blood replicates retained infectiousness at Dry-1, and 100% at Dry-2. For sera however, all replicates retained infectiousness at Dry −1. We were able to plaque plate samples to further investigate the infectious titer of environmentally stable BUNV on the last day of infectiousness. Overall, whole blood had a significantly lower average infectious titer (1.04×10^3 PFU/mL) compared to sera (2.45×10^4 pfu/mL) (Figure 2, $p < 0.05$). No CPE was observed *in vitro* for any of the reconstituted dried samples, indicating a lack of infectivity despite moderate quantitative recovery of ~10^4 RNA copies/mL (see Supplementary Table S2).

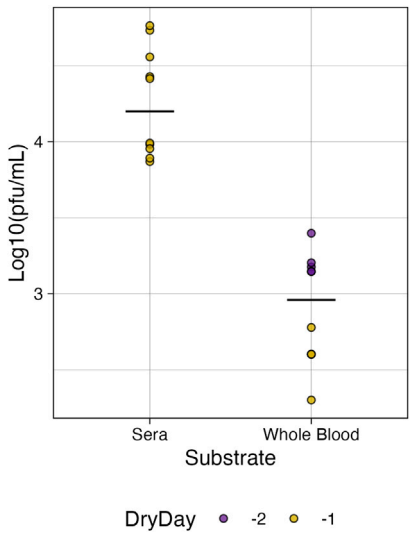

FIGURE 2
Infectious titer of BUNV in plates. The titer of infectious BUNV recovered from plates on the last day of observed infectiousness was significantly higher for sera than for whole blood ($p < 0.05$) relative to the day the plate was dry (Dry Day).

Discussion

BUNV was previously found to co-circulate with RVFV, and as such BUNV has been hypothesized to share aspects of the RVFV transmission cycle [1, 8]. However, the details surrounding the modalities of BUNV transmission remains understudied. RVFV has the potential to be transmitted both vertically and horizontally by *Ae. aegypti* [20, 40]. Further, other Orthobunyaviruses, such Lacrosse virus, Cache Valley virus (a strain of BUNV), and others have been shown to be transmitted by *Ae. aegypti* [35, 36, 42, 56]. We demonstrated that none of the exposed *Ae. aegypti* herein became infected with BUNV via oral exposure, which in turn meant there was no opportunity for ToT. We did show some potential uptake of virus from contaminated larval habitat, but no subsequent transstadial transmission was observed. Thus, there is some potential for refraction to BUNV in *Ae. aegypti* populations as our population did not support infection. As seen with RVFV [34], other *Ae. spp* may be involved in this alternative BUNV transmission modality. Likely there are overlapping ecological factors that contribute to the similarities in the observed transmission of BUNV and RVFV, such as an overall suitability for multiple mosquito species in the region, including seasonal rainfall and other weather patterns that affect mosquito population dynamics in general. However, our data do not rule out the possibility of urbanization of BUNV in other *Ae. aegypti* populations, as another population of this species was found to be moderately competent [39].

These data could also be of use during surveillance efforts during a BUNV disease outbreak. The sensitivity assay demonstrates a high level of sensitivity for this primer set, as 9/10 samples with approximately ~5 RNA copies per 10 mosquitoes in 1,000 uL and 100% of samples with ~50 copies tested positive for BUNV via qRT-PCR, with a calculated LOD of 6.6 copies. Previous RT-PCR assays have low-end detections of BUNV RNA at relatively similar levels (700 copies and 2–20 copies per mL) [57, 58]. Further, it was previously found that in *Ae. spp* infected with Cache Valley Virus, an Orthobunyavirus in the Bunyamwera serogroup, the average titer of infectious virus ranged from approximately 3–5 log$TCID_{50}$ [35]. This assay falls well within these limits and is competitive with other available assays, suggesting use as a surveillance tool is plausible.

In areas with RVF transmission, contact with blood and fluids from cattle is highly associated with seropositivity to RVFV [27, 59], indicating the importance of environmentally mediated transmission for the epidemiology of this virus. Our data does support the potential for environmentally mediated transmission of BUNV through blood and/or sera contamination, possibly from processing of meat or contaminated fomites/instruments. In higher volumes (up to 5 mL initial volume in tubes), infectiousness was retained for up to 28 days. At lower volumes over larger surface areas (plates), infectiousness was shorter owing to the shorter time to dried up substrate, but was still retained up to a week. The importance of identifying this potential novel transmission modality of BUNV lies in the potential for education and increased biosafety and infection control practices in at-risk communities, where PPE use is not high [60]. Recently, it was reported that fomite transmission might contribute to the movement of RVFV from rural areas to urban, as cattle may be moved to satiate the demand for meat in human dense areas [61]. This risk is shared by BUNV, as this data demonstrates this similarity in risk of environmentally mediated transmission between RVFV and BUNV. Further, the finding that dried samples were unlikely to harbor infectious virus speaks to the possibility for moisture control as a biosafety measure in areas where this risk exists.

Additionally, the stability of BUNV in whole blood at an environmentally relevant temperature may also inform surveillance efforts. Blood collected from suspected BUNV infected cattle that was unable to be immediately preserved via cooling may still be of use for qualitative surveillance purposes. This also suggests a potential use of blood that was collected indirectly or from meat processing facilities. Butchers and slaughterhouses as a point of surveillance may help inform on the epidemiology of an outbreak due to the concentration of animals to a central location [61]. Furthermore, environmental stability of BUNV in liquid may assist in less conventional surveillance methods for arboviruses, as the potential for wastewater surveillance of other arboviruses has been discussed [62].

While this experiment simulated field conditions in terms of temperature and humidity, additional factors may affect long-

term BUNV stability and infectivity that we did not address herein. Both abiotic and biological contaminates found in the environment may alter the stability and infectivity by affecting the length of stability and/or probability of infectiousness over time. Furthermore, the physical environment may also influence BUNV stability, such as the moisture content of soil or rain influencing substrate moisture content which may extend the duration of infectiousness. While this is a limitation of our study, it only further emphasizes a need for a One Health and systems approach when characterizing understudied pathogens.

Given the role of animal and environmental factors and the potential to infect humans, viewing understudied Orthobunyaviruses such as BUNV through a One Health scope is immensely important, as changes animal, human, or the environmental conditions in the area may alter the epidemiology of BUNV. Thus, the data herein is an important addition to the knowledge of this neglected tropical disease and highlights the need for considering atypical transmission routes when cataloging the eco-epidemiology of viruses. It is important that we continue to investigate the interplay between these factors to be prepared to respond to the dynamic pressures of viral transmission and disease outbreaks.

Author contributions

Both authors were equally involved in hypothesis generation, experimental design, and writing and review of the manuscript. Experimentation was performed by ET. Data analysis performed by ET and overseen by RC. All authors contributed to the article and approved the submitted version.

Data availability statement

The original contributions presented in the study are included in the article/Supplementary Material, further inquiries can be directed to the corresponding author.

Ethics statement

The manuscript presents research on animals that do not require ethical approval for their study.

Funding

This work was partially funded by the School of Veterinary Medicine and USDA 1433 Animal Health and Disease Research Program (FAIN/Award Number: NI21AHDRXXXXG064).

Acknowledgments

The authors would like to acknowledge Mr. Alex Stackhouse for his assistance in the course of the project and for Kameko the cat for her generous help as a paperweight.

Conflict of interest

The authors declare that the research was conducted in the absence of any commercial or financial relationships that could be construed as a potential conflict of interest.

Publisher's note

Please note that the review of this paper was conducted at the previous publisher, SAGE.

Supplementary material

The Supplementary Material for this article can be found online at: https://www.ebm-journal.org/articles/10.3389/ebm.2024.10114/full#supplementary-material

References

1. Dutuze MF, Ingabire A, Gafarasi I, Uwituze S, Nzayirambaho M, Christofferson RC. Identification of Bunyamwera and possible other orthobunyavirus infections and disease in cattle during a Rift Valley fever outbreak in Rwanda in 2018. *Am J Trop Med Hyg* (2020) **103**:183–9. doi:10.4269/ajtmh.19-0596

2. Gerdes GH. Rift valley fever. *Vet Clin North America: Food Anim Pract* (2002) **18**:549–55. doi:10.1016/s0749-0720(02)00029-4

3. Peyre M, Chevalier V, Abdo-Salem S, Velthuis A, Antoine-Moussiaux N, Thiry E, et al. A systematic scoping study of the socio-economic impact of Rift Valley fever: research gaps and needs. *Zoonoses and Public Health* (2015) **62**:309–25. doi:10.1111/zph.12153

4. Siam AL, Meegan JM, Gharbawi KF. Rift Valley fever ocular manifestations: observations during the 1977 epidemic in Egypt. *Br J Ophthalmol* (1980) **64**:366–74. doi:10.1136/bjo.64.5.366

5. Daubney R, Hudson JR, Garnham PC. Enzootic hepatitis or rift valley fever. An undescribed virus disease of sheep cattle and man from east africa. *J Pathol Bacteriol* (1931) **34**:545–79. doi:10.1002/path.1700340418

6. Samy AM, Peterson AT, Hall M. Phylogeography of Rift Valley fever virus in africa and the arabian peninsula. *PLOS Negl Trop Dis* (2017) **11**:e0005226. doi:10.1371/journal.pntd.0005226

7. Davies FG, Linthicum KJ, James AD. Rainfall and epizootic Rift Valley fever. *Bull World Health Organ* (1985) **63**:941–3.

8. Dutuze MF, Nzayirambaho M, Mores CN, Christofferson RC. A review of Bunyamwera, batai, and ngari viruses: understudied orthobunyaviruses with potential one health implications. *Front Vet Sci* (2018) **5**:69. doi:10.3389/fvets.2018.00069

9. Hartman A. Rift Valley Fever. *Clin Lab Med* (2017) **37**:285–301. doi:10.1016/j.cll.2017.01.004

10. Elliott RM. Orthobunyaviruses: recent genetic and structural insights. *Nat Rev Microbiol* (2014) **12**:673–85. doi:10.1038/nrmicro3332

11. Kuhn JH, Abe J, Adkins S, Alkhovsky SV, Avšič-Županc T, Ayllón MA, et al. Annual (2023) taxonomic update of RNA-directed RNA polymerase-encoding negative-sense RNA viruses (realm Riboviria: kingdom Orthornavirae: phylum Negarnaviricota). *J Gen Virol* (2023) **104**:001864. doi:10.1099/jgv.0.001864

12. Sasaya T, Palacios G, Briese T, Di Serio F, Groschup MH, Neriya Y, et al. ICTV virus taxonomy profile: phenuiviridae 2023. *J Gen Virol* (2023) **104**. doi:10.1099/jgv.0.001893

13. Hughes HR, Adkins S, Alkhovskiy S, Beer M, Blair C, Calisher CH, et al. ICTV virus taxonomy profile: peribunyaviridae. *J Gen Virol* (2020) **101**:1–2. doi:10.1099/jgv.0.001365

14. Nashed NW, Olson JG, El-Tigani A. Isolation of batai virus (Bunyaviridae: Bunyavirus) from the blood of suspected malaria patients in Sudan. *Am J Trop Med Hyg* (1993) **48**:676–81. doi:10.4269/ajtmh.1993.48.676

15. Waddell L, Pachal N, Mascarenhas M, Greig J, Harding S, Young I, et al. Cache Valley virus: a scoping review of the global evidence. *Zoonoses and Public Health* (2019) **66**:739–58. doi:10.1111/zph.12621

16. Hofmann M, Wiethölter A, Blaha I, Jöst H, Heinemann P, Lehmann M, et al. Surveillance of Batai virus in bovines from Germany. *Clin Vaccin Immunol* (2015) **22**:672–3. doi:10.1128/cvi.00082-15

17. Tauro LB, Rivarola ME, Lucca E, Mariño B, Mazzini R, Cardoso JF, et al. First isolation of Bunyamwera virus (Bunyaviridae family) from horses with neurological disease and an abortion in Argentina. *Vet J* (2015) **206**:111–4. doi:10.1016/j.tvjl.2015.06.013

18. Yanase T, Kato T, Yamakawa M, Takayoshi K, Nakamura K, Kokuba T, et al. Genetic characterization of Batai virus indicates a genomic reassortment between orthobunyaviruses in nature. *Arch Virol* (2006) **151**:2253–60. doi:10.1007/s00705-006-0808-x

19. Linthicum KJ, Davies FG, Kairo A, Bailey CL. Rift Valley fever virus (family Bunyaviridae, genus *Phlebovirus*). Isolations from Diptera collected during an inter-epizootic period in Kenya. *J Hyg* (1985) **95**:197–209. doi:10.1017/s0022172400062434

20. Adeniji JA. *Vector competence of NIGERIAN strain of* Aedes aegypti *linn. (DIPTERA: CULICIDAE) for Rift Valley fever virus*. Department of Virology, Faculty of Basic Medical Sciences. University of Ibadan (2002). Available from: https://library.adhl.africa/handle/123456789/12263 (Accessed November 20, 2023).

21. Mohamed R, Abdelgadir DM, Bashab H. Transovarian transmission of Rift Valley fever virus by two species of mosquitoes in Khartoum state (Sudan): aedes vexans (Meigen) and *culex quinquefasciatus* (Say). *Sudan J Public Health* (2013) **8**:164–70.

22. Turell MJ, Reeves WC, Hardy JL. Transovarial and trans-stadial transmission of California encephalitis virus in Aedes dorsalis and Aedes melanimon. *Am J Trop Med Hyg* (1982) **31**:1021–9. doi:10.4269/ajtmh.1982.31.1021

23. Vargas HCM, Farnesi LC, Martins AJ, Valle D, Rezende GL. Serosal cuticle formation and distinct degrees of desiccation resistance in embryos of the mosquito vectors *Aedes aegypti*, Anopheles aquasalis and *Culex quinquefasciatus*. *J Insect Physiol* (2014) **62**:54–60. doi:10.1016/j.jinsphys.2014.02.001

24. Wright D, Kortekaas J, Bowden TA, Warimwe GM. Rift Valley fever: biology and epidemiology. *J Gen Virol* (2019) **100**:1187–99. doi:10.1099/jgv.0.001296

25. Valdez LD, Sibona GJ, Diaz LA, Contigiani MS, Condat CA. Effects of rainfall on Culex mosquito population dynamics. *J Theor Biol* (2017) **421**:28–38. doi:10.1016/j.jtbi.2017.03.024

26. Ha TV, Kim W, Nguyen-Tien T, Lindahl J, Nguyen-Viet H, Thi NQ, et al. Spatial distribution of Culex mosquito abundance and associated risk factors in Hanoi, Vietnam. *PLOS Negl Trop Dis* (2021) **15**:e0009497. doi:10.1371/journal.pntd.0009497

27. Nyakarahuka L, de St Maurice A, Purpura L, Ervin E, Balinandi S, Tumusiime A, et al. Prevalence and risk factors of Rift Valley fever in humans and animals from Kabale district in Southwestern Uganda, 2016. *PLOS Negl Trop Dis* (2018) **12**:e0006412. doi:10.1371/journal.pntd.0006412

28. Gerken KN, Labeaud AD, Mandi H, L'Azou Jackson M, Breugelmans JG, King CH. Paving the way for human vaccination against Rift Valley fever virus: a systematic literature review of RVFV epidemiology from 1999 to 2021. *PLOS Negl Trop Dis* (2022) **16**:e0009852. doi:10.1371/journal.pntd.0009852

29. Nicholas DE, Jacobsen KH, Waters NM. Risk factors associated with human Rift Valley fever infection: systematic review and meta-analysis. *Trop Med Int Health* (2014) **19**:1420–9. doi:10.1111/tmi.12385

30. Craig DE, Thomas WJ, Desanctis AN. Stability of Rift Valley fever virus at 4 C. *Appl Microbiol* (1967) **15**:446–7. doi:10.1128/am.15.2.446-447.1967

31. Shimshony A, Barzilai R. Rift Valley Fever. *Adv Vet Sci Comp Med* (1983) **27**:347–425.

32. European Food Safety Authority EFSA. Opinion of the scientific panel on animal health and welfare (AHAW) on a request from the commission related to "the risk of a Rift Valley fever incursion and its persistence within the community". *EFSA J* (2005) **3**:238. doi:10.2903/j.efsa.2005.238

33. Francis T, Magill TP. Rift Valley Fever. *J Exp Med* (1935) **62**:433–48. doi:10.1084/jem.62.3.433

34. Turell MJ, Beaman JR, Linthicum KJ. Transmission of Rift Valley fever virus by adult mosquitoes after ingestion of virus as larvae. *Am J Trop Med Hyg* (1990) **43**:677–80. doi:10.4269/ajtmh.1990.43.677

35. Ayers VB, Huang Y-JS, Lyons AC, Park SL, Dunlop JI, Unlu I, et al. Infection and transmission of Cache Valley virus by *Aedes albopictus* and *Aedes aegypti* mosquitoes. *Parasites and Vectors* (2019) **12**:384. doi:10.1186/s13071-019-3643-0

36. Chan KK, Auguste AJ, Brewster CC, Paulson SL. Vector competence of Virginia mosquitoes for zika and Cache Valley viruses. *Parasites and Vectors* (2020) **13**:188. doi:10.1186/s13071-020-04042-0

37. EFSA Panel on Animal Health and Welfare AHAW. Scientific opinion on Rift Valley fever. *EFSA J* (2013) **11**:3180. doi:10.2903/j.efsa.2013.3180

38. Mweya CN, Kimera SI, Kija JB, Mboera LEG. Predicting distribution of *Aedes aegypti* and *Culex pipiens* complex, potential vectors of rift valley fever virus in relation to disease epidemics in East Africa. *Infect Ecol Epidemiol* (2013) **3**:21748. doi:10.3402/iee.v3i0.21748

39. Odhiambo C, Venter M, Chepkorir E, Mbaika S, Lutomiah J, Swanepoel R, et al. Vector competence of selected mosquito species in kenya for ngari and bunyamwera viruses. *J Med Entomol* (2014) **51**:1248–53. doi:10.1603/me14063

40. Kading RC, Crabtree MB, Bird BH, Nichol ST, Erickson BR, Horiuchi K, et al. Deletion of the NSm virulence gene of rift valley fever virus inhibits virus replication in and dissemination from the midgut of *Aedes aegypti* mosquitoes. *Plos Negl Trop Dis* (2014) **8**:e2670. doi:10.1371/journal.pntd.0002670

41. Seufi AM, Galal FH. Role of culex and anopheles mosquito species as potential vectors of rift valley fever virus in Sudan outbreak, 2007. *BMC Infect Dis* (2010) **10**:65. doi:10.1186/1471-2334-10-65

42. Hughes MT, Gonzalez JA, Reagan KL, Blair CD, Beaty BJ. Comparative potential of *Aedes triseriatus*, *Aedes albopictus*, and *Aedes aegypti* (Diptera: Culicidae) to transovarially transmit La crosse virus. *J Med Entomol* (2006) **43**:757–61. doi:10.1093/jmedent/43.4.757

43. Dutuze MF, Mayton EH, Macaluso JD, Christofferson RC. Comparative characterization of the reassortant Orthobunyavirus Ngari with putative parental viruses, Bunyamwera and Batai: *in vitro* characterization and *ex vivo* stability. *J Gen Virol* (2021) **102**:001523. doi:10.1099/jgv.0.001523

44. Habiyaremye G, Jairu N, De la Paix Mupenzi J, Ngamije J, Baragahoranye I, Karangwa A. Statistical analysis of climatic variables and prediction outlook in Rwanda. *East Afr J Sci Technol* (2012) **1**:27–34.

45. Mayton EH, Tramonte AR, Wearing HJ, Christofferson RC. Age-structured vectorial capacity reveals timing, not magnitude of within-mosquito dynamics is critical for arbovirus fitness assessment. *Parasites and Vectors* (2020) **13**:310. doi:10.1186/s13071-020-04181-4

46. Schmidt OW, Cooney MK, Kenny GE. Plaque assay and improved yield of human coronaviruses in a human rhabdomyosarcoma cell line. *J Clin Microbiol* (1979) **9**:722–8. doi:10.1128/jcm.9.6.722-728.1979

47. Ragan I, Hartson L, Pidcoke H, Bowen R, Goodrich R. Pathogen reduction of SARS-CoV-2 virus in plasma and whole blood using riboflavin and UV light. *PLOS ONE* (2020) **15**:e0233947. doi:10.1371/journal.pone.0233947

48. Mayton EH, Hernandez HM, Vitek CJ, Christofferson RC. A method for repeated, longitudinal sampling of individual *Aedes aegypti* for transmission potential of arboviruses. *Insects* (2021) **12**:292. doi:10.3390/insects12040292

49. Molina-Cruz A, Bennett K, Barillas-Mury C, Richardson J, Black W, Gupta L. Effect of mosquito midgut trypsin activity on dengue-2 virus infection and dissemination in *Aedes aegypti*. *Am J Trop Med Hyg* (2005) **72**:631–7. doi:10.4269/ajtmh.2005.72.631

50. Veronesi E, Paslaru A, Ettlin J, Ravasi D, Flacio E, Tanadini M, et al. Estimating the impact of consecutive blood meals on vector competence of *Aedes albopictus* for chikungunya virus. *Pathogens* (2023) **12**:849. doi:10.3390/pathogens12060849

51. Armstrong PM, Ehrlich HY, Magalhaes T, Miller MR, Conway PJ, Bransfield A, et al. Successive blood meals enhance virus dissemination within mosquitoes and increase transmission potential. *Nat Microbiol* (2019) **5**:239–47. doi:10.1038/s41564-019-0619-y

52. Merkes CMKK, Allison MJ, Goldberg C, Helbing CC, Hunter ME, Jackson CA, et al. *Generic qPCR limit of detection (LOD)/limit of quantification (LOQ) calculator* (2019). Available from: https://github.com/cmerkes/qPCR_LOD_Calc.2019 (Accessed November 20, 2023).

53. Ritz C, Baty F, Streibig JC, Gerhard D. Dose-response analysis using R. *PLOS ONE* (2015) **10**:e0146021. doi:10.1371/journal.pone.0146021

54. Xu S, Chen M, Feng T, Zhan L, Zhou L, Yu G. Use ggbreak to effectively utilize plotting space to deal with large datasets and outliers. *Front Genet* (2021) **12**:774846. doi:10.3389/fgene.2021.774846

55. Gu W, Lampman R, Novak RJ. Assessment of arbovirus vector infection rates using variable size pooling. *Med Vet Entomol* (2004) **18**:200–4. doi:10.1111/j.0269-283x.2004.00482.x

56. Bergren N, Kading R. The ecological significance and implications of transovarial transmission among the vector-borne bunyaviruses: a review. *Insects* (2018) **9**:173. doi:10.3390/insects9040173

57. Villinger J, Mbaya MK, Ouso D, Kipanga PN, Lutomiah J, Masiga DK. Arbovirus and insect-specific virus discovery in Kenya by novel six genera multiplex high-resolution melting analysis. *Mol Ecol Resour* (2017) **17**:466–80. doi:10.1111/1755-0998.12584

58. Lambert AJ, Lanciotti RS. Consensus amplification and novel multiplex sequencing method for S segment species identification of 47 viruses of the *orthobunyavirus*, *phlebovirus*, and nairovirus genera of the family bunyaviridae. *J Clin Microbiol* (2009) **47**:2398–404. doi:10.1128/jcm.00182-09

59. Nicholas DE, Jacobsen KH, Waters NM. Risk factors associated with human Rift Valley fever infection: systematic review and meta-analysis. *Trop Med Int Health* (2014) **19**:1420–9. doi:10.1111/tmi.12385

60. Smith LJ, Schurer JM, Ntakiyisumba E, Shyaka A, Amuguni JH. Rift Valley fever knowledge, mitigation strategies and communication preferences among male and female livestock farmers in Eastern Province, Rwanda. *PLOS Negl Trop Dis* (2021) **15**:e0009705. doi:10.1371/journal.pntd.0009705

61. Gerken KN, Ndenga BA, Owuor KO, Winter CA, Seetah K, LaBeaud AD. Leveraging livestock movements to urban slaughterhouses for wide-spread Rift Valley fever virus surveillance in Western Kenya. *One Health* (2022) **15**:100457. doi:10.1016/j.onehlt.2022.100457

62. Lee WL, Gu X, Armas F, Leifels M, Wu F, Chandra F, et al. Monitoring human arboviral diseases through wastewater surveillance: challenges, progress and future opportunities. *Water Res* (2022) **223**:118904. doi:10.1016/j.watres.2022.118904

Experimental Biology & Medicine Conference

Orlando, FL - October 13 -16, 2024

Please visit **exbiomedcon.org** or scan the QR code for more info.

Keynote Lecturers

Namandjè Bumpus, Ph.D.
Chief Scientist - US Food and Drug Administration

Advancing Emerging Technologies in Regulatory Science

Michael Friedlander, Ph.D.
Vice President - Health Sciences and Technology at Virginia Tech

All events will take place at the Embassy Suites by Hilton, Orlando Lake Buena Vista South

Cardiovascular

Delphine Gomez, Ph.D.
University of Pittsburgh

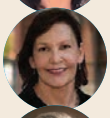

Karen Hirschi, Ph.D.
University of Virginia

Jay Humphrey, Ph.D.
Yale University

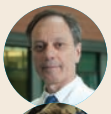

Ali J. Marian, M.D.
The University of Texas Health Science Center at Houston

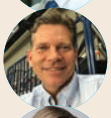

Joseph Miano, Ph.D.
Medical College of Georgia

Dianna Milewicz, M.D., Ph.D.
University of Texas Heath Science Center Houston

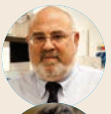

Robert Schwartz, Ph.D.
University of Houston

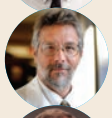

George Taffet, M.D.
Baylor College of Medicine

David Zawieja, Ph.D.
Texas A&M University Health Science Center

Neuroscience

Lique Coolen, Ph.D.
Kent State university

Michael Fehlings, M.D.
University of Toronto

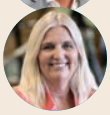

Susan Harkema, Ph.D.
University of Louisville

Maria Lehtinen, Ph.D.
Harvard University

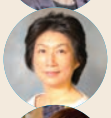

Fang Liu, Ph.D.
NCTR/US Food and Drug Administration

Agnes Luo, Ph.D.
University Cincinnati

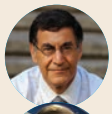

Mervyn Maze, MBChB
University of California San Francisco

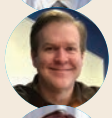

Dorian McGavern, Ph.D.
National Institute of Neurological Diorders and Stroke

Vesna Jevtovic-Todorovic, M.D., Ph.D.
University of Colorado School of Medicine

Regenerative Medicine

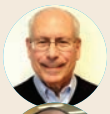

Arnold I. Caplan, Ph.D.
Case Western Reserve

Jian Feng, Ph.D.
State University of New York at Buffalo

Joshua Hare, M.D.
University of Miami

Karen Hasty, Ph.D.
University of Tennessee Health Science Center

Rajasingh Johnson, Ph.D.
University of Tennessee Health Science Center

Y. James Kang, DVM, Ph.D.
Sichuan University

Kwang-Soo Kim,Ph.D.
Harvard University

Joanne Kurtzberg, M.D.
Duke University

Jun Wu, Ph.D.
UT Southwestern

Trainees

Justin Boyd, Ph.D.
Vaxxinity

Udayan Apte, Ph.D.
U of Kansas Medical Center

Ram Kumar, Ph.D.
U of Kansas Medical Center

And More

Career Development
Short Talks
Poster Sessions
Member Blitz

SEBM SOCIETY FOR EXPERIMENTAL BIOLOGY AND MEDICINE

EBM Experimental Biology and Medicine

Scope

Experimental Biology and Medicine (EBM) is a global, peer-reviewed journal dedicated to the publication of multidisciplinary and interdisciplinary research in the biomedical sciences. The journal covers the spectrum of translational research from T0, basic research, to T4, population health. Articles in EBM represent cutting edge research at the overlapping junctions of the biological, physical and engineering sciences that impact upon the health and welfare of the world's population. EBM is particularly appropriate for publication of papers that are multidisciplinary in nature, are of potential interest to a wide audience, and represent experimental medicine in the broadest sense of the term. However, manuscripts reporting novel findings on any topic in the realm of experimental biology and medicine are most welcome.

EBM publishes Research, Reviews, Mini Reviews, and Brief Communications in the following categories.

- Anatomy/Pathology
- Artificial Intelligence/ Machine Learning Applications to Biomedical Research
- Biochemistry and Molecular Biology
- Bioimaging
- Biomedical Engineering
- Bionanoscience
- Cell and Developmental Biology
- Clinical Trials
- Endocrinology and Nutrition
- Environmental Health/Biomarkers/ Precision Medicine
- Genomics, Proteomics, and Bioinformatics
- Immunology/Microbiology/Virology
- Mechanisms of Aging
- Neuroscience
- Pharmacology and Toxicology
- Physiology and Pathophysiology
- Population Health
- Stem Cell Biology
- Structural Biology
- Synthetic Biology
- Systems Biology and Microphysiological Systems
- Translational Research

EBM Experimental Biology and Medicine

EBM is the official journal of the Society for Experimental Biology and Medicine

Led by Dr Steven Goodman, Experimental Biology and Medicine (EBM) is a global, peer-reviewed journal dedicated to the publication of multidisciplinary and interdisciplinary research in the biomedical sciences.

Discover more of our Special Issues

See more →

Contact

development@ebm-journal.org

See more

ebm-journal.org

publishingpartnerships.frontiersin.org/our-partners